

**UNIVERSIDADE FEDERAL DE SANTA CATARINA  
BIBLIOTECA UNIVERSITÁRIA**

Gustavo de Queiroz Hindi

**NUMERICAL ANALYSIS OF MIXTURE FORMATION IN FUEL  
SPRAYS USING ADVANCED TURBULENCE MODELING**

Florianópolis

2018



Gustavo de Queiroz Hindi

**NUMERICAL ANALYSIS OF MIXTURE FORMATION IN FUEL  
SPRAYS USING ADVANCED TURBULENCE MODELING**

Tese submetida ao Programa de Pós-Graduação  
em Engenharia Mecânica para posterior obtenção  
do Grau de Doutor em Engenharia Mecânica.

Orientador

Universidade Federal de Santa Catarina:

Prof. Dr. Emilio E. Paladino

Coorientador

Universidade Federal de Santa Catarina:

Prof. Dr. Amir A. M. de Oliveira Jr.

Florianópolis

2018

Ficha de identificação da obra elaborada pelo autor através do  
Programa de Geração Automática da Biblioteca Universitária da UFSC.

Hindi, Gustavo de Queiroz

Numerical analysis of mixture formation in fuel sprays using  
advanced turbulence modeling / Gustavo de Queiroz Hindi; orientador,  
Emilio E. Paladino, coorientador, Amir A. M. de Oliveira, 2018.  
165 p.

Tese (Doutorado) - Universidade Federal de Santa Catarina,  
Centro Tecnológico, Programa de Pós Graduação em Engenharia  
Mecânica, Florianópolis, 2018.

Inclui referências.

1. Engenharia Mecânica. 2. Spray de combustível,  
Formação de mistura. 3. CFD, LES, Interação turbulência  
partícula. I. Paladino, Emilio E. . II. Oliveira,  
Amir A. M. de. III. Universidade Federal de Santa  
Catarina. Programa de Pós-Graduação em Engenharia  
Mecânica. IV. Título.

Gustavo de Queiroz Hindi

**NUMERICAL ANALYSIS OF MIXTURE FORMATION IN FUEL  
SPRAYS USING ADVANCED TURBULENCE MODELING**

Esta Tese foi julgada aprovada para posterior obtenção do Título de “Doutor em Engenharia Mecânica”, e aprovada em sua forma final pelo Programa de Pós-Graduação em Engenharia Mecânica.

Florianópolis, 26 de Janeiro 2018.

---

Prof. Dr. Jonny Carlos da Silva  
Coordenador  
Universidade Federal de Santa Catarina

**Banca Examinadora:**

---

Prof. Dr. Emílio E. Paladino  
Universidade Federal de Santa Catarina

---

Prof. Dr. Aristeu Silveira Neto  
Relator  
Universidade Federal de Uberlândia

---

Prof. Dr. Guenther Carlos Krieger Filho  
Universidade de São Paulo

---

Profa. Dr. Cintia Soares  
Universidade Federal de Santa Catarina

---

Prof. Dr. Juan Pablo C. L. Salazar  
Universidade Federal de Santa Catarina

---

Prof. Dr. Antônio Fábio C. da Silva  
Universidade Federal de Santa Catarina

Este trabalho é dedicado à minha esposa Maria Luiza pela paciência e suporte ao longo de todos esses anos. Me ajudando a vencer os momentos difíceis e as incertezas.





## **AGRADECIMENTOS**

Agradeço aos professores Emílio e Amir. Ao Emílio pela disposição constante em ajudar, ao seu comprometimento com o meu desenvolvimento, pela confiança no meu trabalho e, pelo apoio e parceria nessa empreitada, onde por vários momentos, duvidei se obteria êxito. Ao Amir, pelo apoio e motivação durante as conversas que tivemos ao longo desse período. Quero ainda agradecer à Volvo do Brasil, pelo suporte durante os primeiros anos de estudo, por apoiar e incentivar o contínuo desenvolvimento do seu time de trabalho.



Ich wart seit Wochen auf diesen Tag und tanz  
vor Freude, über den Asphalt Als wär's ein  
Rhythmus, als gäb's ein Lied ...  
An Tagen wie diesen, wünscht man sich Un-  
endlichkeit An Tagen wie diesen, haben wir  
noch ewig Zeit ...  
Erleben wir das Beste, kein Ende ist in Sicht  
(Die Toten Hosen, 2012)



## RESUMO

As regulamentações de emissões em motores de combustão interna têm ficado cada vez mais rigorosas devido a preocupações ambientais e os impactos das emissões de gases poluentes na saúde. Para alcançar esses requisitos mais restritivos, simulação dos processos de combustão de motor tem sido extensivamente usadas a fim de projetar motores de combustão interna de forma mais rápida e com menor custo, permitindo uma melhor compreensão dos processos de injeção, evaporação e combustão assim como a otimização do motor visando maior eficiência e menor emissão de poluentes. Entretanto, a modelagem de combustão de spray é uma tarefa bastante desafiadora e um tópico ainda aberto na literatura, requerendo melhorias em diversos aspectos de suas aplicações. A revisão da literatura recente sobre modelagem de sprays de combustível sugere que a utilização da abordagem Large Eddy Simulation (LES) é de fundamental importância para representar de forma adequada as complexas interações entre spray e turbulência, que afetam todos os processos físicos de formação de mistura e combustão. Todavia, algumas deficiências foram identificadas quanto a precisão das simulações de sprays não-reativos, principalmente relacionados ao ajuste adequado de diferentes modelos e parâmetros numéricos e, em especial, no tamanho da malha, para capturar de forma adequada as interações entre o spray e a turbulência. Este trabalho apresenta a aplicação de modelos avançados de turbulência para o processo de spray em câmara estática, baseados na implementação do modelo de turbulência LES em um solver Lagrangeano para spray em OpenFOAM (código aberto). Os resultados obtidos para sprays não-reativos provam que resultados altamente precisos podem ser obtidos para comprimentos de penetração de líquido e vapor através da modelagem correta dos fenômenos envolvidos no spray e do adequado refinamento de malha para capturar corretamente as interações entre spray e turbulência. Esse trabalho contribui ainda com a proposta de um novo critério baseado no número de Stokes da gota, para o refinamento adaptativo de malha. Esse critério ainda permite avaliar até que extensão a dispersão turbulenta das gotas é adequadamente capturada para uma dada malha, usando a abordagem LES. Complementam o trabalho um estudo comparativo com modelos de turbulência baseados nas equações médias de Navier Stokes (RANS), análises de sensibilidade de condições ambientais na câmara estática e a influência das propriedades físicas do com-

bustível em características importantes do spray não reativo.

**Palavras-chave:** Spray de combustível, Formação de mistura, CFD, LES, Interação turbulência-partícula

## RESUMO EXPANDIDO

### Introdução

As regulamentações de emissões em motores de combustão interna têm ficado cada vez mais rigorosas devido a preocupações ambientais e os impactos das emissões de gases poluentes na saúde. Para alcançar esses requisitos mais restritivos, simulação dos processos de combustão de motor tem sido extensivamente usadas a fim de projetar motores de combustão interna de forma mais rápida e com menor custo, permitindo uma melhor compreensão dos processos de injeção, evaporação e combustão assim como a otimização do motor visando maior eficiência e menor emissão de poluentes. Entretanto, a modelagem de combustão de spray é uma tarefa bastante desafiadora e um tópico ainda aberto na literatura, requerendo melhorias em diversos aspectos de suas aplicações. A revisão da literatura recente sobre modelagem de sprays de combustível sugere que a utilização da abordagem Large Eddy Simulation (LES) é de fundamental importância para representar de forma adequada as complexas interações entre spray e turbulência, que afetam todos os processos físicos de formação de mistura e combustão. Todavia, algumas deficiências foram identificadas quanto a precisão das simulações de sprays não-reativos, principalmente relacionados ao ajuste adequado de diferentes modelos e parâmetros numéricos e, em especial, no tamanho da malha, para capturar de forma adequada as interações entre o spray e a turbulência. Este trabalho apresenta a aplicação de modelos avançados de turbulência para o processo de spray em câmara estática, baseados na implementação do modelo de turbulência LES em um solver Lagrangeano para spray em OpenFOAM (código aberto). Os resultados obtidos para sprays não-reativos provam que resultados altamente precisos podem ser obtidos para comprimentos de penetração de líquido e vapor através da modelagem correta dos fenômenos envolvidos no spray e do adequado refinamento de malha para capturar corretamente as interações entre spray e turbulência. Esse trabalho contribui ainda com a proposta de um novo critério baseado no número de Stokes da gota, para o refinamento adaptativo de malha. Esse critério ainda permite avaliar até que extensão a dispersão turbulenta das gotas é adequadamente capturada para uma dada malha, usando a abordagem LES. Complementam o trabalho um estudo comparativo com modelos de turbulência baseados nas equações médias de Navier Stokes (RANS), análises de sensibilidade de condições ambi-

entes na câmara estática e a influência das propriedades físicas do combustível em características importantes do spray não reativo.

## **Objetivos**

Na revisão da literatura atual sobre modelagem de sprays de combustível, algumas deficiências foram identificadas na precisão de simulações de sprays não reativos, que foram identificadas comapando os resultados de simulações e experimentos. Essas deficiências podem também comprometer a precisão das simulações de combustão. Por exemplo, uma penetração de líquido incorratamente alta pode levar a um excessivo incidência do spray nas paredes do cilindro e no topo do pistão e, como consequência na formação de mistura e emissões de material particulado. Também, uma penetração de vapor incorreta afeta a preparação de mistura, alterando o atraso de ignição e a taxa de liberação de calor. A taxa de liberação de calor, resultando das reações de combustão, irão afetar as temperaturas no cilindro que podem afetar as emissões de NO<sub>x</sub>, assim como as pressões em cilindro, diretamente impactando o trabalho produzido no ciclo. O principal objetivo desse trabalho é a modelagem do process de sprays não reativos incorporando modelos avançados de turbulência, que possam fornecer resultados precisos para as penetrações de líquido e vapor, assim como outras características importantes do spray provando dessa forma, que com uma modelagem adequada, modelos algébricos para interação entre spray e turbulência não sejam mais necessários.

## **Metodologia**

A metodologia inclui as seguintes etapas: (i) implementação de um modelo de turbulência LES acoplado a uma abordagem Lagrangeana de rastreamento das gotas de combustível na plataforma aberta OpenFOAM; (ii) melhora na abordagem LES atual para modelagem de sprays levando a predições mais precisas para sprays não-reativos, detalhando o impacto da dispersão turbulenta estocásticas das dotas, o efeito do número de partículas Lagrangeanas e o tamanho da malha Euleriana na representação estatística da dispersão turbulenta e o impacto da distorção dinâmica da gotas na força de arrasto sobre as elas; (iii) implementação de um novo critério de refino de malha, baseado no número de Stokes da gota para ser utilizado no refinamento adaptativo de malha; (iv) simulação de condições existentes na câmara de volume constante não-reativa, que estão disponíveis no Laboratório de Combustão da SANDIA (EUA), e estão publicadas como um banco de dados para avaliação da precisão das simulações dos modelos de spray; (v) realização de análises de sensibilidade relacionadas a pressões e temperaturas ambientes na camâra, tipo de combustível, com



o objetivo de descrever seus impactos nas características importantes de sprays não reativos, também comparando os resultados com correlações empíricas conhecidas para penetração de spray, ângulo de spray de diâmetro médio de Sauter (SMD).

## **Resultados e Discussão**

Nesse trabalho um solver Lagrangeano foi implementado em OpenFOAM2.0.x para analisar injeção de spray não-reativo. A estrutura turbulenta foi modelada usando a abordagem LES. O modelo utiliza refinamento de malha adaptativo, baseado na física do escoamento, para melhorar os resultados sem excessivo consumo de CPU. Um novo critério de malha baseado no número de Stokes da gota foi proposto e implementado. O solver foi validado contra resultados experimentais de spray, fornecidos pelo Laboratório de Combustão da SANDIA (EUA), simulando condições da câmara de volume constante não-reativa. Nesse trabalho é mostrado que, com a modelagem LES de sprays usando sub-modelos adequados e o correto nível de refinamento de malha, indendência de pode ser alcançada sem necessidade de ajustes adicionais nos parâmetros de quebra ou nos critérios de penetração, como verificado em alguns trabalhos apresentados na literatura. Além disso, os resultados melhoram com o refinamento da malha, sem necessidade de definir um tamanho específico de malha para obtenção de resultados otimizados, como apresentado no conceito de “convergência de malha” na literatura. Esse fato é de importância fundamental, pois atende o conceito básico de consistência dos métodos numéricos. Também é mostrado que modelos STD são necessários para melhorar as predições de penetração mas, no contexto LES, aonde STD leva em conta a dispersão de sub-malha, um refinamento adequado de malha é necessário para atingir predições corretas, mesmo com a inclusão desses modelos. Adicionalmente, uma análise é apresentada, considerando o número de Stokes de sub-malha, mostrando que existe um tamanho de malha que deve incluir os efeitos de dispersão turbulenta nas gotas, considerando somente as escalas resolvidas, e nenhum modelo STD seria então necessário. Esse critério apresentado no trabalho, baseado no número de Stokes de sub-malha, foi de forma bem sucedida utilizado como critério para refinamento adaptativo de malha. Em condições com taxas de evaporação reduzidas aonde a fase líquida poderia penetrar a frente da fase vapor, a utilização de somente a fração de combustível vaporizado como critério de refinamento poderá falhar na caracterização adequada da penetração de líquido. Nesse cenário o número de Stokes baseado na fase líquida poderá ser um parâmetro mais adequado para re-

finamento adaptativo de malha. Em condições aonde a taxa de evaporação é alta, o critério de fração de combustível vaporizado pode caracterizar a penetração de líquido com boa precisão, enquanto captura melhor a difusão da fase vapor na direção perpendicular ao eixo do jato do spray de combustível. Dessa forma para melhorar a precisão e caracterizar adequadamente os comprimentos de penetração de líquido e vapor, sem conhecer a priori a taxa de evaporação, é recomendado a utilização de ambos os número de Stokes e fração de combustível vaporizado como critérios para refinamento de malha. Relativo a quantidade de parcels para assegurar uma boa representação estatística da fase Lagrangeana, nos cenários simulados nessa tese, assumindo uma relação mínima de  $130k$  a  $150k$  *parcels/mg* de massa de combustível injetado, mostrou que esse parâmetro não tem muita influência nos resultados.

### **Considerações Finais**

Os resultados obtidos nesse trabalho para sprays não-reativos provam que predições altamente precisas podem ser obtidos para penetrações de líquido e vapor através da correta modelagem dos fenômenos do spray e do adequado refinamento da malha para capturar de forma correta as interações entre spray e turbulência. Esse trabalho também contribui com a proposta de um novo critério baseado no número de Stokes da gota, para refinamento adaptativo de malha. Esse critério também avalia até que extensão a dispersão turbulenta das gotas é capturada de forma adequada para um dado tamanho de malha, usando a abordagem LES. A comparação com modelo de turbulência baseado nas equações médias de Navier-Stokes (RANS), análise de sensibilidade para condições ambientes da câmara estática e, a influência das propriedades físicas do combustível em características importantes dos sprays não-reativos também foram exploradas.

**Palavras-chave:** Spray de combustível, Formação de mistura, CFD, LES, Interação turbulência-partícula

## ABSTRACT

Emissions' standards for internal combustion engines are becoming ever more stringent due to environmental concerns and the impact on health from pollutant's emissions. To meet these stringent targets, computational fluid dynamics simulation of engine in-cylinder processes has been extensively used for engine design in a faster and more cost effective way, allowing better understanding of the injection, evaporation and combustion processes to optimize the engine for lower emissions and higher efficiencies. However, spray combustion modeling is a very challenging task and a topic still open in literature with areas that require improvements. The review of current literature on fuel spray modeling approaches suggests that the usage of Large Eddy Simulation (LES) is of critical importance in order to represent the complex interactions between spray and turbulence, that affects all the physical processes related to mixture formation and combustion. However, some deficiencies have been identified related to the accuracy of non-reacting spray simulations, mainly related to the adequate setup of different models and numerical parameters and, in special, the mesh size, to adequately capture the interactions between spray and turbulence. This work presents the application of advanced turbulence modeling to the spray injection process in a static chamber, based on the implementation of a LES turbulence model in a Lagrangian spray based solver in OpenFOAM (open source code). Results that have been obtained hitherto for non-reacting sprays have proven that highly accurate results can be obtained for liquid and vapor length penetrations by correct modeling of spray phenomena and adequate mesh refinement to correctly capture turbulence-spray interactions. This work also contributes with a proposal for a new criterion based on the droplet Stokes number, for adaptive mesh refinement. This criterion also allows to assess to what extent the droplets' turbulent dispersion is properly captured for a given mesh size, using LES approach. Complement this work a turbulence model comparison based on the averaged Navier Stokes equations (RANS), sensitivity analyses of ambient conditions in the static chamber and, the influence of the fuel's physical properties in important characteristics of non-reacting sprays.

**Keywords:** Fuel spray, Mixture formation, CFD, LES, Turbulence-Particle interaction



## LIST OF FIGURES

|           |  |    |
|-----------|--|----|
| Figure 1  | Schematic of a full cone injector spray. Source: Baumgarten (2006).  | 39 |
| Figure 2  | Multi-hole fuel injector spray. Source: Smith et al. (2011)  | 40 |
| Figure 3  | Kelvin Helmholtz model. Source: Baumgarten (2006).   | 51 |
| Figure 4  | Rayleigh-Taylor instability on a liquid drop. Source: Baumgarten (2006).   | 53 |
| Figure 5  | Combined KH-RT breakup model solution flow diagram.  | 54 |
| Figure 6  | Combined KH-RT breakup models. Source: Baumgarten (2006).  | 55 |
| Figure 7  | Taylor-Analogy Breakup. Source: Baumgarten (2006).   | 56 |
| Figure 8  | Gas-droplet velocity calculation: (a) nearest vertex, (b) interpolation. Source: (BAUMGARTEN, 2006).   | 63 |
| Figure 9  | Liquid-gas phase momentum exchange.  | 64 |
| Figure 10 | Influence of liquid penetration definition on results comparison with experiment from ECN.   | 65 |
| Figure 11 | Liquid and vapor penetration plots from Senecal et al. (2013).   | 66 |
| Figure 12 | Liquid and vapor penetration plots from Xue et al. (2013).   | 66 |
| Figure 13 | Liquid and vapor penetration plots from Wehrfritz et al. (2013).   | 67 |
| Figure 14 | Liquid and vapor penetration plots from Banerjee and Rutland (2015).   | 68 |
| Figure 15 | Liquid and vapor penetration plots from Jangi et al. (2015).   | 69 |
| Figure 16 | Possible droplet trajectories in a turbulent flow field. Source: (CROWE; CHUNG; TROUTT, 1988).   | 72 |
| Figure 17 | Graphical representation of hexahedral cell splitting in cell-PointFace method.  | 75 |
| Figure 18 | Interpolation schemes impact on liquid and vapor length penetration  | 76 |
| Figure 19 | Photo of the optically accessible high-temperature, high-pressure spray chamber at Sandia (left), schematic of Sandia combustion vessel (right). Source: Sandia National Laboratories. | 79 |
| Figure 20 | Comparison between mass flow rate signals. Source: ECN.  | 81 |
| Figure 21 | Non-reacting cases mass flow rate.   | 81 |
| Figure 22 | Liquid length penetration measurement uncertainty.   | 82 |
| Figure 23 | Vapor length penetration measurement uncertainty.  | 82 |

|  |     |
|--|-----|
| Figure 24 CFD vessel (left), initial mesh with 1mm cells (center), adaptive mesh refined with 4 levels of AMR (right). . . . .   | 83  |
| Figure 25 AMR2 parcel count impact on liquid and vapor penetration. .  | 85  |
| Figure 26 AMR4 parcel count impact on liquid and vapor penetration. .  | 86  |
| Figure 27 Mean relative gas velocity in a cross-section plane through the injector centerline and spray parcels - AMR2 (left), AMR4 (right) at 0.05 ms. . . . .                            | 87  |
| Figure 28 Subgrid turbulent kinetic energy with AMR4 (left) and AMR5 (right) at 0.15 ms without STD. . . . .   | 88  |
| Figure 29 $\lambda_2$ iso-surfaces for AMR2B (left), AMR4B (center), AMR5B (right) without STD at 0.05ms, 0.15ms (1 <sup>st</sup> and 2 <sup>nd</sup> rows respectively)...                | 89  |
| Figure 30 $nC_{12}H_{26}$ vapor distribution - AMR2A (left), AMR4A (center) and AMR5A (right), all without STD at 0.10ms. . . . .  | 90  |
| Figure 31 Vapor penetraion criterion - 0.1% of mass fraction distribution - AMR2A (left), AMR4A (center) and AMR5A (right), all without STD at 0.10ms. . . . .                             | 91  |
| Figure 32 Mesh size impact on liquid and vapor penetration (a) with STD model and (b) without STD model. . . . .   | 93  |
| Figure 33 $nC_{12}H_{26}$ vapor distribution. . . . .  | 95  |
| Figure 34 AMR2 and 4 - 1000k parcels - Dynamic droplet distortion impact on liquid and vapor penetration. . . . .  | 96  |
| Figure 35 Droplet Stokes number with AMR2 (left), AMR4 (center) and AMR5 (right) without STD at 0.10ms. . . . .  | 97  |
| Figure 36 Droplet Stokes number plot along the injector centerline, closer to the injector tip (1 <sup>st</sup> row) and further away (2 <sup>nd</sup> row) without STD at 0.10ms. . . . . | 98  |
| Figure 37 Droplet Stokes number plot along an horizontal line 4 mm below the injector tip without STD at 0.10ms. . . . .   | 99  |
| Figure 38 Liquid and vapor penetration for different refinement levels, using Stokes criterion, without STD modeling. . . . .  | 100 |
| Figure 39 Comparison to ECN Test 2 with AMR5 using the $St_{sgs} \geq 1$ criterion. . . . .  | 101 |
| Figure 40 Fraction of turbulent energy resolved for AMR2 (left), AMR4 (center) and AMR5 (right) meshes, at 0.05ms after start of injection. . . .  | 102 |
| Figure 41 Fraction of the turbulent flow energy resolved plot along the centerline of the injector, at 0.05ms after start of injection. . . . .  | 103 |
| Figure 42 Fraction of the turbulent flow energy plot along an horizontal   |     |

|  |     |
|--|-----|
| line 4mm below the injector tip, at 0.05ms after start of injection. . . . .   | 103 |
| Figure 43 Fraction of the turbulent flow energy plot along an horizontal line 9mm below the injector tip, at 0.05ms after start of injection. . . . .  | 104 |
| Figure 44 Refined mesh from LES simulated cases used as fixed meshes for the RANS simulated cases - 4 levels of refinement (left) and 5 levels of refinement (right). . . . .                                | 105 |
| Figure 45 Gas velocity magnitude RANS (left) and LES (right) with 4 and 5 levels of cell refinement (1 <sup>st</sup> and 2 <sup>nd</sup> rows respectively), at 0.05ms after start of injection. . . . .     | 106 |
| Figure 46 Comparison between RANS and LES on z-component of gas velocity at 0.05ms after start of injection with the mesh from the AMR4 LES case. . . . .  | 107 |
| Figure 47 Comparison between RANS and LES on z-component of gas velocity at 0.05ms after start of injection with the mesh from the AMR5 LES case. . . . .  | 108 |
| Figure 48 Volume average of parcel velocity evaluated at different positions below the injector tip. . . . .   | 109 |
| Figure 49 Droplet velocity magnitude RANS (left) and LES (right) with 4 and 5 levels of cell refinement (1 <sup>st</sup> and 2 <sup>nd</sup> rows respectively), at 0.05ms after start of injection. . . . . | 110 |
| Figure 50 Droplet drag RANS (left) and LES (right) with 4 and 5 levels of cell refinement (1 <sup>st</sup> and 2 <sup>nd</sup> rows respectively), at 0.05ms after start of injection. . . . .               | 111 |
| Figure 51 Comparison among LES and RANS on liquid and vapor length penetrations with the mesh from AMR4 LES case. . . . .  | 112 |
| Figure 52 Comparison among LES and RANS on liquid and vapor length penetrations with the mesh from AMR5 LES case. . . . .  | 112 |
| Figure 53 $nC_{12}H_{26}$ vapor distribution with 4 levels of cell refinement mesh RANS (left) and LES (right), at 0.05ms and 0.10ms (1 <sup>st</sup> and 2 <sup>nd</sup> rows respectively). . . . .        | 114 |
| Figure 54 $nC_{12}H_{26}$ vapor distribution with 5 levels of cell refinement mesh RANS (left) and LES (right), at 0.05ms and 0.10ms (1 <sup>st</sup> and 2 <sup>nd</sup> rows respectively). . . . .        | 115 |
| Figure 55 Schlieren image extracted from the Sandia experiment showing vapor region border at 0.10ms. . . . .  | 116 |
| Figure 56 Comparison between RANS turbulent kinetic energy (left) and LES total kinetic energy (right), at 0.10ms after start of injection. . . . .  | 116 |
| Figure 57 Turbulent kinetic energy plot along the centerline of the injector, at 0.10ms after start of injection. . . . .  | 117 |

|  |     |
|--|-----|
| Figure 58 Turbulent kinetic energy plot along an horizontal line 4mm below the injector tip, at 0.10ms after start of injection. ....  | 117 |
| Figure 59 Turbulent kinetic energy plot along an horizontal line 9mm below the injector tip, at 0.10ms after start of injection. ....  | 118 |
| Figure 60 Turbulent viscosity RANS (left) and LES (right) meshes with 5 levels of cell refinement, at 0.10ms after start of injection. ....  | 119 |
| Figure 61 Comparison among RANS and LES both with AMR enabled with 3 levels of refinement on liquid and vapor length penetrations. ....  | 120 |
| Figure 62 Mesh at 0.05ms for RANS case (left) and LES (right). ....  | 121 |
| Figure 63 $nC_{12}H_{26}$ vapor distribution with AMR and 3 levels of cell refinement RANS (left) and LES (right), at 0.05ms after start of injection. .   | 121 |
| Figure 64 Refinement criterion impact on liquid length penetration. ....   | 124 |
| Figure 65 Resulting mesh with vaporized fuel fraction criterion (left) and $St_{sgs}$ criterion (right), at 0.10ms. ....   | 124 |
| Figure 66 $nC_{12}H_{26}$ vapor distribution and parcels - vaporized fuel fraction criterion (left) and $St_{sgs}$ criterion (right), at 0.05ms and 0.10ms (1 <sup>st</sup> and 2 <sup>nd</sup> rows respectively). ....                                 | 125 |
| Figure 67 Refinement criterion impact on liquid length penetration with vessel temperature of 900K. ....   | 126 |
| Figure 68 Resulting mesh with vaporized fuel fraction criterion (left) and $St_{sgs}$ criterion (right), at 0.10ms with vessel temperature of 900K. ....   | 127 |
| Figure 69 $nC_{12}H_{26}$ vapor distribution and parcels - vaporized fuel fraction criterion (left) and $St_{sgs}$ criterion (right), at 0.05ms and 0.10ms (1 <sup>st</sup> and 2 <sup>nd</sup> rows respectively) with vessel temperature of 900K. .... | 128 |
| Figure 70 Spray tip penetration predicted from Eq. 5.1 for the case with vessel ambient pressure of 4MPa, compared to 3D simulation. ....  | 130 |
| Figure 71 Vessel pressure impact on liquid and vapor length penetrations. ....   | 131 |
| Figure 72 Volume average of parcel velocity evaluated at different positions below the injector tip. ....  | 132 |
| Figure 73 Droplet velocity magnitude as a consequence of the varying vessel ambient pressure - 4MPa (left), 6MPa (center) and 8MPa (right), at 0.05ms after start of injection. ....   | 133 |
| Figure 74 Vapor mass phase diffusivity for n-Dodecane as a function of temperature. ....   | 134 |
| Figure 75 Vessel pressure impact on liquid and vapor length penetrations. ....   | 135 |
| Figure 76 $nC_{12}H_{26}$ vapor distribution and parcels - P=4MPa (left), 6MPa (center) and 8MPa (right), at 0.05ms, 0.10ms and 0.15ms (1 <sup>st</sup> , 2 <sup>nd</sup> and  |     |



|  |     |
|--|-----|
| 3 <sup>rd</sup> rows respectively). . . . .  | 136 |
| Figure 77 Spray tip penetration predicted from Eq. 5.1 with varying vessel and injection conditions. . . . .   | 139 |
| Figure 78 Vessel temperature impact on liquid and vapor length penetrations. . . . .   | 140 |
| Figure 79 Vessel pressure impact on liquid and vapor length penetrations. . . . .  | 141 |
| Figure 80 $nC_{12}H_{26}$ vapor distribution and parcels - T=600K (left), 900K (center) and 1200K (right), at 0.05ms, 0.10ms and 0.15ms (1 <sup>st</sup> , 2 <sup>nd</sup> and 3 <sup>rd</sup> rows respectively). . . . . | 142 |
| Figure 81 Liquid and vapor length penetrations comparing cases with similar gas density. . . . .   | 143 |
| Figure 82 Vapor pressure comparison between $nC_7H_{16}$ and $nC_{12}H_{26}$ . . . . .   | 146 |
| Figure 83 Surface tension comparison between $nC_7H_{16}$ and $nC_{12}H_{26}$ . . . . .  | 147 |
| Figure 84 Dynamic viscosity comparison between $nC_7H_{16}$ and $nC_{12}H_{26}$ . . . . .  | 147 |
| Figure 85 Ohnesorge number ratio comparison between $nC_{12}H_{26}$ to $nC_7H_{16}$ . . . . .  | 148 |
| Figure 86 Gas Weber number ratio comparison between $nC_7H_{16}$ to $nC_{12}H_{26}$ . . . . .  | 149 |
| Figure 87 Volume average of parcel Velocity evaluated at different positions below the injector tip. . . . .   | 150 |
| Figure 88 Droplet velocity magnitude $nC_{12}H_{26}$ (left) and $nC_7H_{16}$ (right), at 0.05ms after start of injection. . . . .  | 151 |
| Figure 89 Droplet drag $nC_{12}H_{26}$ (left) and $nC_7H_{16}$ (right) fuel sprays, at 0.05ms after start of injection. . . . .  | 152 |
| Figure 90 Comparison between $nC_{12}H_{26}$ and $nC_7H_{16}$ on liquid and vapor length penetrations. . . . .   | 153 |
| Figure 91 $nC_{12}H_{26}$ vapor distribution (left) and $nC_7H_{16}$ (right), at 0.05ms and 0.15ms (1 <sup>st</sup> and 2 <sup>nd</sup> rows respectively). . . . .  | 154 |



## LIST OF TABLES

|         |  |     |
|---------|--|-----|
| Table 1 | KH-RT model constants . . . . .                                | 70  |
| Table 2 | Non Reacting Case Details . . . . .                            | 80  |
| Table 3 | Cases' Definition . . . . .                                    | 84  |
| Table 4 | Sauter Mean Diameter Evaluated at $0.05ms$ After SOI . . . . . | 131 |
| Table 5 | Vessel and Spray Conditions - Pressure Analyses . . . . .      | 137 |
| Table 6 | Vessel and Spray Conditions - Temperature Analyses . . . . .   | 144 |
| Table 7 | Sauter Mean Diameter Evaluated at $0.05ms$ After SOI . . . . . | 144 |
| Table 8 | Vessel and Spray Conditions - Fuel Type Analyses . . . . .     | 145 |
| Table 9 | SMD Evaluated at $0.05ms$ After SOI for Both Fuels . . . . .   | 150 |



## LIST OF ABBREVIATIONS AND ACRONYMS

|                 |  |
|-----------------|--|
| AMR             | Adaptive Mesh Refinement                           |
| API             | American Petroleum Institute                       |
| CFD             | Computational Fluid Dynamics                       |
| CO              | Carbon Monoxide                                    |
| CPF             | cellPointFace interpolation scheme                 |
| DI              | Direct Injection                                   |
| DIC             | Diagonal Incomplete-Cholesky                       |
| DILU            | Diagonal Incomplete LU                             |
| DNS             | Direct Numerical Simulation                        |
| ECN             | Engine Combustion Network                          |
| GHG             | Greenhouse Gas                                     |
| HC              | Hydrocarbon  |
| KH              | Kelvin-Helmholtz                                   |
| LES             | Large Eddy Simulation                              |
| NIST            | National Institute of Standards and Technology     |
| NO <sub>x</sub> | Nitric Oxides                                      |
| PBiCG           | Preconditioned Bi-Conjugated Gradient              |
| PCG             | Preconditioned Conjugated Gradient                 |
| PIMPLE          | Combination of PISO and SIMPLE algorithms          |
| PISO            | Pressure Implicit with Splitting of Operators      |
| PM              | Particulate Matter                                 |
| PMVC            | Point Mean Value Coordinates interpolation scheme  |
| RANS            | Reynolds Averaged Navier Stokes                    |
| RNG             | Re-Normalisation Group                             |
| RT              | Rayleigh-Taylor                                    |
| SIMPLE          | Semi Implicit Method for Pressure Linked Equations |
| SIT             | Spray Induced Turbulence                           |
| SMD             | Sauter Mean Diameter                               |
| SOI             | Start of Injection                                 |
| STD             | Stochastic Turbulent Dispersion                    |
| TAB             | Taylor-Analogy Breakup                             |
| TKE             | Turbulent Kinetic Energy                           |



## LIST OF SYMBOLS

### Roman Letters

|         |   |
|---------|---|
| $a$     | droplet acceleration  |
| $A$     | droplet area; area  |
| $B$     | Spalding transfer number  |
| $c_p$   | specific heat at constant pressure                                  |
| $C_\mu$ | $k - \varepsilon$ model constant                                    |
| $C_D$   | drag coefficient  |
| $d$     | diameter; nozzle diameter   |
| $D$     | molecular diffusion coefficient                                     |
| $E$     | Energy; energy spectrum   |
| $f$     | momentum transfer; filtered quantity                                |
| $F$     | LES filter; aerodynamic drag force                                  |
| $g$     | acceleration due to gravity   |
| $G$     | Gaussian probability density function; LES filter transfer function |
| $h$     | enthalpy  |
| $H$     | latent heat   |
| $I$     | modified Bessel functions   |
| $k$     | turbulent kinetic energy; sinusoidal perturbation wave number       |
| $K$     | conductivity coefficient; modified Bessel functions                 |
| $l$     | eddy length scale   |
| $L$     | length; lengthscale   |
| $m$     | mass  |
| $Nu$    | Nusselt number  |
| $p$     | pressure  |
| $P$     | Pressure  |
| $Pr$    | Prandtl number  |
| $Q$     | energy  |
| $r$     | radius  |
| $Re$    | Reynolds number   |
| $S$     | Rate of strain tensor   |
| $Sc$    | Schmidt number  |
| $Sh$    | Sherwood number   |
| $St$    | Stokes number   |
| $t$     | time  |
| $T$     | temperature; Taylor number  |

|       |   |
|-------|---|
| $u$   | local mean gas velocity   |
| $U$   | droplet - gas relative velocity   |
| $v$   | droplet velocity  |
| $V$   | volume, velocity  |
| $V_k$ | diffusion velocity  |
| $y$   | dimensionless displacement of droplet's surface from its equilibrium position |
| $W$   | turbulent dispersion source term  |
| $We$  | Weber number  |
| $x$   | spatial coordinate  |
| $Y$   | mass fraction   |
| $Z$   | Ohnesorge number  |

#### Greek Letters

|               |   |
|---------------|---|
| $\delta_{ij}$ | Kronecker delta   |
| $\Delta$      | filter cubic box size   |
| $\varepsilon$ | turbulent dissipation   |
| $\eta$        | ratio of turbulent to mean-strain time scale; sinusoidal perturbation amplitude |
| $\lambda$     | sinusoidal perturbation wavelength  |
| $\Lambda$     | sinusoidal perturbation wavelength for the maximum growth rate                  |
| $\mu$         | viscosity   |
| $\nu$         | kinematic viscosity   |
| $\rho$        | density   |
| $\sigma$      | surface tension between liquid and gas  |
| $\tau$        | shear stress; breakup time; droplet relaxation time                             |
| $\omega$      | droplet oscillation frequency;  |
| $\Omega$      | sinusoidal perturbation maximum growth rate                                     |

#### Subscripts

|               |   |
|---------------|---|
| $air$         | air   |
| $b$           | breakup   |
| $c$           | critical, characteristic  |
| $cell$        | cell  |
| $comb$        | combustion  |
| $d$           | droplet   |
| $drag$        | drag  |
| $\varepsilon$ | identify constants for the turbulent dissipation transport equation |
| $e$           | eddy, evaporation   |



|              |  |
|--------------|--|
| <i>f</i>     | frontal  |
| <i>h</i>     | heat transfer  |
| <i>hole</i>  | nozzle hole  |
| <i>i</i>     | index for vectorial component  |
| <i>inj</i>   | injection  |
| <i>j</i>     | index for vectorial component  |
| <i>g</i>     | gas phase  |
| <i>gas</i>   | gas phase  |
| <i>k</i>     | species <i>k</i> ; related to the turbulent kinetic energy model                   |
| <i>KH</i>    | related to Kelvin-Helmholtz breakup model  |
| <i>l</i>     | liquid phase   |
| <i>p</i>     | particle   |
| <i>rel</i>   | relative between droplet and gas   |
| <i>RT</i>    | related to Rayleigh-Taylor breakup model   |
| <i>s</i>     | sensible part; related to the spray, related to the turbulent kinetic energy model |
| <i>sgs</i>   | subgrid scale  |
| <i>spray</i> | due to spray   |
| <i>t</i>     | turbulent  |
| <i>vap</i>   | vaporization   |

#### Superscripts

|            |  |
|------------|--|
| '          | rate or time derivative                            |
| '          | derivative; fluctuation                            |
| ''         | fluctuation  |
| *          | value at the droplet's surface; intermediate value |
| -          | average value                                      |
| ~          | Favre average                                      |
| <i>sgs</i> | subgrid scale                                      |



## CONTENTS

|              |   |     |
|--------------|---|-----|
| <b>1</b>     | <b>INTRODUCTION</b> . . . . .   | 35  |
| 1.1          | OBJECTIVES AND CONTRIBUTIONS . . . . .  | 36  |
| 1.2          | DOCUMENT OVERVIEW . . . . .   | 37  |
| <b>2</b>     | <b>BACKGROUND AND LITERATURE REVIEW</b> . . . . .   | 39  |
| 2.1          | DIESEL ENGINE SPRAY PHYSICS . . . . .   | 39  |
| 2.2          | MATHEMATICAL MODELING FOR CONTINUUM PHASE FLOW . . . . .  | 41  |
| <b>2.2.1</b> | <b>LES Balance Equations and Its Closure Terms</b> . . . . .  | 42  |
| <b>2.2.2</b> | <b>URANS Balance Equations and Its Closure Terms</b> . . . . .  | 46  |
| 2.3          | MATHEMATICAL AND NUMERICAL MODELING FOR DISPERSED PHASE FLOW . . . . .                                    | 49  |
| <b>2.3.1</b> | <b>Spray Breakup</b> . . . . .  | 50  |
| 2.3.1.1      | Kelvin-Helmholtz Breakup Model . . . . .  | 50  |
| 2.3.1.2      | Rayleigh-Taylor Breakup Model . . . . .   | 52  |
| 2.3.1.3      | Combined KH-RT Breakup Model . . . . .  | 53  |
| <b>2.3.2</b> | <b>Droplet Drag Model</b> . . . . .   | 55  |
| <b>2.3.3</b> | <b>Spray Turbulence Interactions</b> . . . . .  | 57  |
| 2.3.3.1      | Standard Models for Spray-Turbulence Interactions . . . . .   | 57  |
| <b>2.3.4</b> | <b>Evaporation</b> . . . . .  | 59  |
| 2.3.4.1      | Single component droplet evaporation . . . . .  | 59  |
| <b>3</b>     | <b>THESIS PROPOSAL</b> . . . . .  | 63  |
| 3.1          | CURRENT MODELING LIMITATIONS . . . . .  | 63  |
| 3.2          | LES BASED MODELING . . . . .  | 69  |
| 3.3          | SPRAY TURBULENCE INTERACTION - PROPOSED GRID REFINEMENT APPROACH BASED ON DROPLET STOKES NUMBER . . . . . | 71  |
| 3.4          | NUMERICAL IMPLEMENTATIONS . . . . .   | 74  |
| <b>3.4.1</b> | <b>Droplet Stokes number numerical implementation</b> . . . . .   | 77  |
| <b>3.4.2</b> | <b>Other implementation issues</b> . . . . .  | 77  |
| <b>4</b>     | <b>SPRAY SIMULATION RESULTS</b> . . . . .   | 79  |
| 4.1          | EXPERIMENTAL CASES FROM SANDIA . . . . .  | 79  |
| 4.2          | NON-REACTING SPRAY SIMULATIONS . . . . .  | 83  |
| <b>4.2.1</b> | <b>Effect of Mesh Refinement and Parcel Number</b> . . . . .  | 85  |
| <b>4.2.2</b> | <b>Effect of STD and TAB models</b> . . . . .   | 91  |
| <b>4.2.3</b> | <b>Analysis based on <math>St_{sgs}</math> and proposed mesh refinement criterion</b> . . . . .           | 96  |
| 4.3          | LES TURBULENT KINETIC ENERGY RESOLUTION . . . . .   | 101 |

|          |   |            |
|----------|---|------------|
| 4.4      | COMPARISON BETWEEN RANS AND LES . . . . .   | 104        |
| <b>5</b> | <b>ANALYSES OF VESSEL CONDITIONS AND FUEL<br/>TYPE ON IMPORTANT SPRAY PARAMETERS AND<br/>ON MIXTURE FORMATION . . . . .</b> | <b>123</b> |
| 5.1      | MESH REFINEMENT CRITERION COMPARISON . . . . .  | 123        |
| 5.2      | VESSEL AMBIENT PRESSURE IMPACT . . . . .  | 129        |
| 5.3      | VESSEL AMBIENT TEMPERATURE IMPACT . . . . .   | 138        |
| 5.4      | COMPARISON BETWEEN nDODECANE ( $nC_{12}H_{26}$ ) VS.<br>nHEPTANE ( $nC_7H_{16}$ ) . . . . .                                 | 144        |
| <b>6</b> | <b>SUMMARY AND CONCLUSIONS . . . . .</b>  | <b>155</b> |
|          | <b>Bibliography . . . . .</b>   | <b>159</b> |

## 1 INTRODUCTION

Diesel engines are known for their higher fuel conversion efficiency, as a consequence of better thermal efficiency and reduced pumping work, as load control is obtained by fuel mass delivery to the engine and not by throttle control. This has led to this type of engine to be the most commonly used for large transportation vehicle applications, such as trucks and buses.

Environmental and health related concerns have led to the introduction of emission standards in the 1970s, and from that date on they have become more and more stringent, controlling oxides of Nitrogen (NO<sub>x</sub>), particulate matter (PM), Carbon monoxide (CO) and hydrocarbon (HC) emissions. Worries on fuel economy and greenhouse gas emissions (GHG) have led to legislation in 2007 proposing targets on CO<sub>2</sub> emissions, as well.

To meet these stringent targets, sometimes contradictory from a point of view of combustion products, various possibilities arise such as fuel technology (biofuels), engine design, aftertreatment systems, lubricants technology.

The trade-off between NO<sub>x</sub> and PM emissions is one of the most challenging, as the approach to reduce engine out PM emissions leads to increase in engine out NO<sub>x</sub> emissions, when operating under conventional diesel engine combustion. One example is the use of injection timing retard, which results in lower in-cylinder pressures and thus lower peak combustion temperatures, reducing NO<sub>x</sub> emissions. On the other hand this leads to higher PM due to improper fuel-air mixing and also lower fuel economy.

In production engines nowadays there exist two main possibilities to address this trade-off, (1) low engine out NO<sub>x</sub> emissions with PM emission aftertreatments; (2) low engine out PM emissions with NO<sub>x</sub> emission aftertreatments, the latter offering better results concerning fuel economy.

Biodiesel is also under the spotlight as a possibility to reduce emissions, but not without some drawbacks. Life cycle studies considering factors such as land use from cultivation of soybeans or rapeseed (carbon content in the soil, GHG emissions from fertilizers - N<sub>2</sub>O) have shown that the GHG emissions of biodiesel made from US Midwest soybean to be over three times higher than that of petroleum diesel, estimated with the same method (CASTANHEIRA; FREIRE, 2013; SEARCHINGER; HEIMLICH et al., 2008). Concerning tailpipe emissions, NO<sub>x</sub> has been found to be related to the test cycle condition, higher at high load than with petroleum diesel, mainly related to the lower heating value of biodiesel demanding higher fuel mass in order to reach the same required power output. Due to its oxygen content, oxidation of the fuel is better with biodiesel, leading to lower HC and CO

emissions. The total PM emissions is also related to the test cycle condition, but has been found to reduce in most of the performed studies (EPA, 2002).

The interaction between all the involved physical phenomena is quite complex, and reaching a correct engine design with the proper trade-offs only by experiments will be extremely time consuming and cost intensive. This is where computational fluid dynamics of engine in-cylinder process is gaining, over the past years, more importance as it can aid in dealing with all these interrelated factors in a faster and more cost effective way, allowing the better understanding of these processes and thus optimizing the engine for low emissions and high efficiency. However, spray combustion modeling is a very challenging task and a topic still open in the literature, with areas that still require improvements.

The review of current literature on fuel spray modeling approaches suggests that the usage of Large Eddy Simulation (LES) is of critical importance in order to represent the complex interactions between spray and turbulence, which affects all the physical processes related to mixture formation and combustion. In spite of some deficiencies related to the accuracy of non-reacting spray simulations, mainly concerning the adequate setup of different models and numerical parameters and, in particular, the mesh size, to adequately capture the interactions between spray and turbulence. This work presents the application of advanced turbulence modeling to the spray injection process in a static chamber, based on the implementation of a LES turbulence model in a Lagrangian spray based solver in OpenFOAM (open source code). Results that have been obtained hitherto for non-reacting sprays have proven that highly accurate results can be obtained for liquid and vapor length penetrations by correct modeling of spray phenomena and adequate mesh refinement to correctly capture turbulence-spray interactions. This work also contributes with a proposal for a new criterion based on the droplet Stokes number, for adaptive mesh refinement. This criterion also allows to assess to what extent the droplets' turbulent dispersion is properly captured for a given mesh size, using LES approach. A turbulence model comparison based on the averaged Navier Stokes equations (RANS), sensitivity analyses of ambient conditions in the static chamber and, the influence of the fuel's physical properties in important characteristics of non-reacting sprays are also explored.

## 1.1 OBJECTIVES AND CONTRIBUTIONS

In the review of the current literature on fuel spray modeling approaches, some deficiencies have been identified related to the accuracy of non-reacting spray simulations, that have been identified comparing the simulation results

to experiments. These deficiencies may also compromise the accuracy of combustion simulations. For example, an incorrectly high liquid length penetration can lead to excessive fuel impingement on cylinder walls and piston crown, and as a consequence in the mixture preparation and PM emissions. Also, an incorrect vapor penetration affects mixture preparation, altering ignition delay and rate of heat release. The rate of heat release, as a result of the combustion reaction, will affect in-cylinder temperature that can affect NO<sub>x</sub> emissions, as well as in-cylinder pressure, directly impacting the produced work in the cycle.

The main objective of this work is the numerical modeling of non-reacting spray process incorporating advanced turbulence models, that can provide accurate results for liquid and vapor length penetrations, as well as other important spray characteristics thus proving that, with proper modeling, algebraic models for turbulence and spray interaction are no longer required.

The methodology includes the following targets:

- Implementation of a LES turbulence model coupled to a Lagrangian tracking of the fuel droplets in the free platform OpenFOAM.
- Improve the current approach of LES for spray modeling leading to more accurate non-reacting spray predictions, detailing the impact of stochastic turbulence dispersion on the dispersion of the droplets, the effect of the number of Lagrangian parcels and Eulerian mesh size on statistical representation of droplet stochastic turbulence dispersion and the impact of the dynamic droplet distortion on droplet drag force.
- Implementation of a new refinement criterion, based on droplet Stokes number to be used for adaptive mesh refinement.
- Simulate the conditions prevailing in the constant volume non-reacting chamber, that are available in the Combustion Laboratory at SANDIA (US), and are published as a database for evaluation of the accuracy of simulation models for spray.
- Perform sensitivity analyses regarding vessel ambient pressure and temperature, and fuel type, with the objective to describe their impacts on important non-reacting spray characteristics, also comparing the results with known empirical correlations for liquid length penetration, spray angle and Sauter Mean Diameter (SMD).

## 1.2 DOCUMENT OVERVIEW

This thesis document is organized as follows:

- In chapter 2 a theoretical background and literature review is presented, showing the mathematical modeling for spray combustion.
- In chapter 3 a critical review of similar modeling approaches in literature is presented along with, the reasoning behind the modeling selection in this work and finally followed by the description of the thesis proposal and activities.
- In chapter 4 results obtained for non-reacting sprays are presented and discussed in view of the challenges of spray modeling in turbulent flow and the spray-turbulence interaction.
- In chapter 5 results for the vessel ambient pressure and temperature, and fuel type sensitivity analysis are presented and discussed with the empirical correlations for liquid length penetration, spray angle and SMD.
- Finally; in chapter 6 a summary and conclusion of the findings are presented.



## 2 BACKGROUND AND LITERATURE REVIEW

### 2.1 DIESEL ENGINE SPRAY PHYSICS

In this section it will be described briefly the mixture formation process with a direct injection (DI) fuel injector with its characteristics and spray break-up process.

In Fig. 1, a schematic of the injection break-up and evaporation processes of a full-cone diesel spray is shown.

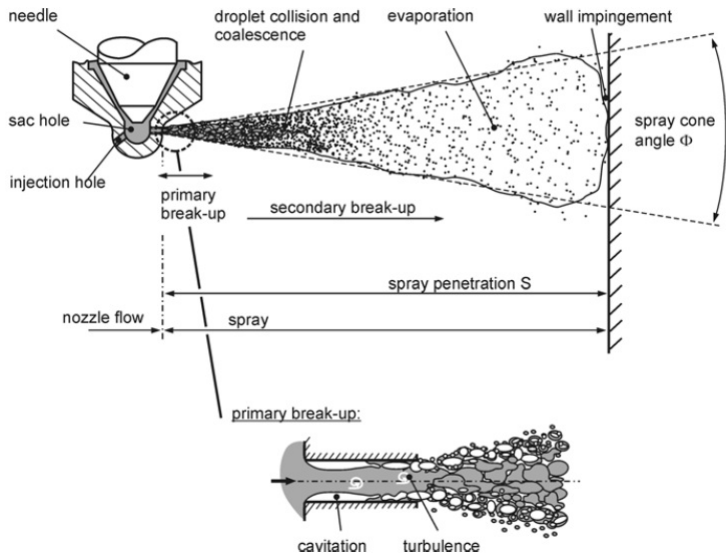


Figure 1 – Schematic of a full cone injector spray. Source: Baumgarten (2006)

At the exit of the nozzle orifice the jet starts to break-up in ligaments and bigger drops, due to the high pressures in the injection leading to cavitation and turbulence that initiates inside the nozzle (primary break-up process). Due to the velocity difference between the droplets and the surrounding gas, aerodynamic forces induce the growth of instabilities in the liquid-gas interface, which lead to the secondary break-up in smaller diameter droplets. These smaller droplets are affected by the temperature, density and flow struc-

ture in the surroundings which leads to the evaporation process. In the dense region of the spray collision between droplets are likely to occur, leading to new break-up of them or the coalescence forming bigger droplets. Depending on the injection time and its duration, the spray may impinge in the cylinder wall and piston crown with the formation of liquid film puddle.

The sac hole size defines the volume of fuel remaining inside the injector from the previous injection event. As this fuel is not at the fuel line pressure, it will impact the new injection process by delaying the injecting fuel acceleration.

The fuel spray tip penetration ( $S$ ) and its cone angle ( $\Phi$ ) are important parameters that characterize its operation.

An important characteristic of this type of injector, compared to other types such as hollow-cone sprays, is that neither its spray structure nor its cone angle change significantly with changing the surroundings' pressure, as will be shown in section 5.2. The spray shape can be modified by changing the position and number of orifices.

Photo of a multi-hole injector spray in engine like conditions is shown in Fig. 2, where in addition to the processes described above there is some interaction between the various jets, which adds complexity to it.

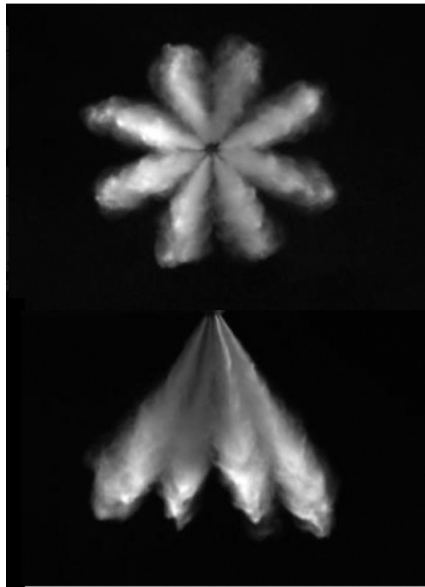


Figure 2 – Multi-hole fuel injector spray. Source: Smith et al. (2011)

## 2.2 MATHEMATICAL MODELING FOR CONTINUUM PHASE FLOW

In this section it will be presented a basic description of the instantaneous balance equations for the continuum phase using the Eulerian referential, followed by a brief description of LES turbulence modeling. As RANS turbulence modeling is a common practice in industrial applications for internal combustion engine simulations, it will also be presented briefly in this chapter and later, in section 4.4, results obtained with this approach will be compared against LES turbulence modeling approach. For the dispersed phase, modeled with Lagrangian approach, the complex models for primary and secondary breakup, evaporation, and other phenomena regarding the spray-gas interaction will also be covered in the following sections.

The Euler referential is used to describe the gas phase flow which instantaneous balance equations, as described by Poinso and Veynante (2005), with added source terms for spray and combustion are presented below.

The balance equation for species  $k$  is given by,

$$\frac{\partial (\rho Y_k)}{\partial t} + \frac{\partial (\rho u_i Y_k)}{\partial x_i} = - \frac{\partial}{\partial x_i} (V_{k,i} Y_k) + \dot{\rho}_{k,spray} + \dot{\rho}_{k,comb} \quad (2.1)$$

In this equation  $\rho$  is the density,  $Y_k$  is the species mass fraction,  $u$  is velocity and  $V_{k,i}$  is the  $i$ - component of the diffusion velocity of species  $k$ ,  $V_k$ . The diffusion velocity leads to Fick's law. For example, species laminar diffusion fluxes,

$$V_{k,i} Y_k = -\rho D_k \frac{\partial Y_k}{\partial x_i}, \quad (2.2)$$

where  $D_k$  is the species molecular diffusion coefficient.

The first term in the right hand side in Eq. 2.1 accounts for species mass diffusion, the second term is the time rate of change of species density from the interaction with the spray, and the last term is the time rate of change of species density due to chemical reactions.

Summing Eq. 2.1 over all species the total gas mass conservation equation is obtained,

$$\frac{\partial \rho}{\partial t} + \frac{\partial (\rho u_i)}{\partial x_i} = \dot{\rho}_{spray} \quad (2.3)$$

As the total mass of the gas phase does not change with combustion, the combustion source term does not appear in Eq. 2.3. Nevertheless, a mass source for the total gas phase appears which represents the evaporation of liquid droplets.

The momentum balance equation is given by,

$$\frac{\partial (\rho u_j)}{\partial t} + \frac{\partial (\rho u_i u_j)}{\partial x_i} = -\frac{\partial p}{\partial x_j} + \frac{\partial \tau_{ij}}{\partial x_i} + \rho g_j + f_{j,spray} \quad (2.4)$$

In this equation  $p$  is the pressure and  $\tau_{ij}$  is the shear stress tensor. The second term on the right hand side accounts for the momentum transfer due to friction, the third term accounts for body forces and the last term is the interfacial momentum transfer per unit volume due to the interaction with the spray.

The energy balance equation, in terms of enthalpy, is given by,

$$\begin{aligned} \frac{\partial (\rho h_s)}{\partial t} + \frac{\partial (\rho u_i h_s)}{\partial x_i} = & \frac{Dp}{Dt} + \tau_{ij} \frac{\partial u_i}{\partial x_j} + \frac{\partial}{\partial x_i} \left( K_t \frac{\partial T}{\partial x_i} \right) \\ & - \frac{\partial}{\partial x_i} \left( \rho \sum_{k=1}^N V_{k,i} Y_k h_{s,k} \right) + \dot{Q}_{spray} + \dot{Q}_{comb} \end{aligned} \quad (2.5)$$

In this equation  $h_s$  is the sensible enthalpy,  $K_t$  is the turbulent thermal conductivity coefficient,  $T$  is the temperature and  $h_{s,k}$  is the sensible enthalpy of species  $k$ . The first term in the right hand side is a consequence of the work done per unit time by pressure forces, the second term is a consequence of the work done per unit time by viscous forces, the third term is a consequence of heat conduction, the fourth term is the consequence of enthalpy transfer due to mass diffusion of species, and the last two terms include source terms from spray interaction and chemical heat release.

## 2.2.1 LES Balance Equations and Its Closure Terms

Large Eddy Simulations (LES) equations are obtained by filtering the instantaneous balance equations. The filter provides scale separation between the energy containing eddies (large scales) that are resolved, and the small scales responsible for viscous transformation (subgrid scale, SGS) that are modeled. The impact of the large flow structures on mixing, and their unsteady interactions with the combustion is one advantage of LES over RANS (POINSOT; VEYNANTE, 2005; ECHEKKI; MASTORAKOS, 2011).

There are spectral and spatial LES filters. The box filter is a spatial filter that weight averages over a given volume defined by a cubic box of size  $\Delta$ , which essentially corresponds to a characteristic size of the mesh used

for the numerical solution of the equations, given by Eq. 2.7. The filtered quantity  $f$  is defined as,

$$\bar{f}(x) = \int f(x') F(x-x') dx', \quad (2.6)$$

where  $F$  is the LES filter defined as,

$$F(x) = F(x_i) = \begin{cases} \frac{1}{\Delta^3} & \text{if } |x_i| \leq \frac{\Delta}{2}, i = 1, 2, 3 \\ 0 & \text{otherwise} \end{cases} \quad (2.7)$$

and  $x$  is the position in space.

Now defining the Favre average as,

$$\tilde{f} = \frac{\bar{\rho} f}{\bar{\rho}}, \quad (2.8)$$

where the overbar (e.g.  $\bar{\rho}$ ) means the Reynolds mean, any quantity  $f$  may be split into mean and fluctuating components as:

$$f = \tilde{f} + f'' \quad \text{with} \quad \overline{f''} = 0 \quad (2.9)$$

Resulting in the filtered balance equations for mass,

$$\frac{\partial \bar{\rho}}{\partial t} + \frac{\partial (\bar{\rho} \tilde{u}_i)}{\partial x_i} = \bar{\rho}_{spray} \quad (2.10)$$

momentum,

$$\frac{\partial (\bar{\rho} \tilde{u}_j)}{\partial t} + \frac{\partial (\bar{\rho} \tilde{u}_i \tilde{u}_j)}{\partial x_i} = -\frac{\partial \bar{p}}{\partial x_j} + \frac{\partial}{\partial x_i} [\bar{\tau}_{ij} - \bar{\rho} (\widetilde{u_i u_j} - \tilde{u}_i \tilde{u}_j)] + \bar{\rho} g + \bar{f}_{j,spray} \quad (2.11)$$

species,

$$\frac{\partial (\bar{\rho} \tilde{Y}_k)}{\partial t} + \frac{\partial (\bar{\rho} \tilde{u}_i \tilde{Y}_k)}{\partial x_i} = \frac{\partial}{\partial x_i} [\overline{V_{k,i} Y_k} + \bar{\rho} (\widetilde{u_i Y_k} - \tilde{u}_i \tilde{Y}_k)] + \bar{\rho}_{k,spray} + \bar{\rho}_{k,comb} \quad (2.12)$$

and enthalpy,

$$\begin{aligned} \frac{\partial (\bar{\rho} \tilde{h}_s)}{\partial t} + \frac{\partial (\bar{\rho} \tilde{u}_i \tilde{h}_s)}{\partial x_i} = \frac{D\bar{p}}{Dt} + \overline{\tau_{ij} \frac{\partial u_i}{\partial x_j}} + \frac{\partial}{\partial x_i} \left[ \overline{K_t \frac{\partial T}{\partial x_i}} - \bar{\rho} (\widetilde{u_i h_s} - \tilde{u}_i \tilde{h}_s) \right] \\ - \frac{\partial}{\partial x_i} \left( \overline{\rho \sum_{k=1}^N V_{k,i} Y_k h_{s,k}} \right) + \bar{Q}_{s\text{pray}} + \bar{Q}_{c\text{omb}} \end{aligned} \quad (2.13)$$

where

$$\frac{D\bar{p}}{Dt} = \frac{\partial \bar{p}}{\partial t} + u_i \frac{\partial \bar{p}}{\partial x_i} \quad (2.14)$$

In Eq. 2.13 both work done per unit time by viscous forces ( $\overline{\tau_{ij} \partial u_i / \partial x_j}$ ) and enthalpy transfer due to mass diffusion of species ( $\overline{V_{k,i} Y_k h_{s,k}}$ ) were neglected, against the other work terms and the turbulent transport that are orders of magnitude higher (POINSOT; VEYNANTE, 2005), and thus have not been implemented in the LES solver in this work.

The closure terms for the unknown terms from Eq. 2.10 to 2.13 are shown below.

The Reynold stress ( $\widetilde{u_i u_j} - \tilde{u}_i \tilde{u}_j$ ) requires a subgrid scale turbulence model for closure and is given by the subgrid scale shear stress tensor  $\tau_{ij}^{sgs}$ .

One of the simplest models to close the equations for the filtered velocity was proposed by Smagorinsky (1963), where the inherent assumption of balance between the subgrid scale energy production and dissipation rate, requires fine grids in order not to be violated, as the subgrid model needs to model the effect of the unresolved scales, and with a coarse grid a relevant amount of turbulent kinetic energy may still be present in the subgrid scales, as will be seen in section 4.3. If this happens there is also a possibility of a significant reverse energy cascade from the subgrid scales to the resolved scales (MENON; YEUNG; KIM, 1996).

In the Smagorinsky's eddy viscosity model the subgrid scale shear stress tensor is given by,

$$\tau_{ij}^{sgs} - \frac{\delta_{ij}}{3} \tau_{kk} = -\nu_t \left( \frac{\partial \bar{u}_i}{\partial x_j} + \frac{\partial \bar{u}_j}{\partial x_i} \right) = -2\nu_t \bar{S}_{ij}, \quad (2.15)$$

where  $\delta_{ij}$  is the Kronecker delta,  $\bar{S}_{ij}$  is the filtered strain rate tensor and the subgrid scale turbulent viscosity is given by,

$$\nu_t = (C_s \Delta)^2 \bar{S}_{ij}, \quad (2.16)$$

where  $C_s$  is a model constant that varies with the type of flow regime and the

numerical method. To overcome the limitation related to the constant ( $C_s$ ), Germano et al. (1991) proposed a method to calculate and update a more adequate Smagorinsky constant based on the local flow regime, the dynamic subgrid scale eddy viscosity model.

An improvement to address the potential issues with the zero-equation LES Models, is the adoption of a higher order model that solves a transport equation for the subgrid kinetic energy. The One Equation Eddy Viscosity Model for compressible flows proposed by Yoshizawa and Horiuti (1985), including the terms to account for the interaction with the spray, is given by,

$$\frac{\partial (\bar{\rho} k_{sgs})}{\partial t} + \frac{\partial (\bar{\rho} \tilde{u}_i k_{sgs})}{\partial x_i} = \overline{\tau_{ij} \frac{\partial u_i}{\partial x_j}} + \frac{\partial}{\partial x_j} \left[ (\mu + \mu_t) \frac{\partial k_{sgs}}{\partial x_j} \right] - \bar{\rho} C_\varepsilon \frac{k_{sgs}^{3/2}}{\Delta} + \bar{W}_s \quad (2.17)$$

In this equation  $C_\varepsilon$  is a model constant, and  $\bar{W}_s$  is a source term that comes from the interaction of the turbulence with the spray, and will be discussed in section 2.3.3. The first term on the right hand side is the production term, the second term accounts for diffusion and the third term on the right hand side accounts for the dissipation of the turbulent kinetic energy.

This model is not based on the local balance between the subgrid scale energy production and dissipation rate, as the Smagorinsky model, so it is expected to be better in regions where local balance is violated (MENON; YEUNG; KIM, 1996).

The subgrid scale shear stress tensor is given by,

$$\tau_{ij}^{sgs} = -2\nu_k \bar{\delta}_{ij} + \frac{2}{3} k_{sgs} \delta_{ij}, \quad (2.18)$$

and the subgrid scale turbulent viscosity  $\nu_k$ ,

$$\nu_k = C_k k_{sgs}^{1/2} \Delta, \quad (2.19)$$

where  $C_k$  is a model constant.

The model with an additional transport equation for the subgrid kinetic energy ( $k_{sgs}$ ) have shown benefits over the traditional zero equation models such as Smagorinsky, being less dissipative and less dependent on extremely refined grids, thus more adequate to industrial application (LEE; POMRANING; RUTLAND, 2002; SONE; MENON, 2003; RUTLAND, 2009, 2011).

The species ( $\widetilde{u_i Y_k} - \tilde{u}_i \tilde{Y}_k$ ) and enthalpy ( $\widetilde{u_i h_s} - \tilde{u}_i \tilde{h}_s$ ) subgrid scale turbulent fluxes are closed using a classical gradient assumption,

$$\widetilde{u_i Y_k} - \tilde{u}_i \tilde{Y}_k = - \frac{\mu_t}{Sc_{tk}} \frac{\partial \tilde{Y}_k}{\partial x_i} \quad (2.20)$$

$$\widetilde{u_i h_s} - \widetilde{u_i} \widetilde{h_s} = -\frac{\mu_t}{Pr_t} \frac{\partial \widetilde{h_s}}{\partial x_i}, \quad (2.21)$$

where  $Sc_{tk}$  and  $Pr_t$  are the subgrid scale Schmidt for species  $k$  and Prandtl numbers, respectively.

The diffusive fluxes for species ( $\overline{V_{k,i} Y_k}$ ) are usually neglected against the turbulent transport and have not been implemented in the LES solver for this work.

The diffusive flux for enthalpy  $\left( \overline{K_t \frac{\partial T}{\partial x_i}} \right)$ , can be modeled as,

$$\overline{K_t \frac{\partial T}{\partial x_i}} = \overline{K_t} \frac{\partial \widetilde{T}}{\partial x_i} \quad (2.22)$$

The pressure-velocity correlation term  $\left( \overline{u_i \frac{\partial p}{\partial x_i}} \right)$  from Eq. 2.14 is approximated by  $\widetilde{u_i} \frac{\partial \bar{p}}{\partial x_i}$ .

## 2.2.2 URANS Balance Equations and Its Closure Terms

Unsteady Reynolds Averaged Navier Stokes (URANS) equations are obtained by averaging the instantaneous balance equations. This averaging process impacts on all space and time scales, and will solve for the mean values of all quantities, and no turbulent motion is explicitly captured.

Resulting in the Favre averaged balance equations for mass,

$$\frac{\partial \bar{\rho}}{\partial t} + \frac{\partial (\bar{\rho} \widetilde{u_i})}{\partial x_i} = \bar{\rho}_{spray} \quad (2.23)$$

momentum,

$$\frac{\partial (\bar{\rho} \widetilde{u_j})}{\partial t} + \frac{\partial (\bar{\rho} \widetilde{u_i} \widetilde{u_j})}{\partial x_i} = -\frac{\partial \bar{p}}{\partial x_j} + \frac{\partial}{\partial x_i} \left( \bar{\tau}_{ij} - \bar{\rho} \widetilde{u_i'' u_j''} \right) + \bar{\rho} g + \bar{f}_{j,spray} \quad (2.24)$$

species,

$$\frac{\partial (\bar{\rho} \widetilde{Y_k})}{\partial t} + \frac{\partial (\bar{\rho} \widetilde{u_i} \widetilde{Y_k})}{\partial x_i} = -\frac{\partial}{\partial x_i} \left( \overline{V_{k,i} Y_k} + \bar{\rho} \widetilde{u_i'' Y_k''} \right) + \bar{\rho}_{k,spray} + \bar{\rho}_{k,comb} \quad (2.25)$$



and enthalpy,

$$\begin{aligned} \frac{\partial (\bar{\rho} \tilde{h}_s)}{\partial t} + \frac{\partial (\bar{\rho} \tilde{u}_i \tilde{h}_s)}{\partial x_i} &= \frac{D\bar{p}}{Dt} + \overline{\tau_{ij} \frac{\partial u_i}{\partial x_j}} + \frac{\partial}{\partial x_i} \left( \overline{K_t \frac{\partial T}{\partial x_i}} - \bar{\rho} \tilde{u}_i'' \tilde{h}_s'' \right) \\ &\quad - \frac{\partial}{\partial x_i} \left( \overline{\rho \sum_{k=1}^N V_{k,i} Y_k h_{s,k}} \right) + \bar{Q}_{spray} + \bar{Q}_{comb} \end{aligned} \quad (2.26)$$

where,

$$\frac{D\bar{p}}{Dt} = \frac{\partial \bar{p}}{\partial t} + \tilde{u}_i \frac{\partial \bar{p}}{\partial x_i} + \overline{u_i'' \frac{\partial p}{\partial x_i}} \quad (2.27)$$

In Eq. 2.26 both work done per unit time by viscous forces ( $\overline{\tau_{ij} \partial u_i / \partial x_j}$ ) and enthalpy transfer due to mass diffusion of species ( $\overline{V_{k,i} Y_k h_{s,k}}$ ) are neglected in the original implementation in OpenFOAM.

The closure terms for the unknown terms from Eq. 2.23 to 2.26 are shown below.

The Reynolds stress ( $\overline{u_i'' u_j''}$ ) is closed with a turbulence model described by the shear stress tensor  $\tau_{ij}$ ,

$$\tilde{\tau}_{ij} = \mu_t \left( \frac{\partial \tilde{u}_i}{\partial x_j} + \frac{\partial \tilde{u}_j}{\partial x_i} \right) - \frac{2}{3} \delta_{ij} \left( \bar{\rho} k + \mu_t \frac{\partial \tilde{u}_i}{\partial x_i} \right); \quad (2.28)$$

based on the Boussinesq hypothesis using the turbulent viscosity  $\mu_t$  concept,

$$\mu_t = C_\mu \rho \frac{k^2}{\varepsilon}, \quad (2.29)$$

where  $C_\mu$  is a model constant.

To be able to obtain both  $\tau_{ij}$  and  $\mu_t$  it is required to have transport equations for the turbulent kinetic energy ( $k$ ) and for the turbulent dissipation ( $\varepsilon$ ). A modification to the original  $k - \varepsilon$  turbulence model from Jones and Launder (1972) to account for compressibility effects found in internal combustion engines, including a term to account for the interaction between the spray and the turbulent structure is used.

In the two equation  $k - \varepsilon$  (JONES; LAUNDER, 1972) the turbulent kinetic energy ( $k$ ) transport equation is given by,

$$\frac{\partial (\bar{\rho} k)}{\partial t} + \frac{\partial (\bar{\rho} \tilde{u}_i k)}{\partial x_i} = \overline{\tau_{ij} \frac{\partial u_i}{\partial x_j}} + \frac{\partial}{\partial x_j} \left[ \left( \mu + \frac{\mu_t}{\sigma_k} \right) \frac{\partial k}{\partial x_j} \right] - \bar{\rho} \varepsilon + \bar{W}_s \quad (2.30)$$

In this equation  $\sigma_k = 1.0$  is a model constant, and  $\tilde{W}_s$  is a source term that arises from the interaction of the turbulence with the spray.

The turbulent dissipation ( $\varepsilon$ ) transport equation, incorporating the Rapid Distortion Theory contribution via the second term in the right hand side, is given by,

$$\begin{aligned} \frac{\partial(\bar{\rho}\varepsilon)}{\partial t} + \frac{\partial(\bar{\rho}\tilde{u}_i\varepsilon)}{\partial x_i} = \frac{\partial}{\partial x_j} \left[ \left( \mu + \frac{\mu_t}{\sigma_\varepsilon} \right) \frac{\partial \varepsilon}{\partial x_j} \right] - C_{\varepsilon 3} \bar{\rho} \varepsilon \frac{\partial \tilde{u}_i}{\partial x_i} \\ + \left( C_{\varepsilon 1} \overline{\tau_{ij} \frac{\partial u_i}{\partial x_j}} - C_{\varepsilon 2} \bar{\rho} \varepsilon + c_s \overline{W}_s \right) \frac{\varepsilon}{k} \end{aligned} \quad (2.31)$$

In this equation  $\sigma_\varepsilon = 1.3$ ,  $C_{\varepsilon 1} = 1.44$ ,  $C_{\varepsilon 2} = 1.92$ ,  $C_{\varepsilon 3} = -0.33$  and  $c_s = 1.0$  are model constants.

The species ( $\widetilde{u_i'' Y_k''}$ ) and enthalpy ( $\widetilde{u_i'' h_s''}$ ) turbulent fluxes are closed using a classical gradient assumption,

$$\bar{\rho} \widetilde{u_i'' Y_k''} = - \frac{\mu_t}{Sc_{kt}} \frac{\partial \tilde{Y}_k}{\partial x_i} \quad (2.32)$$

$$\bar{\rho} \widetilde{u_i'' h_s''} = - \frac{\mu_t}{Pr_t} \frac{\partial \tilde{h}_s}{\partial x_i}, \quad (2.33)$$

where  $Sc_{kt}$  and  $Pr_t$  are the turbulent Schmidt number for species  $k$  and Prandtl number, respectively.

The diffusive fluxes for species ( $\overline{V_{k,i} Y_k}$ ) are usually neglected against the turbulent transport, but can be modeled as,

$$\overline{V_{k,i} Y_k} = - \bar{\rho} \bar{D}_k \frac{\partial \tilde{Y}_k}{\partial x_i} \quad (2.34)$$

The diffusive flux for enthalpy  $\left( \overline{K_t \frac{\partial T}{\partial x_i}} \right)$ , can be modeled as,

$$\overline{K_t \frac{\partial T}{\partial x_i}} = \bar{K}_t \frac{\partial \tilde{T}}{\partial x_i} \quad (2.35)$$

In Eq. 2.34  $\bar{D}_k$  is the mean species molecular diffusion coefficient and in Eq. 2.35  $\bar{K}_t$  is the mean turbulent thermal conductivity coefficient.

The pressure-velocity correlation  $\left( \overline{u_i'' \frac{\partial p}{\partial x_i}} \right)$  from Eq. 2.27 is orders of magnitude smaller than the other terms and thus is neglected.

## 2.3 MATHEMATICAL AND NUMERICAL MODELING FOR DISPERSED PHASE FLOW

In this section, the equations for the motion, heat and mass transfer of the liquid phase, flowing as spray, are presented in a Lagrangian referential, which will be used to describe its motion. In addition, the closure models for the interfacial transport between phases, including the turbulence effects, are discussed.

For the modeling of the spray, the Monte-Carlo Method is employed, i.e., instead of dealing with all the droplets present in the spray, only a small amount of them are solved in detail to obtain an approximated solution that will represent the overall solution for the spray. The assumption is that the behavior for this subset of droplets are representative of all droplets in the spray.

In the Lagrangian method the spray is then described by a discrete number of parcels, where each one of them contains a number of droplets with the same size, temperature, velocity and fuel properties that are a statistic representation of the total number of the droplets in the spray (DUKOWICZ, 1980).

An equation of motion is solved for every parcel in the domain, as

$$\rho_l V_d \frac{dv_i}{dt} = C_D A_f \frac{\rho_g |U_i|}{2} U_i + \rho_l V_d g_i, \quad (2.36)$$

in this equation  $\rho_l$  is the liquid density,  $V_d$  is the droplet volume,  $v_i$  is the droplet velocity,  $C_D$  is the drag coefficient,  $A_f$  is the droplet frontal area,  $\rho_g$  is the gas density,  $g_i$  is the gravitational acceleration and  $U_i$  is the drop-gas relative velocity defined as,

$$U_i = u_i + u'_i - v_i \quad (2.37)$$

In this equation  $u_i$  is the local mean gas velocity and  $u'_i$  is the local turbulent fluctuation gas velocity.

The first term on the right hand side of Eq. 2.36 is a consequence of drag forces and the second term is a consequence of gravitational body forces. As the ratio between the dispersed and continuous phase densities is of order  $10^2$  or higher, other forces such as buoyancy, Basset, and so on, are of lesser importance and thus neglected (NORDIN, 2001).

To update the parcel velocity Eq. 2.36 is rewritten and implemented in OpenFOAM as,

$$\frac{dv_i}{dt} = \frac{|U_i|}{\tau_u} + g_i \quad (2.38)$$

where the momentum relaxation time is defined as,

$$\tau_u = \frac{4\rho_l d_d}{3\rho_g C_D U_i} \quad (2.39)$$

### 2.3.1 Spray Breakup

As shown in Fig. 1 the spray breakup is divided in primary and secondary. For primary breakup the simplest and most popular is the Blob method from Reitz (1987) that considers in the dense spray region the injection of big spherical drops that are latter subjected to secondary aerodynamic induced breakup. Huh and Gosman (1991) proposed an extension to that model to include also the turbulence effects, leading to surface instabilities that will be augmented by the aerodynamic forces and produce the first droplets. Arcoumanis, Gavaises and French (1997) proposed a model that includes in addition to the above phenomena of aerodynamic instabilities and turbulence, cavitation in the big spherical droplets injected by the Blob method.

Secondary breakup is caused by aerodynamic forces on the droplets already injected in the primary breakup. The Taylor Analogy Breakup (TAB) from O'Rourke and Amsden (1987) is based on a spring-mass system and an oscillating droplet (Fig. 7), but it is known to under-predict droplet sizes (TANNER, 1997) and to underestimate spray penetration (PARK; KIM; LEE, 2002). The KH breakup model proposed by Reitz (1987) can also be used for secondary breakup. The Rayleigh-Taylor breakup model based on the work from Taylor (1963) analyzing the surface instabilities as a consequence of acceleration/deceleration of the droplets as it moves in the gas stream, is another used method.

#### 2.3.1.1 Kelvin-Helmholtz Breakup Model

The KH breakup model (REITZ, 1987) is based on the KH instabilities growing in the interface of a cylindrical liquid jet with initial radius  $r_0$  that is penetrating into a stationary incompressible gas with a relative velocity  $u_{rel} = |u_i - v_i|$  (Fig. 3). Note that the fluctuating velocity component is not considered.

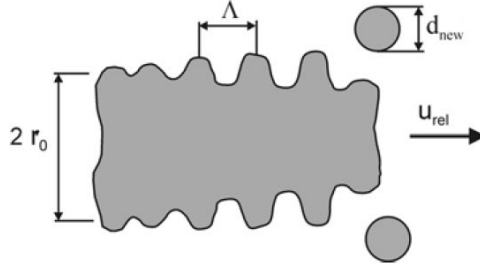


Figure 3 – Kelvin Helmholtz model. Source: Baumgarten (2006).

This model also considers both liquid and gas as incompressible and the gas also as inviscid. Due to inner nozzle flow it is assumed that there are infinitesimal sinusoidal perturbations on the liquid surface with initial amplitude  $\eta_0$ , with wavelengths  $\lambda$ , with wave number  $k = 2\pi/\lambda$ .

The analysis results in a dispersion equation relating the growth rate ( $\omega$ ) of a perturbation to its wavelength ( $\lambda$ ),

$$\omega^2 + 2\nu_l k^2 \omega \left[ \frac{I_1'(kr_0)}{I_0(kr_0)} - \frac{2kl}{k^2 + l^2} \frac{I_1(kr_0)}{I_0(kr_0)} \frac{I_1'(lr_0)}{I_1(lr_0)} \right] = \frac{\sigma k}{\rho_l r_0^2} \left(1 - k^2 r_0^2\right) \left(\frac{l^2 - k^2}{l^2 + k^2}\right) \frac{I_1(kr_0)}{I_0(kr_0)} + \frac{\rho_g}{\rho_l} \left(u_{rel} - \frac{i\omega}{k}\right)^2 k^2 \left(\frac{l^2 - k^2}{l^2 + k^2}\right) \frac{I_1(kr_0)K_0(kr_0)}{I_0(kr_0)K_1(kr_0)}, \quad (2.40)$$

in this dispersion equation  $I_0$  and  $I_1$  are modified Bessel functions of the first kind,  $K_0$  and  $K_1$  are modified Bessel functions of the second kind,  $\sigma$  is the surface tension,  $l^2 - k^2 = \omega/\nu_l$ ,  $\nu_l = \mu_l/\rho_l$  is the kinematic viscosity, and the prime indicates differentiation.

The maximum growth rate is obtained from the solution of Eq. 2.40,

$$\Omega \left[ \frac{\rho_l r_0^3}{\sigma} \right] = \frac{0.34 + 0.38 We_g^{1.5}}{(1 + Z_l)(1 + 1.4T^{0.6})}, \quad (2.41)$$

and its corresponding wavelength,

$$\frac{\Lambda}{r_0} = 9.02 \frac{(1 + 0.45Z_l^{0.5})(1 + 0.4T^{0.7})}{(1 + 0.865We_g^{1.67})^{0.6}} \quad (2.42)$$

In the equations above,  $Z_l = \sqrt{We_l}/Re_l$  is the Ohnesorge number and

$T = Z_l \sqrt{We_g}$  is the Taylor number. The liquid Weber number is  $We_l = \rho_l r_0 u_{rel}^2 / \sigma$ , the gas Weber number is  $We_g = \rho_g r_0 u_{rel}^2 / \sigma$  and Reynolds number for the liquid is  $Re_l = r_0 u_{rel} / \nu_l$ .

In the KH breakup model, the initial parcel diameters are set equal to the nozzle hole diameter  $d_0$  and the atomization of the injected "blobs" is modeled assuming that the breakup drop radius,

$$r_{KH} = B_0 \Lambda, \quad (2.43)$$

is proportional to the wavelength of the fastest growing unstable surface wave  $\Lambda$ .

In this equation  $B_0$  is a model constant equal to 0.61.

The rate of change of drop radius due to breakup is obtained as,

$$\frac{dr_0}{dt} = -\frac{(r_0 - r)}{\tau_{KH}} \quad \text{where } (r \leq r_0), \quad (2.44)$$

where the breakup time is,

$$\tau_{KH} = \frac{3.726 B_1 r_0}{\Lambda \Omega}. \quad (2.45)$$

In this equation the breakup time constant  $B_1$  is related to the initial disturbance on the liquid jet and has been found to vary from one injector to another (usually within the 5 – 100 range), and is important to characterize the initial spray injection ramp.

As the droplet breaks-up, its velocity component normal to the path of the parent drop is obtained as,

$$V_{nKH} = C_1 \Lambda \Omega. \quad (2.46)$$

In this equation  $C_1$  is a model constant equal to 0.188 (REITZ, 1987).

### 2.3.1.2 Rayleigh-Taylor Breakup Model

The Rayleigh-Taylor breakup model is based on the growth of unstable waves on the interface between two fluids of different densities due to rapid acceleration or deceleration normal to this interface (Fig. 4). The disintegration of the drop is induced by the inertia of the liquid as it leaves the nozzle with high velocity and is decelerated by the aerodynamic drag force,

$$F_{D,i} = m_d \frac{3}{8} C_D \frac{\rho_g |U_i|^2}{\rho_l r_0} \quad (2.47)$$

In Eq. 2.47  $m_d$  is the droplet mass.

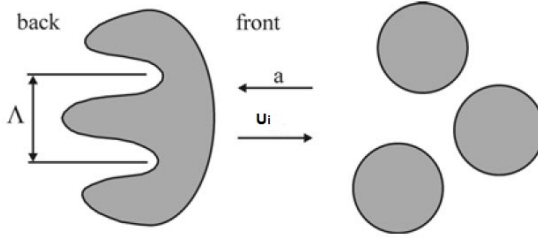


Figure 4 – Rayleigh-Taylor instability on a liquid drop. Source: Baumgarten (2006).

Typical implementations of the RT breakup model neglect both gas and liquid viscosity, as presented in Patterson and Reitz (1998), where the growth rate ,

$$\Omega_{RT} = \sqrt{\frac{2}{3\sqrt{3}\sigma} \frac{[a(\rho_l - \rho_g)]^{3/2}}{\rho_l + \rho_g}}, \quad (2.48)$$

and the corresponding wavelength,

$$\Lambda_{RT} = C_{RT} 2\pi \sqrt{\frac{3\sigma}{a(\rho_l - \rho_g)}}, \quad (2.49)$$

of the fastest growing wave are obtained.

In the above equations  $C_{RT}$  is a model size constant usually ranging from 1 – 5.33 and  $a$  is the acceleration of the interface that can be easily calculated from Eq. 2.47 by dividing it by the droplet mass.

The size of the new droplets are assumed proportional to the wavelength ( $d_{RT} = \Lambda_{RT}$ ) and the breakup time inversely proportional to the growth rate ( $\tau_{RT} = C_\tau * \Omega^{-1}$ ), where  $C_\tau$  is a time constant equal to 1. When the time equals the breakup time the droplets disintegrates to the size  $d_{RT}$ .

### 2.3.1.3 Combined KH-RT Breakup Model

A single breakup mechanism is not capable of predicting the process in engine sprays, so more than one model is usually used in combination. For example, the RT breakup model predicts too fast breakup of droplets, while the KH breakup model predicts equally sized droplets with intermediate size.

Therefore a combined KH-RT breakup model is then preferred. There are two KH-RT breakup model implementations available in OpenFOAM.

One implementation have both models competing during the whole injection process. In this approach,  $\Lambda_{RT}$  is calculated and compared to the parcel size. If the parcel size is larger than  $\Lambda_{RT}$ , then it starts to track for how long the RT waves are growing in the parcel surface. If this time is larger than  $\tau_{RT}$  the parcels will undergo the breakup according to the RT model. Otherwise, if the time is shorter than  $\tau_{RT}$ , and the parcel diameter is larger than  $2 * r_{KH}$ , then the parcel will undergo breakup according to the KH model, if the time is larger than the  $\tau_{KH}$  (Fig. 5).

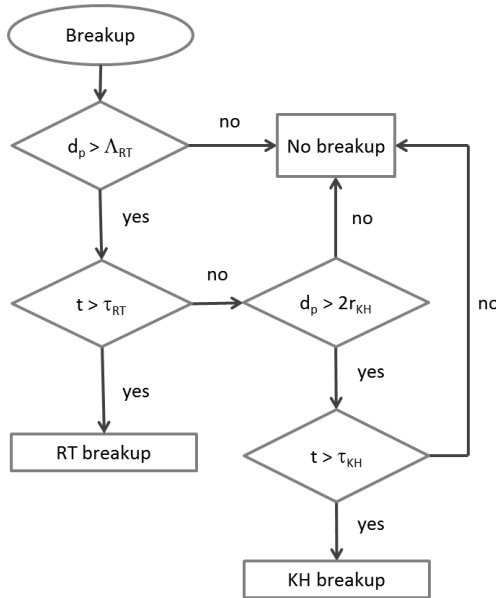


Figure 5 – Combined KH-RT breakup model solution flow diagram.

In the second implementation the RT breakup model is only activated beyond a certain distance from the nozzle, defined as the breakup length,

$$L_b = C_b \sqrt{\frac{\rho_l}{\rho_g}} d_0, \quad (2.50)$$

where  $C_b$  is a model constant ranging from 1 – 50 and  $d_0$  is the nozzle diameter.



So up to the breakup length only the KH breakup is activated (Fig. 6). Beyond that point both KH and RT are activated in a competing manner as described for the first implementation type.

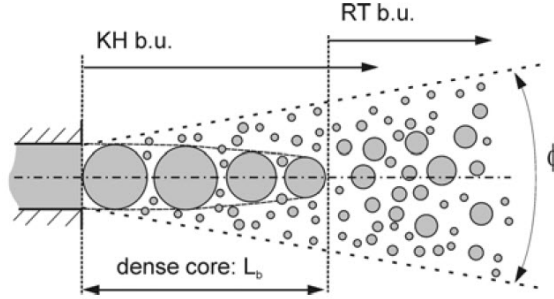


Figure 6 – Combined KH-RT breakup models. Source: Baumgarten (2006).

### 2.3.2 Droplet Drag Model

As a droplet moves, through a gas, with large Weber number it distorts. As the drag coefficient is dependent on the droplet shape, the aerodynamic drag forces vary considerably. A classical method to calculate the drop distortion is the Taylor-Analogy Breakup (TAB) model (LIU; MATHER; REITZ, 1993).

If the droplets are assumed as spherical drops, the aerodynamic drag forces are under-predicted. The spheres' drag coefficient ( $C_{D,sphere}$ ), is given by

$$C_{D,sphere} = \begin{cases} 0.424 & \text{if } Re > 1000 \\ \frac{24}{Re} \left( 1 + \frac{1}{6} Re^{\frac{2}{3}} \right) & \text{if } Re \leq 1000 \end{cases} \quad (2.51)$$

The dynamic drag model is then used to take in consideration the changes due to droplet distortions, and calculates the new drag coefficient,

$$C_D = C_{D,sphere}(1 + 2.632y) \quad (2.52)$$

where  $y$  represents the displacement of the droplet's surface from its equilibrium position.

The Taylor-Analogy Breakup (TAB) (O'ROURKE; AMSDEN, 1987)

is based on a spring-mass system and an oscillating droplet (Fig. 7).

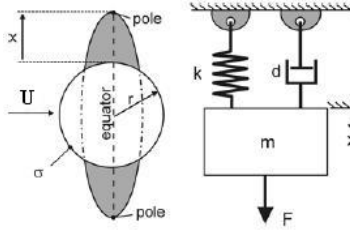


Figure 7 – Taylor-Analogy Breakup. Source: Baumgarten (2006).

The equation of motion with the coefficients as per the analogy is given by

$$\ddot{x} = C_F \frac{\rho_g |U_i|^2}{\rho_l r_0} - C_k \frac{\sigma}{\rho_l r_0^3} x - C_d \frac{\mu_l}{\rho_l r_0^2} \dot{x} \quad (2.53)$$

In this equation  $C_F = 1/3$ ,  $C_k = 8$  and  $C_d = 5$  are model constants deduced in O'Rourke and Amsden (1987) and  $r_0$  is the undisturbed droplet radius. Marek (2013) has derived the model and has identified a typo in the original model, where the constant  $C_d$  value is 10, instead of 5.

Using a dimensionless displacement ( $y = \frac{x}{C_b r_0}$ ), that represents the displacement of the droplet's surface from its equilibrium position, divided by the droplets radius ( $C_b = 1/2$  is a model constant), and solving results in

$$y(t) = We_c + e^{-\frac{t}{t_d}} \left[ (y - We_c) \cos(\omega t) + \frac{1}{\omega} \left( \dot{y}_0 + \frac{y_0 - We_c}{t_d} \right) \sin(\omega t) \right], \quad (2.54)$$

in this equation  $\omega$  is the droplet oscillation frequency and  $t_d$  is the viscous damping time.

The other expressions in Eq. 2.54, are given by

$$We_c = \frac{C_F}{C_k C_b} We_g \quad (2.55)$$

$$\frac{1}{t_d} = \frac{C_d}{2} \frac{\mu_l}{\rho_l r_0^2} \quad (2.56)$$

$$\omega^2 = C_k \frac{\sigma}{\rho_l r_0^3} - \frac{1}{t_d^2} \quad (2.57)$$

Lee et al. (2012) have shown that in the original TAB model from O'Rourke and Amsden (1987) there is a swap between the sine and cosine coefficients in the  $\dot{y}$  expression.

In OpenFOAM the coefficients are named differently for easy identification as,

$$\begin{aligned} C_d &= C_{mu} \\ C_k &= C_{omega} \\ \frac{C_k C_b}{C_F} &= We_{crit} = 12 \end{aligned} \quad (2.58)$$

### 2.3.3 Spray Turbulence Interactions

In both RANS and LES approaches, the standard turbulent dispersion of spray droplets are incorporated through a stochastic calculation of the fluctuations of drag force on droplets. The velocity fluctuations in each coordinate direction, that are used to calculate the turbulent dispersion, are obtained assuming a Gaussian probability function, as will be described below (Eq. 2.61). In the context of LES approach, this model accounts for the dispersion caused only by the **subgrid** turbulent scales, once the dispersion caused by the large eddies is captured by the drag force calculated considering the calculated velocity fluctuations corresponding to the "large" structures.

#### 2.3.3.1 Standard Models for Spray-Turbulence Interactions

When considering the statistical treatment of the interactions between the spray droplets and the turbulent flow field, these interactions are accounted by two terms; a spray induced turbulence (*SIT*),

$$\dot{W}_s = \frac{1}{V_{cell}} \sum \left( m_p \frac{dv_i}{dt} \right) u'_i, \quad (2.59)$$

which is included as a source term in turbulent kinetic energy transport equation and accounts for the production or dissipation of turbulent kinetic energy in the one equation eddy viscosity model (Eq. 2.17) for LES and on Eq. 2.30 for RANS and, a stochastic turbulent dispersion (*STD*), that accounts for the parcel dispersion due to interaction with the fluctuating flow field,

$$U_i = u_i + u'_i - v_i. \quad (2.60)$$

In the equations above  $V_{cell}$  is the computational cell volume,  $m_p$  is the parcel mass.

The gas velocity fluctuation components ( $u'_i$ ), is not known and thus are calculated assuming that a Gaussian probability density function represents their behavior (AMSDEN; OROURKE; BUTLER, 1989; BAUMGARTEN, 2006), given by

$$G(u'_i) = \frac{1}{\sqrt{2\pi}\sqrt{2k/\varepsilon}} \exp\left(-\frac{|u'_i|^2}{4k/3}\right). \quad (2.61)$$

In this equation the subgrid turbulent kinetic energy ( $k_{sgs}$ ) is considered for the LES model.

In the current CFD code implementation this is done by generating random numbers ( $RndNumb$ ) between 0 and 1 for each one of the components and obtaining the velocity fluctuation as,

$$u'_i = 2\sqrt{\frac{2k}{3}} RndNumb_i. \quad (2.62)$$

The velocity fluctuation corrects the drop-gas relative velocity ( $U_i$ ), Eq. 2.60, if the local turbulent time ( $t_{turbLoc}$ ) defined as,

$$t_{turbLoc} = \min\left(\frac{k}{\varepsilon}, C_{ps} \frac{k^{3/2}}{\varepsilon} \frac{1}{|U_i|}\right), \quad (2.63)$$

is larger than the actual time-step ( $dt$ ).  $C_{ps}$  is an empirical constant equal to 0.16432 (AMSDEN; OROURKE; BUTLER, 1989). The inclusion of a fluctuating velocity in the relative velocity calculation, will incorporate in the drag force calculation the effect of the subgrid turbulent fluctuations. However, as will be seen and discussed in the results section, when the grid is refined to a point such that the Stokes number referred to the subgrid eddies is according to the proposed metric (Eq. 3.6), it is expected that the subgrid turbulence does not affect the droplets' trajectories.

The models described for *SIT* and *STD* are used with both RANS and LES based turbulence models. In the case of RANS the turbulent dissipation ratio ( $\varepsilon$ ) is obtained from its transport equation, while in LES the dissipation term from the one equation eddy viscosity model (Eq. 2.17), is calculated considering the subgrid turbulent kinetic energy ( $\varepsilon = C_\varepsilon \frac{k_{sgs}^{3/2}}{\Delta}$ ). In that equation  $C_\varepsilon$  is a constant, which different authors attribute different values, as an example, (BHARADWAJ; RUTLAND; CHANG, 2009) uses  $C_\varepsilon = 0.30$ , (KE; LIXING; CHAN, 2014) uses  $C_\varepsilon = 0.0916$ , (BANERJEE; RUTLAND, 2015) uses  $C_\varepsilon = 1.0$ .

In order to evaluate the effect of the number of Lagrangian parcels and Eulerian mesh size on the statistical representation of droplet stochastic turbulent dispersion, a turbulent dispersion (*STD*) LES sub-model has been implemented while, based on the conclusions from Jangi et al. (2015) that will be discussed in section 3.1, *SIT* has not been included in the modeling.

### 2.3.4 Evaporation

Real fuels are mixtures of various different components with different evaporation behaviors. More volatile components evaporate first and those with higher molecular weight evaporate latter. In virtue of this there are different possibilities of mathematically describing such behavior. The single component model, as the name states, is adequate for single component fuels and even though it is possible to represent, in some cases, the mean properties of the multi component fuel with a single component fuel, there are significant differences concerning the overall mixture formation process. Multi-component fuel evaporation models exist, however, as this work will be based on single component fuel sprays only, they will not be discussed.

#### 2.3.4.1 Single component droplet evaporation

In this model (KRALJ, 1996), the time rate of change of droplet mass that will determine the amount of fuel vapor to be added to the computational cells, is given by

$$\frac{dm_d}{dt} = -\pi d \rho_g D S h_d \ln(1 + B_d), \quad (2.64)$$

which is implemented as,

$$\frac{dm_d}{dt} = -\frac{m_d}{\tau_e}, \quad (2.65)$$

where  $\tau_e$  is the evaporation relaxation time defined as,

$$\tau_e = \frac{m_d}{\pi d \rho_g D S h_d \ln(1 + B_d)}. \quad (2.66)$$

This leads to the Frossling correlation in terms of diameter, implemented as,

$$\frac{dd}{dt} = -\frac{d}{3\tau_e}, \quad (2.67)$$

in order to model the time rate of change of droplet diameter.

In the equations above  $m_d$  is the droplet mass,  $D$  is the mass diffusivity of liquid vapor in air,  $d$  is the droplet diameter,  $B_d$  is the Spalding transfer number given by,

$$B_d = \frac{Y_1^* - Y_1}{1 - Y_1^*}; \quad (2.68)$$

and  $Sh_d$  is the Sherwood number given by,

$$Sh_d = (2.0 + 0.6Re_d^{\frac{1}{2}} Sc_d^{\frac{1}{3}}) \frac{1}{B_d}. \quad (2.69)$$

In Eq. 2.68  $Y_1^*$  is the fuel vapor mass fraction at the droplet's surface given by,

$$Y_1^* = \frac{M_1}{M_1 + M_{mix} \left( \frac{p_{gas}}{p_v} - 1 \right)}, \quad (2.70)$$

and the fuel vapor mass fraction  $Y_1 = \frac{\rho_1}{\rho}$ .

In Eq. 2.70  $M_1$  is the molecular weight of the fuel,  $M_{mix}$  is the molecular weight of all species excluding fuel vapor,  $p_{gas}$  is the gas pressure and  $p_v$  is the vapor pressure at the current droplet temperature.

In Eq. 2.69  $Sc_d$  is the Schmidt number of air given by,

$$Sc_d = \frac{\mu_{air}}{\rho_{gas} D}, \quad (2.71)$$

and  $Re_d$  is given by,

$$Re_d = \frac{\rho_{gas} |u_i + u'_i - v_i| d}{\mu_{air}}. \quad (2.72)$$

In Eq. 2.72  $\mu_{air}$  is evaluated at  $\hat{T} = \frac{T_{gas} + 2T_d}{3}$ , where  $T_{gas}$  is the gas temperature and  $T_d$  is the droplet temperature. In Eq. 2.71 the vapor mass phase diffusivity  $D$  is obtained from a polynomial correlation from the American Petroleum Institute (API) given by,

$$D = 3.6059e^{-3} (1.8 * T)^{1.75} \frac{\alpha}{p * \beta}, \quad (2.73)$$

where  $\alpha = \sqrt{1/w_f + 1/w_a}$  and  $\beta = \sqrt{a^{(1/3)} + b^{(1/3)}}$ , with  $a = 147.18$ ,  $b = 20.1$ ,  $w_f = 170.338$  and  $w_a = 28.0$  are the constants for n-Dodecane.

In order to obtain the change in droplet temperature an energy balance

in the drop has to be performed (KRALJ, 1996; BAUMGARTEN, 2006),

$$\dot{Q}_d = c_{p,l} \dot{m}_d \frac{dT_d}{dt} - \frac{dm_d}{dt} H_{vap}, \quad (2.74)$$

where,

$$\dot{Q}_d = \pi d K_{air} Nu_d f (T_{gas} - T_d), \quad (2.75)$$

where  $f$  is a factor that corrects the rate of heat exchange due to mass transfer,

$$f = \frac{z}{e^z - 1} \quad (2.76)$$

$$z = -\frac{c_{p,v} \dot{m}_d}{\pi d K_{air} Nu_d}. \quad (2.77)$$

In the equations above  $\dot{Q}_d$  is the rate of heat transfer to the drop,  $c_{p,l}$  is the specific heat capacity of the liquid fuel,  $H_{vap}$  is the latent heat of vaporization at the drop temperature,  $c_{p,v}$  is the specific heat capacity of the vapor fuel,  $K_{air}$  is the conductivity of the air evaluated at  $\hat{T}$ ,  $Nu_d$  is the Nusselt number given by the Ranz-Marshall correlation,

$$Nu_d = 2.0 + 0.6 Re_d^{\frac{1}{2}} Pr_d^{\frac{1}{3}}, \quad (2.78)$$

where  $Pr_d$  is the Prandtl number given by,

$$Pr_d = \frac{\mu_{air} c_p}{K_{air}}. \quad (2.79)$$

The first term from Eq. 2.74 on the right hand side accounts for droplet heating and the second term accounts for the droplet evaporation.

The time rate of change of droplet temperature is implemented as,

$$\frac{dT_d}{dt} = \frac{f}{\tau_h} (T_{gas} - T_d) - \frac{1}{c_{p,l}} \frac{H_{vap}}{\tau_e} \quad (2.80)$$

where  $\tau_h$  is the heat transfer relaxation time defined as,

$$\tau_h = \frac{m_d c_{p,l}}{\pi d K_{air} Nu_d} \quad (2.81)$$





### 3 THESIS PROPOSAL

As discussed in previous chapters, the current state of the art of CFD modeling for internal combustion engines imply the use of LES approach for the turbulence characterization on the mixture formation and combustion processes. In this chapter a critical review of the state of the art of LES applied to fuel spray modeling will be presented, followed by the reasoning for the modeling selection for this work and finally the details for the thesis proposal.

#### 3.1 CURRENT MODELING LIMITATIONS

From a fuel spray simulation stand point, two major facts impact the liquid length penetration prediction accuracy (NORDIN, 2001; BAUMGARTEN, 2006); (1) the gas phase velocity calculation at the parcel location, which can be done assuming the velocity of the closest node in the volume or interpolate from the other nodes (Fig. 8),

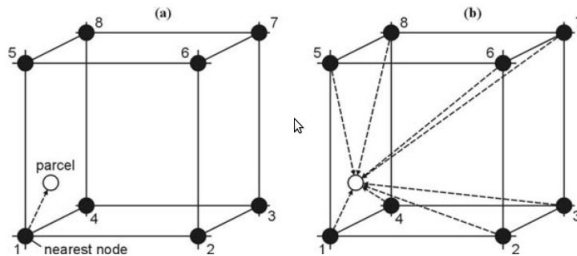


Figure 8 – Gas-droplet velocity calculation: (a) nearest vertex, (b) interpolation. Source: (BAUMGARTEN, 2006)

and (2) the momentum transfer between liquid droplets and gas phase (Fig. 9). On a coarse grid the momentum transfer, from the parcel to the cell gas volume, will be diffused in a bigger volume and the gas acceleration will be smaller, maintaining a high relative velocity between parcel and gas and thus maintaining a high drag that will lead to reduced liquid length penetration. On the other hand, on a finer grid with the momentum transfer the gas velocity will increase faster, reducing the relative velocity between droplets and gas, leading to lower drag and as a consequence higher liquid length penetration. This fact leads to a numerical inconsistency, as it states that with finer grids the solution will deviate from the real physical phenomena.

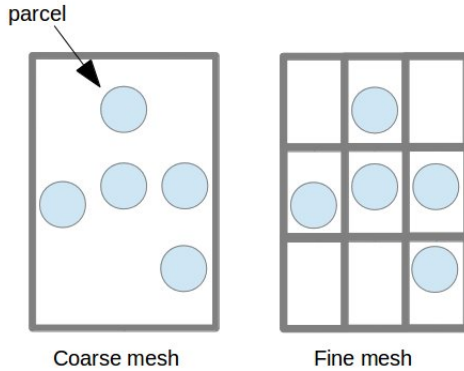


Figure 9 – Liquid-gas phase momentum exchange.

Regarding the droplet size distribution, most spray simulation studies used the Kelvin-Helmholtz/Rayleigh-Taylor (KH-RT) combined breakup models (BHARADWAJ; RUTLAND, 2010; WEHRFRITZ et al., 2013; ELMTOFT et al., 2015), but the model parameters varied among them and, in some cases, using these tuning parameters to improve the correlation of simulation to experimental results.

Another aspect observed in previous works is the lack of consistency to compare liquid length penetration (distance from the nozzle exit along the spray axis to the point where a predefined percentage of liquid fuel is still encountered) against experiments, sometimes even against the same experiment. The percentage definition varied from 90 to 99% among the various cited works. The definition by the Engine Combustion Network (ECN), which shall be used as reference, is 99% to compare simulation results against their experimental data. Therefore, even claiming that experimental value of liquid penetration are adequately reproduced by models, the penetration definition certainly influences this validation. Figure 10 shows the liquid penetration obtained in this work with a coarse mesh (the same simulation), considering two different definitions for the liquid penetration. It can be observed that, changing this definition could lead to a wrong conclusion regarding the results comparison with experiments.

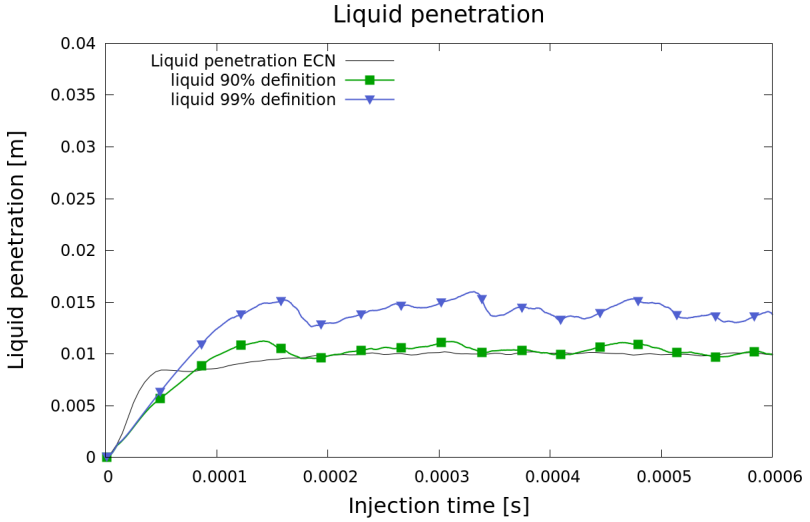


Figure 10 – Influence of liquid penetration definition on results comparison with experiment from ECN.

An investigation on the interaction between mesh size and number of injected parcels was done by Senecal et al. (2013), where the authors stated that with fine grids, if the liquid mass contained in the parcel was similar to the gas phase in the cell, a minimum of momentum transfer was required to get the gas phase to reach the same velocity of the parcel, thus the drag would be reduced to a minimum and as a consequence the liquid length penetration would be over predicted. They concluded that as the mesh was refined the number of injected parcels had to be increased, in order to have the amount of liquid mass in each parcel reduced, and thus minimizing this effect. These authors also considered that the injection of the spray in a single point would have the same effect of reduction in drag, so they proposed the injection to be performed along a circle with the same diameter of the injector nozzle. They also concluded that, for spray modeling with LES approach, the mesh independence condition should be replaced by what these authors called "mesh convergence", i.e., if the mesh would be refined beyond a certain size results would get worse. This statement is inconsistent from a numerical point of view as finer grids must lead to a more precise result and, as will be shown later in this work, if a consistent mesh refinement criteria is followed, the results do improve with mesh refinement. Regarding the liquid length penetration definition they used the value of 95% and the minimum cell size

of  $31.25\mu\text{m}$  with adaptive mesh refinement. They also used dynamic droplet distortion model, droplet collision model and stochastic turbulence dispersion model.

Fig. 11, shows the results for liquid and vapor length penetrations presented by Senecal et al. (2013), varying minimum cell sizes.

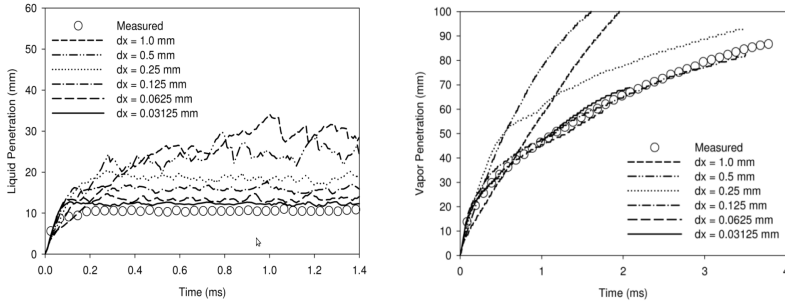


Figure 11 – Liquid and vapor penetration plots from Senecal et al. (2013).

Spray simulation using LES modeling was also investigated by Xue et al. (2013) (Fig. 12). They showed good agreement with experimental results but considered the value of 90% for the definition of liquid length penetration, which as already shown in Fig. 10 would lead to an incorrect conclusion regarding accuracy of the model prediction. The minimum cell size used in their work was  $31.25\mu\text{m}$  with adaptive mesh refinement and included dynamic droplet distortion (TAB), droplet collision and stochastic turbulence dispersion models.

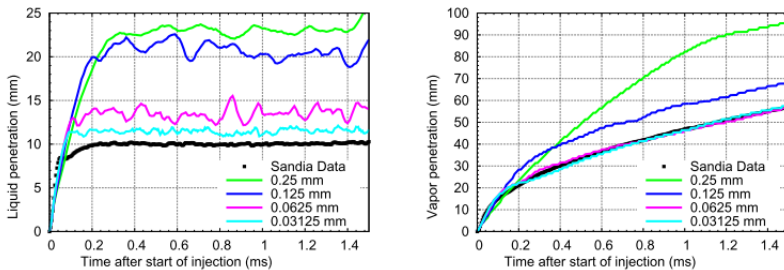


Figure 12 – Liquid and vapor penetration plots from Xue et al. (2013).

Wehrfritz et al. (2013) have used a different approach from all previous works, where they assume that the fuel can be considered as if in supercriti-

cal condition, and that the vapor phase is in fact a large group of very small diameter parcels. The authors have not indicated the fuel temperature from the experiment used, but they have described all the other details about it that have allowed to find it in the SANDIA database. The SANDIA experimental case had the fuel injected at a temperature of 373K, however the critical temperature for n-Dodecane is 658K. This assumption by itself is then not at all valid. Based on the "supercritical" hypothesis they have assumed that the injected droplets are represented by a Rosin-Rammler droplet size distribution, but arbitrarily assuming that the smaller droplet diameter is equal to  $D_{min} = D_{injector}/D_{injector} = 1\mu m$  and the bigger droplet diameter is equal to  $D_{max} = D_{injector}/5 = 18\mu m$ . By assuming this distribution, the solution was somewhat forced to the result that the authors were chasing, while the breakup physical phenomena was completely disregarded. They have shown good agreement with minimum cell sizes of  $41.67\mu m$  using fixed mesh refinement, but considering as 97% the definition for liquid length penetration. The vapor length penetration was under-predicted at the minimum cell size (Fig. 13). This indicates that even forcing the solution by imposing the droplet size distribution and assessing the liquid length penetration to a lower definition, the results are not as accurate as stated by the authors.

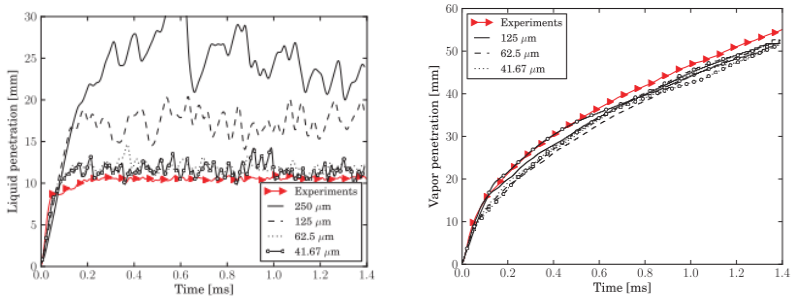


Figure 13 – Liquid and vapor penetration plots from Wehrfritz et al. (2013).

A similar approach presented by Wehrfritz et al. (2013) was attempted by Elmtoft et al. (2015), trying to improve the precision of the spray simulations by reducing the size of the droplets injected by the Blob method, maintaining the point injection. Instead of injecting Blobs with the same size of the nozzle diameter, the initial Blobs' size range from a fraction of 0.10 to 0.25 of the nozzle diameter. They also used 97% for the definition for liquid length penetration. The minimum cell size used in their work was  $62.5\mu m$  with adaptive mesh refinement and also included dynamic droplet distortion,

droplet collision and stochastic turbulence dispersion models.

Other studies were performed by Banerjee and Rutland (2015), in this case with constant mesh size along the simulations (i.e. not used AMR), with minimum cell sizes at the spray region of  $125\mu\text{m}$ . They reported good agreement of liquid penetration with experimental data but only after a certain time after injection (red circle region in Fig. 14), in the region which they defined as steady state liquid jet. Their model was not able of capturing adequately the initial part of penetration. In addition, the definition for liquid length penetration considered was 97%. They also reported results for vapor penetration, and even using 0.05 (5%) fraction as definition, different from 0.1% recommended by the ECN, did not show good agreements.

Fig. 14 shows the results for liquid and vapor length penetrations presented by Banerjee and Rutland (2015), varying minimum cell sizes. In this plot grid-A size is 4mm, grid-B size is 2mm, grid-C size is 1mm and grid-D size is 0.5mm. In their work, the quantity of injected parcels is not identified.

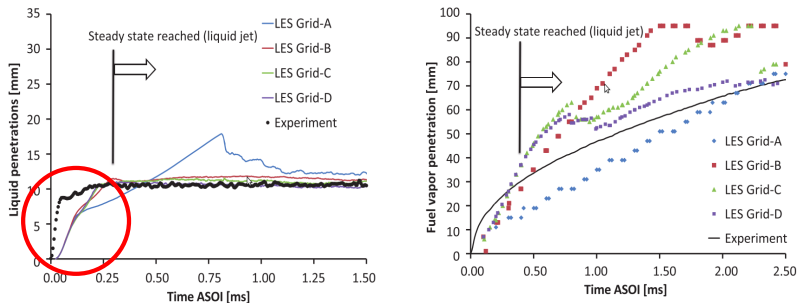


Figure 14 – Liquid and vapor penetration plots from Banerjee and Rutland (2015).

A more detailed analysis on the impact of both *SIT* and *STD*, comparing with experimental data from the ECN, was presented in the work from Jangi et al. (2015). In that work it has been identified that vapor penetration is not affected by either *SIT* or *STD*, while liquid penetration length is over-predicted if *STD* is not modeled. They have also found that the liquid length penetration is not impacted by *SIT*. The authors also stated that the reason for previous works with LES and higher levels of cell refinements to over-predict liquid length penetration was the lack of *STD* modeling. In that work the minimum cell size was  $125\mu\text{m}$ . They have used 95% for liquid length penetration definition and have not stated the definition used for vapor length penetration. They have used Huh-Gosman for primary breakup and KHRT for secondary breakup modeling.

Fig. 15 shows the results for liquid and vapor length penetrations presented by Jangi et al. (2015), varying minimum cell sizes.

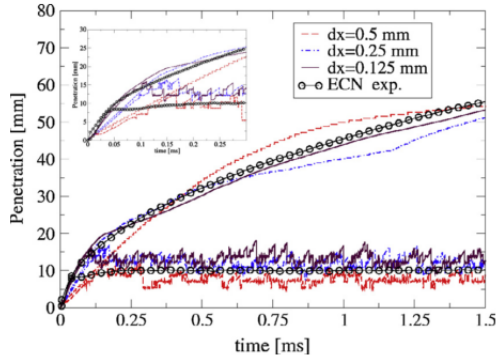


Figure 15 – Liquid and vapor penetration plots from Jangi et al. (2015).

The research described above have used both *SIT* and *STD* in their modeling. This is also the case for various other works not described above such as Lee, Pomraning and Rutland (2002), Bharadwaj and Rutland (2010), Tsang, Trujillo and Rutland (2014), Gong et al. (2014), Gong, Jangi and Bai (2014), Zhou et al. (2015).

Irannejad and Jaber (2014) and Keller et al. (2015) on the other hand, have shown that if the flow structure is correctly captured in the LES modeling, *STD* will not impact the droplet turbulent dispersion, while using cell sizes around 400 and 500  $\mu\text{m}$ , but as will be shown in the results chapter, this mesh size is too coarse to correctly capture the spray-turbulence interaction. Irannejad and Jaber (2014) used 97% as definition for liquid length penetration, while in Keller et al. (2015) this was not informed. Keller et al. (2015) used a Rosim-Ramler distribution as the primary breakup, injecting the parcels along a circle, while Irannejad and Jaber (2014) used a stochastic breakup model presented in Gorokhovski and Saveliev (2003). Both work included droplet distortion model and Irannejad and Jaber (2014) also used collision model.

### 3.2 LES BASED MODELING

From the spray models' review presented in the previous section, it can be concluded that, although computationally costlier than Reynolds Aver-

aged Navier-Stokes (RANS), LES based simulations of in-cylinder processes represent the current state of the art in terms of turbulence models, even in industrial applications. This shows benefits on the modeling of spray turbulence interaction which will influence on the prediction of in-cylinder spatial and temporal distributions of vapor species, temperature and pressure, improving the spray and combustion simulation.

As for spray breakup model set-up, in this work the combined Kelvin-Helmholtz (KH) model described in Reitz (1987) with the Rayleigh-Taylor breakup model, as presented in Patterson and Reitz (1998) are used, with both models competing during the injection duration. The parcels are injected in a single point location with initial diameters equal to the nozzle hole diameter.

For all the cases the KH-RT breakup model constants used in this work have been kept the same (Tab. 1), eliminating additional tuning as a consequence of the varying parameters (Tab. 3).

Table 1 – KH-RT model constants

|            |      |
|------------|------|
| B0         | 0.61 |
| B1         | 2    |
| $C_{\tau}$ | 1    |

The usage of the dynamic droplet drag model, with the droplet distortion obtained with the TAB model from Liu, Mather and Reitz (1993), is a common method required to avoid under-prediction of the aerodynamic drag on the droplet. However, its impact is also investigated in more detail in this work.

For the spray vessel simulation a single component fuel is being injected so the single component droplet evaporation model described in section 2.3.4.1 is used.

Turbulent dispersion has a significant impact on important spray parameters as liquid and vapor penetration. However, concerning the stochastic turbulent dispersion modeling, as can be seen in results hereby obtained, even considering STD models, the results are far from the experimental ones. Therefore, two aspects have been analyzed: (i) the effect of mesh refinement, considering STD model and (ii) the effect of mesh refinement on the need of using STD model, i.e., to what extent the subgrid structures are capable of dispersing the smaller droplets. For these analysis a mesh refinement criterion is proposed and discussed below, based on local droplet Stokes number.



### 3.3 SPRAY TURBULENCE INTERACTION - PROPOSED GRID REFINEMENT APPROACH BASED ON DROPLET STOKES NUMBER

In LES approach, as the mesh is refined and smaller turbulent scales are captured (i.e., less turbulent scales are captured through subgrid models), the turbulent dispersion of smaller droplets will be captured by the droplets' drag by the velocity fluctuations of the continuous phase. Therefore, no statistical treatment would be necessary if the mesh is sufficiently refined. This is true for LES modeling of single phase flow, as the mesh is refined beyond Kolmogorov scales, resulting in Direct Numerical Simulation. This is impracticable for industrial applications. **However, regarding the spray turbulent dispersion, the mesh size required would be that which captures the smallest eddies that are capable of dispersing the smallest droplets present in a given region of the domain. These eddies are expected to be much larger than Kolmogorov scales, for high droplet/gas density ratios.** From another point of view, we can find out to what extent the subgrid eddies are capable of dispersing (changing trajectories) of the smallest droplets present in a given region. Therefore, the local droplet Stokes number, based on the subgrid turbulent eddies time-scale arises as a good criterion for adaptive mesh refinement, to adequately model the spray-turbulence interactions. This concept is discussed in more details, for gas-solid flows, in Boivin, Simonin and Squires (2000), but the focus in that work was the effect of particles on subgrid turbulence, i.e. the SIT effect previously discussed. Even though, as very small droplets can be present in the model, as result of break-up models, the consideration that all turbulent dispersion is captured by resolved scales, would lead to extremely fine grids. Therefore, this criterion will remain as qualitative in the simulations in this work and subgrid STD model may still be required. However, as will be seen in the results section, this criterion is useful for adaptive mesh refinement when the "usual" criterion, i.e., refinement based on vapor front, is not adequate. For instance, in cases of low temperature when spray penetration leads the vapor front. Furthermore, independently of the mesh refinement criterion used, it will be shown that the analysis of the resulting fields of Stokes number distribution is useful to evaluate the results' quality and to what extent the subgrid turbulence affects the spray.

Following the work from Crowe, Chung and Troutt (1988), as shown in Fig. 16, for  $St \gg 1$  it can be assumed that eddies (in this case, subgrid ones) will not affect droplets motion. The Stokes number in this work is related to the filter size scale.

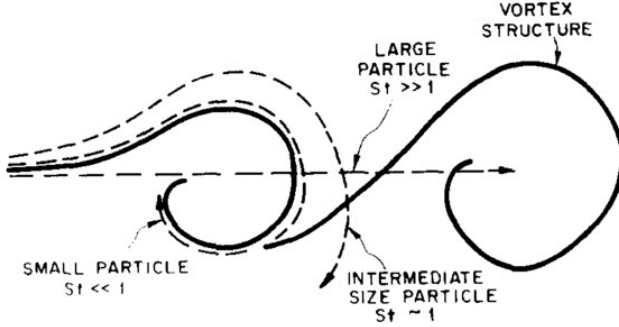


Figure 16 – Possible droplet trajectories in a turbulent flow field. Source: (CROWE; CHUNG; TROUTT, 1988).

To compute the effect of the subgrid eddies on droplets' trajectories, the droplet Stokes number should be based on the characteristic turn over time of the subgrid eddies,

$$St_{sgs} = \frac{\tau_d}{t_e} = \frac{\tau_d u'_{sgs}}{l_{sgs}}. \quad (3.1)$$

The integral length scale of subgrid given by Boivin, Simonin and Squires (2000),

$$l_{sgs} = C_K \frac{k_{sgs}^{3/2}}{\varepsilon}, \quad (3.2)$$

where, from equation (2.17),  $\varepsilon = C_\varepsilon k_{sgs}^{3/2} / \Delta$  and  $C_K$  is a constant of order of unity (BOIVIN; SIMONIN; SQUIRES, 2000). As stated before, different authors attribute different values to  $C_\varepsilon$  but the (maybe obvious) conclusion is that the integral length scale of the subgrid turbulence is proportional to the mesh size filter,  $\Delta$ . So the subgrid eddy turn-over time can then be calculated as,

$$\begin{aligned}
t_e &= \frac{l_{sgs}}{u'_{sgs}} \\
&= \frac{(C_K/C_\epsilon)\Delta}{u'_{sgs}} \\
&= \frac{C_K}{C_\epsilon\sqrt{2/3}} \frac{\Delta}{\sqrt{k_{sgs}}} \\
&= \text{Constant} \frac{\Delta}{\sqrt{k_{sgs}}}
\end{aligned} \tag{3.3}$$

The relaxation time, or droplet characteristic time,  $\tau_d$  is given by,

$$\tau_d = \frac{2}{9} \frac{\rho_l r_{SMD}^2}{\mu_g} \tag{3.4}$$

As the relaxation time  $\tau_d$  arrives from a balance between drag and inertia, the Sauter Mean Diameter (SMD), which relates volume and droplet interface area, is then used as characteristic weighted average diameter.

Therefore, the droplet Stokes number, based on subgrid eddies characteristic time, results in,

$$\begin{aligned}
St_{sgs} &= \frac{C_\epsilon\sqrt{2/3}}{C_K} \frac{2\rho_l}{9\mu_g} \frac{r_{SMD}^2}{\Delta} k_{sgs}^{1/2} \\
&= C_{St} \frac{\rho_l}{\mu_g} \frac{r_{SMD}^2}{\Delta} k_{sgs}^{1/2}
\end{aligned} \tag{3.5}$$

If the droplet Stokes number, **related to the subgrid eddies** is larger than unity, it is expected that the droplets are not affected by the subgrid turbulence. This criterion is proposed to assure that the interaction between droplets and the gas phase is resolved, and coupled via the drag force, considering the resolved scales. Thus no turbulent dispersion modeling would be required for the subgrid. The value of the constant ( $C_{St}$ ) in Eq. (3.5) can be, *a priori*, calculated from standard values proposed in literature for  $C_K$  and  $C_\epsilon$ . However, it must be considered that, integral scales,  $l_{sgs}$  and  $u'_{sgs}$  (respectively related to the mesh filter size  $\Delta$  and to the subgrid TKE,  $k_{sgs}$ ) comprise all lengths and time scales ranging from the mesh filter to the Kolmogorov scales. In addition, the SMD also represents an average of the droplet diameter. Therefore, the resulting values of the Stokes number, calculated based on these parameters, could not be an exact representation of the "dispersion

capacity” of subgrid turbulence and, therefore, the value of  $C_{St}$  was adjusted to adequate the mesh refinement criterion. Furthermore, to properly resolve the turbulent scales that are capable of transporting the droplets, high cell refinements are required in the domain, which can lead to extremely large cell counts, rendering the procedure unfeasible for industrial applications. Therefore, even using this criterion, STD models should be included in simulations, when very small droplets are present in the spray. Considering the values proposed in literature  $C_K$  and  $C_\epsilon$  of order of unity (recalling that  $C_\epsilon = 1$  is also encountered) results in  $C_{St} \approx 0.2$ . In this work the value of  $C_{St} = 0.6$  was used, which gave adequate results. However, as stated, this analysis should remain as qualitative. Considering this value, the proposed droplet Stokes number based on the subgrid energy criterion to allow mesh refinement was set to,

$$St_{sgs} \geq 1 \quad (3.6)$$

which is aligned with the general concept definition proposed by Crowe, Chung and Troutt (1988).

### 3.4 NUMERICAL IMPLEMENTATIONS

OpenFOAM (Open Source Field Operation and Manipulation) is a C++ developed library, where it is possible to develop specific solvers to deal with modeling of physical and chemical phenomena based on Finite Volume Method. The tool is designed in such a way that the user can create its own solver by reusing basic classes already scripted in C++. The numerical model developed in this thesis was performed through code implementations on the base OpenFOAM 2.0.x version.

In this work a LES turbulence model was implemented in a Lagrangian spray based solver in OpenFOAM to analyze turbulent, non-reacting spray flow, with adaptive mesh refinement.

In the OpenFOAM release used in these simulations, there is an isotropic cell splitting implemented to allow for adaptive mesh refinement (KARLSSON, 2013). In this implementation it is possible to define a refinement criterion, that will mark the cells, and then split them in every direction by a factor of 2, so one cell is split in 8 new cells and the coarse mesh field is interpolated to the refined cells. In this work in order to improve the computational accuracy without excessive impact on memory and time costs, adaptive mesh refinement (*AMR*) is used in all cases testing 4 different refinement levels (2, 3, 4 and 5). The simulations have been performed with a base cell size of  $1\text{mm}$ , and at every refinement level the mesh size is split in half in its 3 dimensions. So the cases with 2 levels of *AMR* led to a minimum cell size of

$250\mu m$ , cases with 3 levels of *AMR* led to a minimum cell size of  $125\mu m$ , cases with 4 levels of *AMR* led to a minimum cell size of  $62.5\mu m$  and cases with 5 levels of *AMR* led to a minimum cell size of  $31.25\mu m$ . The mesh refinement criterion used in this work was based on evaporated fuel fraction ( $Y_{fuel}$ ) or on the droplet Stokes number ( $St_{sgs}$ ) according to the proposed criterion, which implementation will be discussed in the next section. The mesh was not unrefined during the simulation, so where the refinement criterion was met at any point in time during the simulation it remained with that constant cell size to the end of the run.

As described in section 3.1, the interpolation scheme for the gas phase velocity calculation at the parcel location is important to improve accuracy. From the interpolation schemes for the lagrangian phase available in OpenFOAM, two have been investigated, cellPointFace (*CPF*) and pointMVC (*PMVC*). In OpenFOAM the gas velocity is stored at the cell centers. In the *CPF* method the hexahedral cell is divided in tetrahedral elements, being 1 vertex in the cell center, 1 vertex in one of the cell faces' center and 2 face vertices (Fig. 17).

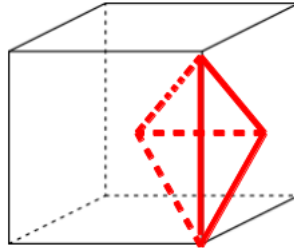


Figure 17 – Graphical representation of hexahedral cell splitting in cell-PointFace method.

The parcel will then be found inside one of the tetrahedral elements, and so the gas velocity will be interpolated to the vertices of that tetrahedral and then interpolated from the vertices to the parcel position. The *CPF* interpolation method is an improvement when compared to the nearest node (Fig. 8-a), but share the same concept of interpolating to the closest nodes. In the *PMVC* method the gas velocity at the cell center will be interpolated directly to its vertices and then use the Mean Value Coordinates interpolation to the parcel position (Fig. 8-b).

A case with 4 levels of cell refinement has been simulated, comparing

both interpolation schemes mentioned above. As can be seen in Fig. 18 the impact on liquid length penetration is minimal. On the other hand, the vapor length penetration increases if PMVC interpolation scheme is used. Based on this comparative analysis, the *CPF* interpolation scheme has been used throughout the analyses that will be presented in the upcoming chapters.

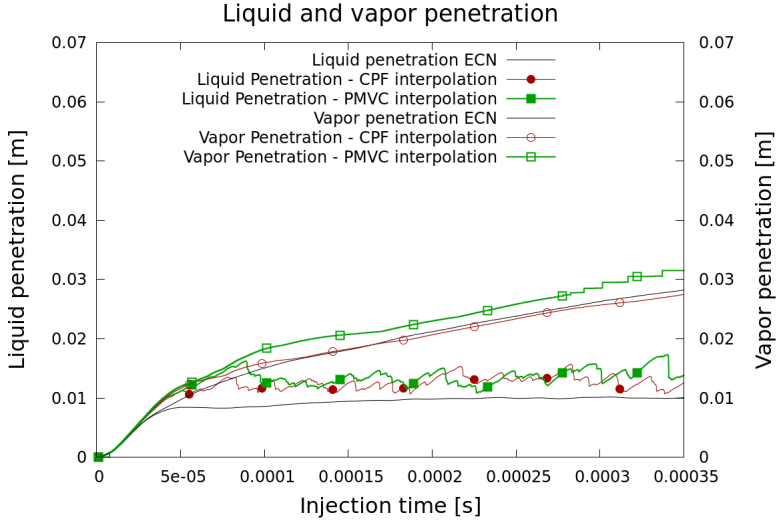


Figure 18 – Interpolation schemes impact on liquid and vapor length penetration .

Concerning the numerical interpolation schemes used, first order discretization is used for the time derivatives and second order discretization scheme for convection and diffusion terms. Due to the high characteristic velocity of the physical process, to maintain the solution stability the CFL number was limited to a maximum of 0.25, thus resulting in a very small time-step of the order of  $10^{-8}s$ , thus second order discretization for the time derivatives was not deemed necessary. The pressure-velocity coupling algorithm used is PIMPLE, described in Holzmann (2016), a transient algorithm that is a merge of PISO and SIMPLE available in the original solver which allows usage with bigger time-steps than the original schemes. Regarding the solution of resulting linear systems, pressure and density are solved with a matrix symmetric solver, Preconditioned Conjugate Gradient (PCG) using a Diagonal Incomplete-Cholesky (DIC) preconditioner, while velocity, enthalpy and turbulent kinetic energy are solved with a Preconditioned Bi-Conjugate Gradient (PBiCG), with a Diagonal Incomplete-LU (DILU) preconditioner.

### 3.4.1 Droplet Stokes number numerical implementation

For the implementation of the droplet Stokes number into OpenFOAM, a routine has been created using the original spray and parcel classes, where it is possible to work with predefined functions to obtain information about the Lagrangian part of the simulation, such as droplet Sauter Mean Diameter. The remaining scalars are obtained in the Eulerian part, such as turbulent kinetic energy at the subgrid and cell size where the Lagrangian parcel is located.

A new refinement scalar field, the droplet Stokes number, is created and the resulting value from Eq. 3.5 is stored at the cell level. This new field could then be selected at run-time to be used as a criterion for the adaptive mesh refinement.

### 3.4.2 Other implementation issues

For the implementation of the stochastic turbulent dispersion for LES, as described in section 2.3.3, a routine has been created using the original spray class to obtain the required parcel information. The turbulent dissipation, is calculated as  $\varepsilon = C_\varepsilon \frac{k_{tgs}^{3/2}}{\Delta}$ , the velocity fluctuation is calculated from Eq. 2.62, the local turbulent time is obtained from Eq. 2.63, and finally the relative velocity is updated per Eq. 2.60.

The Engine Research Group from Politecnico di Milano (PoliMi) has created a library for internal combustion engines (Lib-ICE), by implementing new codes and modifications to the original OpenFOAM 2.0.x release. In a partnership between UFSC and PoliMi, part of this code was provided to be the starting point of this thesis.

In the course of this work the following corrections to the codes in Lib-ICE, released by the Politecnico de Milano, have been required and thus performed:

- Corrections to the KH breakup time, as proposed originally by Reitz (1987).

The KH breakup time equation was implemented as in the work from Nordin (2001),

$$\tau_{KH} = \frac{3.788B_1r_0}{\Lambda\Omega}, \quad (3.7)$$

and was corrected to the original model proposed by Reitz (1987),

$$\tau_{KH} = \frac{3.726B_1r_0}{\Lambda\Omega} \quad (3.8)$$

- Corrections in the implementation of the combined KH-RT breakup models, in order to allow both models to compete during the whole injection duration.

PoliMi, in their ICE library, had attempted to improve the breakup of the droplet by adding a boiling sub-routine in the KH-RT combined model. The boiling implementation is not part of the original KH-RT combined model, and thus has been removed.

- Corrections to the TAB model used for the dynamic droplet distortion. Polimi, in their ICE library, in an attempt to increase the droplet distortion,

$$y(t) = We_c + e^{\frac{-t}{t_d}} \left[ (y - We_c) \cos(\omega t) + \frac{1}{\omega} \left( \dot{y}_0 + \frac{y_0 - We_c}{t_d} \right) \sin(\omega t) \right] \quad (3.9)$$

have modified the original implemented time in OpenFOAM 2.0.x to another droplet characteristic time in the parcel. This led to distortion values that were unrealistically high. To correct this issue, the original implementation in OpenFOAM 2.0.x was restored in the code.



## 4 SPRAY SIMULATION RESULTS

In order to validate non-reacting spray modeling, a set of reliable and well documented experiments are required. These experiments are available and provided by the Sandia National Laboratories at the Engine Combustion Network (ECN), that intends to provide data for collaboration among researchers around the globe. For the development of this thesis, experimental data for non-reacting fuel sprays of  $nC_{12}H_{26}$  (n-Dodecane) available at ECN have been used. A photo and a schematic of the Sandia combustion vessel is shown on Fig.19.

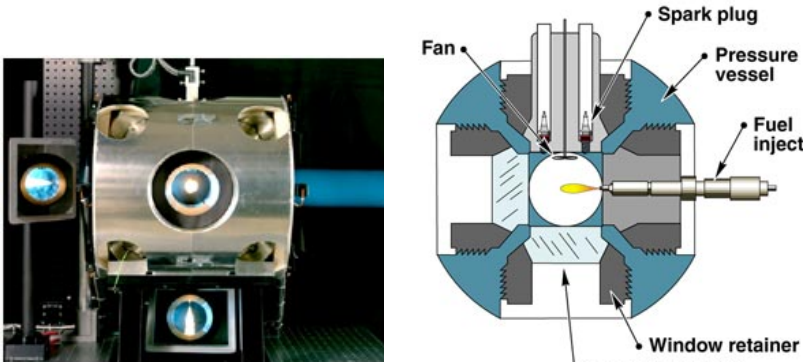


Figure 19 – Photo of the optically accessible high-temperature, high-pressure spray chamber at Sandia (left), schematic of Sandia combustion vessel (right). Source: Sandia National Laboratories.

### 4.1 EXPERIMENTAL CASES FROM SANDIA

The experimental cases documented in the Engine Combustion Network from SANDIA National Laboratories (ECN, ), have been used to validate the simulation models. Further details of geometry and experimental conditions can be found in (<https://ecn.sandia.gov/diesel-spray-combustion/>). Table 2 shows the non-reacting case's details.

Regarding experimental data for injection mass flow rate, its measure included constant oscillations during the main injection period that, as described in ECN, may be real and caused by pressure fluctuations but sensor vibration or ringing at a natural frequency should also be causing them. This

Table 2 – Non Reacting Case Details

|                       | ECN Test 1                    | ECN Test 2      |                 |
|-----------------------|-------------------------------|-----------------|-----------------|
| <b>Vessel details</b> | $O_2$ [%]                     | 0.0             | 0.0             |
|                       | $N_2$ [%]                     | 89.71           | 89.71           |
|                       | $CO_2$ [%]                    | 6.52            | 6.52            |
|                       | $H_2O$ [%]                    | 3.77            | 3.77            |
|                       | Ambient temp [K]              | 900             | 900             |
|                       | Ambient pressure [MPa]        | 6.05            | 2.04            |
|                       | Vessel lateral dimension [mm] | 108             | 108             |
| <b>Spray details</b>  | Injected fuel                 | $nC_{12}H_{26}$ | $nC_{12}H_{26}$ |
|                       | Nozzle diameter [ $\mu m$ ]   | 83.7            | 89.4            |
|                       | Nozzle orifice Cd             | 0.89            | 0.9             |
|                       | Injection $\Delta P$ [MPa]    | 150             | 150             |
|                       | Injection duration [ms]       | 1.54            | 1.54            |
|                       | Injected fuel mass [mg]       | 3.46            | 3.9             |
|                       | Fuel temperature [K]          | 373             | 373             |

oscillations can impact particularly the comparison of the initial penetration, so their recommendation is to use a filtered signal that removes noises and contains a more realistic ramp-up shape. The engine group from Polytechnic University of Valencia provides a simple tool to generate the mass flow rate signal from the ECN experiments (<https://www.cmt.upv.es/ECN03.aspx>).

A comparative example between these signals is shown in Fig. 20 and the injected mass flow rate profile for the experiment used in this work is shown on Fig. 21.

The uncertainty in the liquid length penetration measurement is shown in Fig. 22, while the uncertainty in the vapor length penetration measurement is shown in Fig. 23. Liquid length penetration is obtained from high-speed Mie-scatter imaging using a 3% threshold of maximum intensity as described by Siebers (1998). Shadowgraph or schlieren imaging were used to identify the vapor boundary of a penetrating jet. The boundary of the spray is determined through image analysis. The penetration distance is defined as the distance along the spray axis to the boundary of the spray as described in Naber and Siebers (1996).

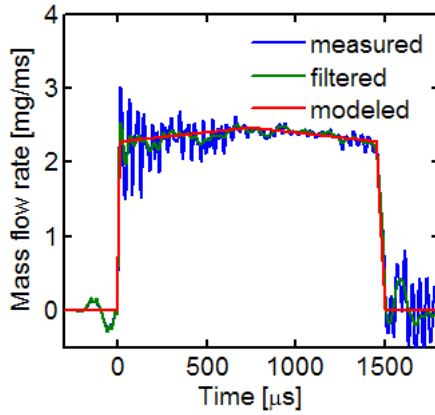


Figure 20 – Comparison between mass flow rate signals. Source: ECN

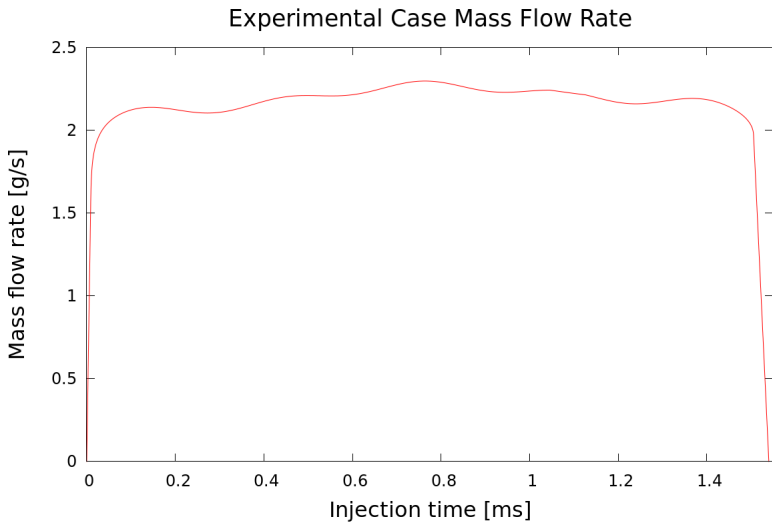


Figure 21 – Non-reacting cases mass flow rate.

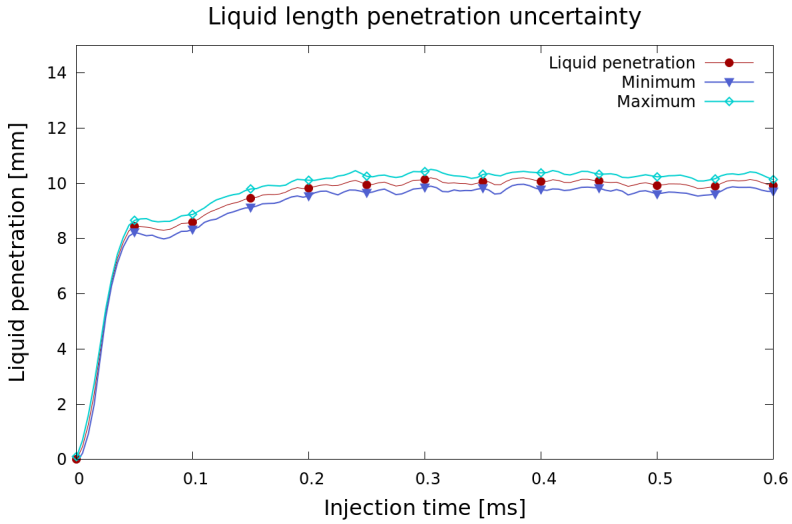


Figure 22 – Liquid length penetration measurement uncertainty.

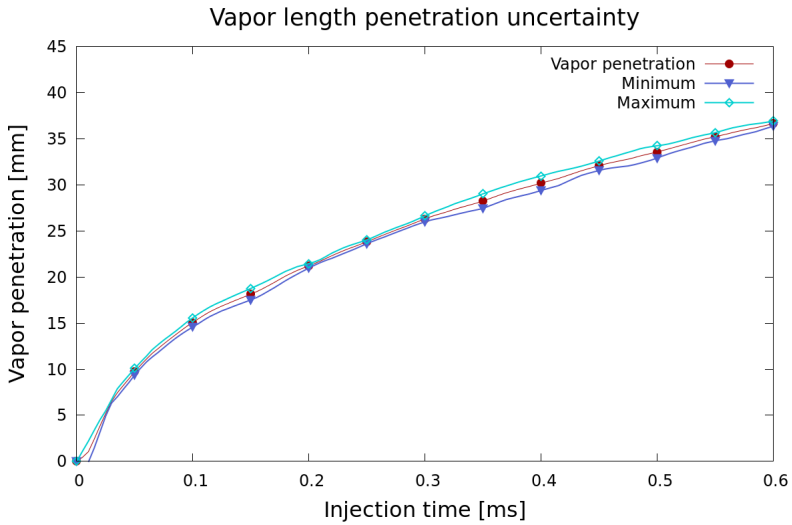


Figure 23 – Vapor length penetration measurement uncertainty.

## 4.2 NON-REACTING SPRAY SIMULATIONS

Fig. 24 shows in the left side the CFD vessel domain, in the center the initial mesh with constant size equal to 1mm and in the right image, the mesh at 0.1ms after start of injection in a case with 4 levels of AMR, so with minimum cell size of  $62.5\mu m$ .

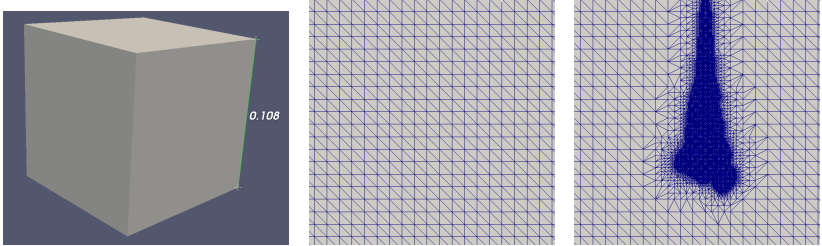


Figure 24 – CFD vessel (left), initial mesh with 1mm cells (center), adaptive mesh refined with 4 levels of AMR (right).

As discussed in previous sections, in addition to the mesh refinement and parcel count, the influence of Stochastic Turbulent Dispersion (STD) model inclusion and droplet distortion on drag (TAB) will also be studied. In addition, results obtained using different mesh refinement criteria will be studied and the  $St_{sgs}$  parameter, discussed in Section 3.3, will be used as a refinement criterion and a post-processing parameter to analyze the influence of subgrid turbulence on spray dispersion. These proposed analyses lead to a simulation matrix presented in Tab. 3. All these simulations correspond to the conditions of ECN Test 1 case. Then the model using the  $St_{sgs}$  criterion for mesh refinement was also applied to ECN Test 2 case, to validate the model against other test conditions. This section is organized as follows: first the influence of mesh refinement is analyzed, showing that, contrary to what is stated in literature (BAUMGARTEN, 2006; SENEAL et al., 2013), the results are always improved as mesh is refined, which is expected, if adequate models are used. Then, the effect of STD and TAB models are analyzed and it is shown that, even including a model for the subgrid  $STD$ , it is not capable of reproducing the experimental values for liquid and vapor penetration, if certain level of mesh refinement is not attained. Finally, results are analyzed in view of the  $St_{sgs}$  parameter.

In the liquid and vapor penetration comparisons, the cases from Table 3 are identified with the label of the first column in the table and the case from SANDIA (ECN) (Tab. 2) are identified in the plots as liquid and vapor pen-

Table 3 – Cases' Definition

| Case name                                       | AMR levels  | Parcel counts                   | Droplet distortion (TAB) | Stochastic turbulent dispersion (STD) | Refinement criterion    |
|---|-------------|---------------------------------|--------------------------|---------------------------------------|-------------------------|
| AMR2A<br>AMR2B<br>AMR2C<br>AMR2D                | 2           | 500k<br>1000k<br>2000k<br>3000k | Off                      | Yes                                   | Vaporized Fuel Fraction |
| AMR4A<br>AMR4B<br>AMR4C<br>AMR4D                | 4           | 500k<br>1000k<br>2000k<br>3000k | Off                      | Yes                                   | Vaporized Fuel Fraction |
| AMR2B<br>AMR4B<br>AMR5B                         | 2<br>4<br>5 | 1000k                           | Off                      | Yes                                   | Vaporized Fuel Fraction |
| AMR2BNoSTD<br>AMR4BNoSTD<br>AMR5BNoSTD          | 2<br>4<br>5 | 1000k                           | Off                      | No                                    | Vaporized Fuel Fraction |
| AMR2BTAB<br>AMR4BTAB                            | 2<br>4      | 1000k                           | On                       | Yes                                   | Vaporized Fuel Fraction |
| AMR2ANoSTD St<br>AMR4ANoSTD St<br>AMR5ANoSTD St | 2<br>4<br>5 | 500k                            | Off                      | No                                    | Droplet Stokes Number   |

etration ECN. For the results comparison, as recommended in the 2<sup>nd</sup> ECN Workshop (ECN, ), the liquid length penetration is defined as the distance from the nozzle outlet to the farthest axial position encompassing 99% of the injected mass, and the vapor penetration is defined as the maximum distance from the nozzle outlet to where the fuel mass fraction is 0.1%. In all cases a maximum cell count of 3 million cells have been used.

#### 4.2.1 Effect of Mesh Refinement and Parcel Number

Figure 25 shows the cases with minimum cell sizes of  $250\mu\text{m}$  and varying the number of injected parcels, using STD model. It can be seen that all 4 cases are not capable of correctly capturing the initial ramp for both liquid and vapor penetrations (zoomed view). The ramp inclination angle is smaller in the simulation cases and liquid and gas penetrations are later over predicted.

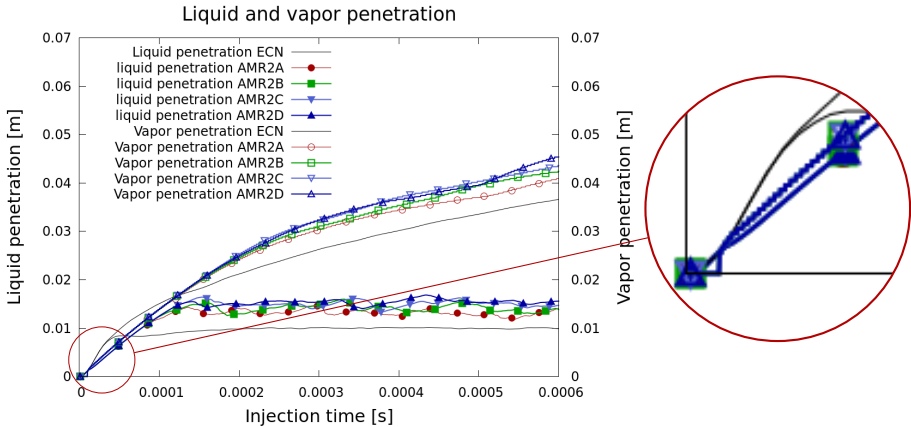


Figure 25 – AMR2 parcel count impact on liquid and vapor penetration.

Fig. 26 shows the cases with minimum cell sizes of  $62.5\mu\text{m}$  and varying the number of injected parcels, using STD model. The initial ramp for both liquid and vapor penetration are better captured than the previous cases with coarser mesh sizes (zoomed view). Liquid penetration, after an initial overshoot (after initial ramp), shows good agreement with the experimental results. The vapor penetrations also show good agreement with the experimental results. Cases with 500k and 1000k parcels show better agreement

with experiments for both liquid and vapor penetration but, in general, it is observed that the parcel number does not have strong influence in liquid and vapor penetration results, assuming that a minimum ratio of 130k parcels / mg of injected fuel mass is used.

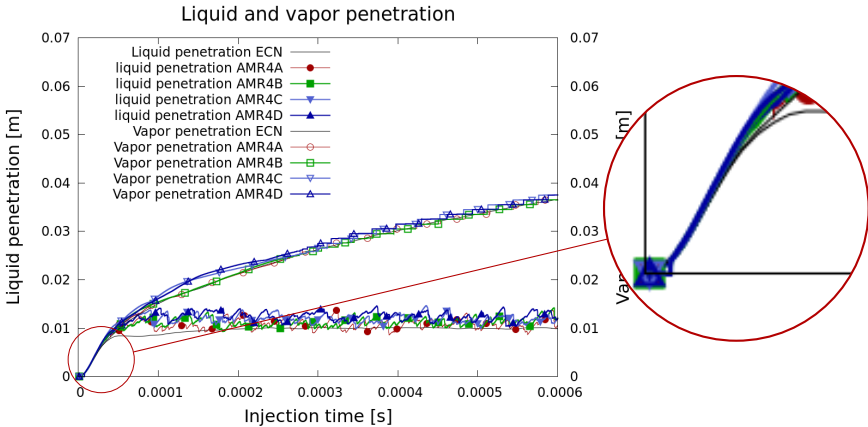


Figure 26 – AMR4 parcel count impact on liquid and vapor penetration.

A possible explanation for the observed behavior in figs. 25 and 26 is as follows. In the initial part of the injection, the controlling parameter is momentum transfer, while later, in the plateau region, is the turbulent dispersion. In the coarser mesh, the momentum transfer between parcel and gas phase is too fast leading to lower liquid length penetration. After the initial ramp the most important effect on liquid penetration is the turbulent dispersion, which is not adequately captured with this coarse mesh, even using STD model. As the mesh is further refined to size  $62.5\mu\text{m}$  the momentum transfer in the ramp is better captured, as well as the turbulent dispersion in the steady-state condition thus leading to the correct prediction of penetration lengths.

Figure 27 shows mean relative gas velocity in a cross section plane through the injector centerline and the spray parcels at 0.05 ms after start of injection, where it is possible to see the very high relative velocity diffusion with a coarse mesh (AMR2) vs. the case with a finer mesh (AMR4). This reinforces the fact that the controlling parameter in the initial ramp is the momentum transfer, leading to a reduced penetration with the coarse mesh. In addition, as the relative velocity affects the break-up, the mean droplet diameter decreases much more rapidly in the coarse mesh, as can be seen by the droplets' size, as both images have the same scale factor based on the droplets' diameter.



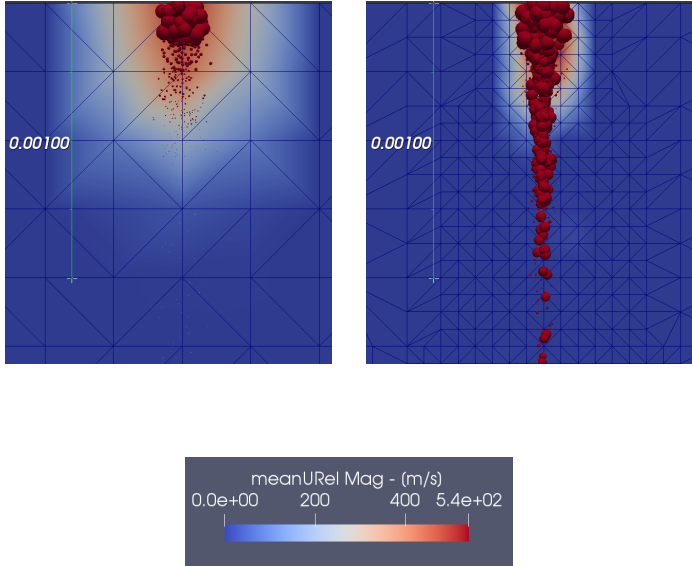


Figure 27 – Mean relative gas velocity in a cross-section plane through the injector centerline and spray parcels - AMR2 (left), AMR4 (right) at 0.05 *ms*.

Figure 28 shows, for cases with 4 and 5 levels of cell refinement without the usage of STD modeling, the subgrid turbulent kinetic energy. It is possible to verify a very high reduction as a consequence of mesh refinement. The maximum value has reduced approximately 45%, which has led to the improvement in the droplet's dispersion without the usage of the turbulent dispersion model. In fact, although not shown because color map plots are visually similar, when including STD model, the increase of subgrid turbulent kinetic energy was about 2% when including the model in the refined grid (AMR5), and about 10% in the coarse mesh, showing that the effect of STD model reduces as mesh is refined and, eventually, it could be avoided.

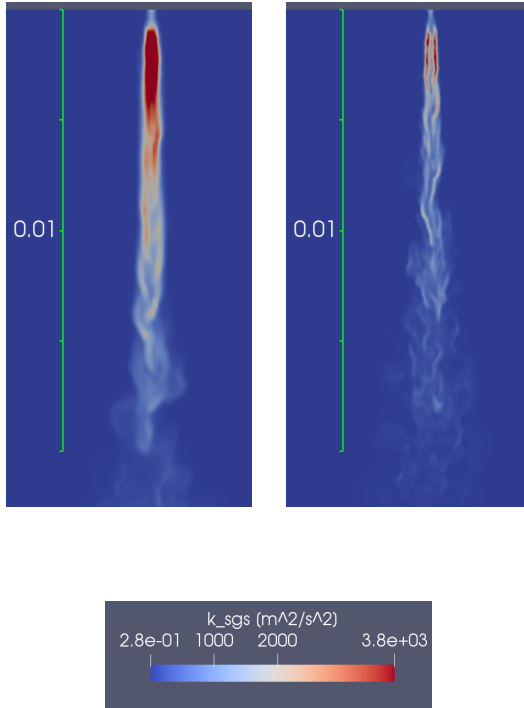


Figure 28 – Subgrid turbulent kinetic energy with AMR4 (left) and AMR5 (right) at 0.15 *ms* without STD.

In Fig. 29, iso-surfaces of  $\lambda_2 = 10^7$  parameter, are presented for cases with 2, 4 and 5 levels of cell refinement without the usage of STD modeling. It can be seen that, beyond the correct prediction of penetration, the whole structure of the turbulence induced in gas phase is changed, as the mesh is refined. Due to less momentum dissipation, a more "conical" turbulence structure is observed, with less radial influence near the injector and opening the angle as spray penetrates in the chamber, which is physically expected.

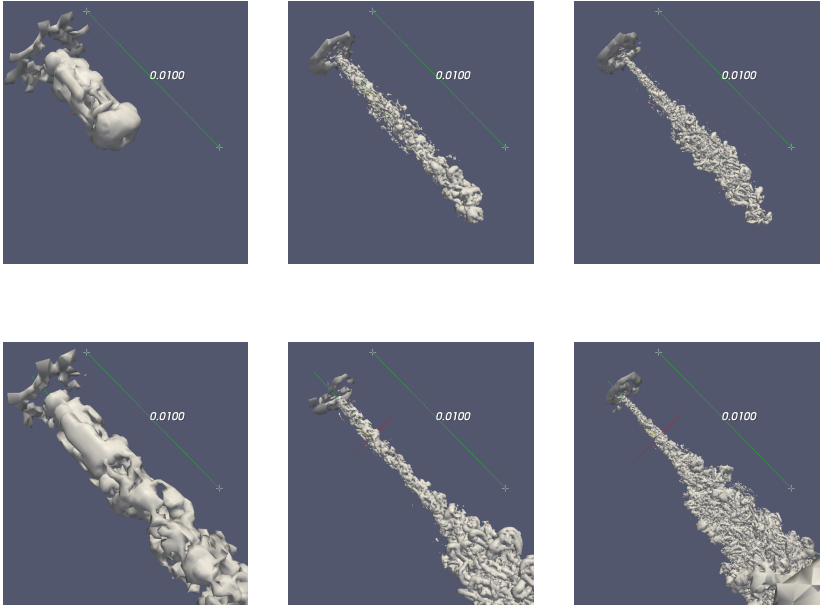


Figure 29 –  $\lambda_2$  iso-surfaces for AMR2B (left), AMR4B (center), AMR5B (right) without STD at 0.05ms, 0.15ms (1<sup>st</sup> and 2<sup>nd</sup> rows respectively).

Figure 30 presents the vapor distribution for different meshes (2, 4 and 5 levels of cell refinement without STD modeling) showing that, besides the penetration parameter, which is compared with experiments, the shape of the resulting vapor region is also seriously affected by the mesh refinement which will probably affect the combustion in the reacting case.

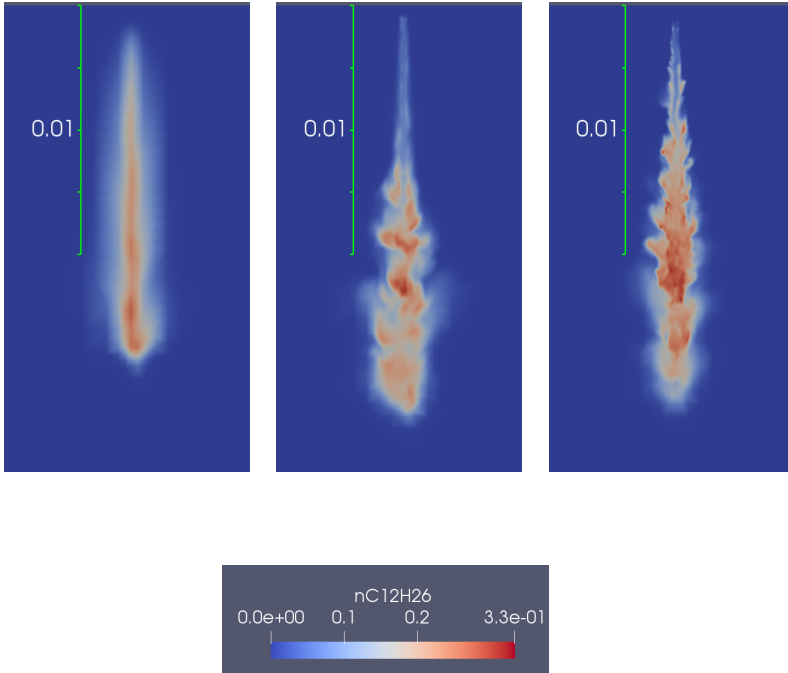


Figure 30 –  $nC_{12}H_{26}$  vapor distribution - AMR2A (left), AMR4A (center) and AMR5A (right), all without STD at 0.10ms.

Fig 31 shows for the cases from Fig. 30, the definition of 0.1% of vapor fuel mass fraction used to set the boundary of the vapor phase and thus, the vapor length penetration.

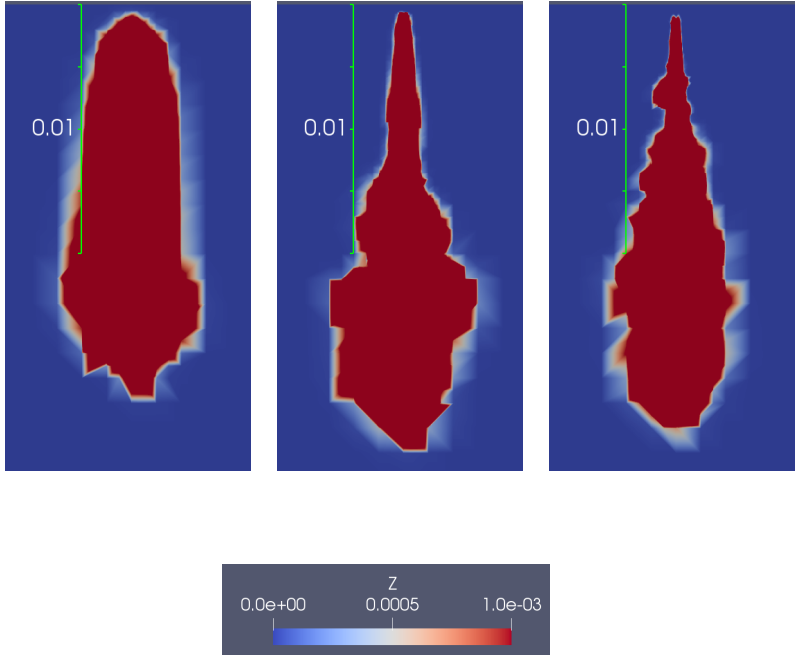


Figure 31 – Vapor penetration criterion - 0.1% of mass fraction distribution - AMR2A (left), AMR4A (center) and AMR5A (right), all without STD at 0.10ms.

#### 4.2.2 Effect of STD and TAB models

Figure 32 shows the impact of inclusion of subgrid *STD* modeling in the liquid and vapor length penetrations considering the mesh refinement effect. The comparisons are made among *AMR*2, 4 and 5 with 1000k injected parcels with and without stochastic turbulent dispersion (*STD*) modeling. It becomes clear that, as the velocity field is not properly resolved (coarse mesh - *AMR*2), the inclusion of *STD* does not suffice to get a correct prediction of the liquid and vapor length penetrations. When *STD* is used with a coarse mesh it attempts to improve the result, leading to lower liquid length penetration, but still seriously over-predicting it. Furthermore, even not reaching the correct penetration lengths with the mesh sizes used in these simulations, when *STD* model is not included (Fig. (32-(b)), a clear trend is observed in the way that this model has less impact on penetration as mesh is refined. As

discussed in section 3.3, it is expected that, as droplet Stokes number associated to subgrid eddies increases over unity, the effect of *STD* model becomes negligible.

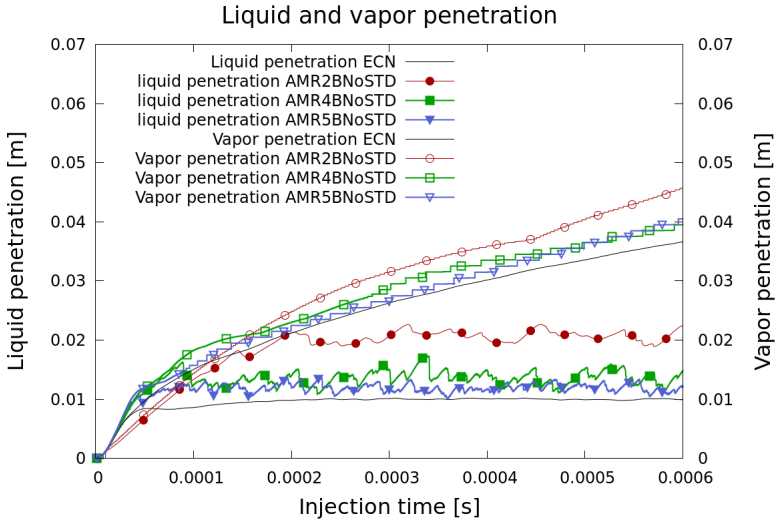
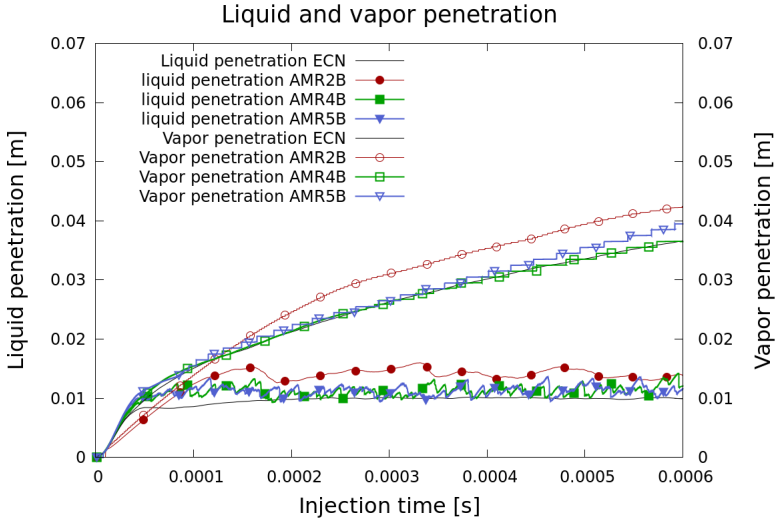
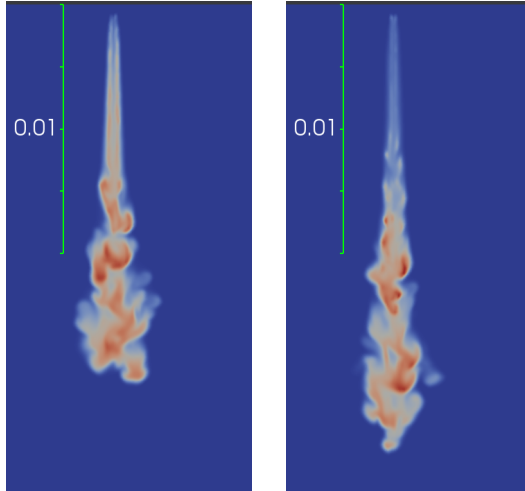


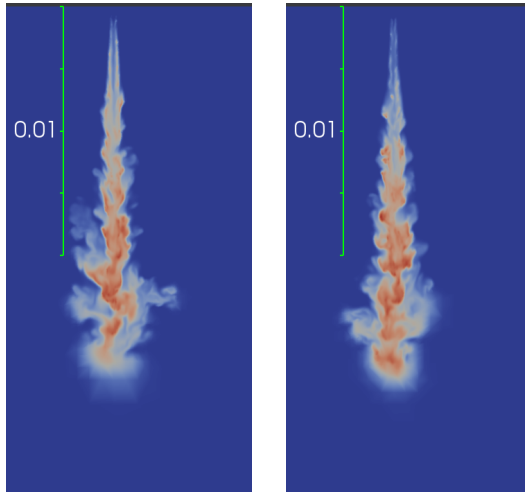
Figure 32 – Mesh size impact on liquid and vapor penetration (a) with STD model and (b) without STD model.

Figure 33 shows the effect of STD model on n-Dodecane vapor distribution for the cases with 4 and 5 levels of cell refinement. Besides the penetration length the inclusion of the model also affects the whole spray morphology (angle and thickness). However, when mesh is refined the effect of STD model becomes less significant for vapor penetration and shape.





(a) AMR4 with STD (left) and without STD (right) at 0.10ms.



(b) AMR5 - with STD (left) and without STD (right) at 0.10ms.



Figure 33 –  $nC_{12}H_{26}$  vapor distribution.

Figure 34 shows the cases where the dynamic droplet distortion model is used with the same injected parcel numbers and varying minimum cell sizes, as a result of the *AMR* levels. It indicates a dependency of the mesh size for the TAB model showing that with the coarser mesh (*AMR2*) the liquid length penetration with TAB distortion model is actually higher than without it, and as the mesh is refined (*AMR4*) the liquid length penetration with and without TAB distortion modeling approximate each other.

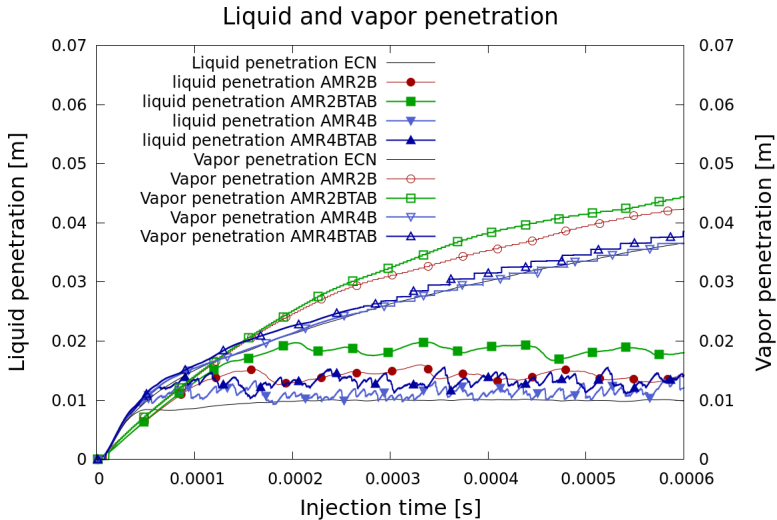


Figure 34 – AMR2 and 4 - 1000k parcels - Dynamic droplet distortion impact on liquid and vapor penetration.

### 4.2.3 Analysis based on $St_{sgs}$ and proposed mesh refinement criterion

In the following analyses all results are presented for the cases without STD model in order to visualize the actual effect of subgrid turbulence on spray dispersion, i.e., in these cases, only resolved scales are considered in spray dispersion. Figure 35 shows the comparison droplet Stokes number distribution for AMR2, AMR4 and AMR5 cases, without STD modeling, using the droplet Stokes number (Eq. 3.6) as mesh refinement criterion. It is possible to see that as the mesh is refined the droplet Stokes number based on subgrid eddies characteristic time, increases indicating that the unresolved eddies are reducing their impact in the droplet dispersion.

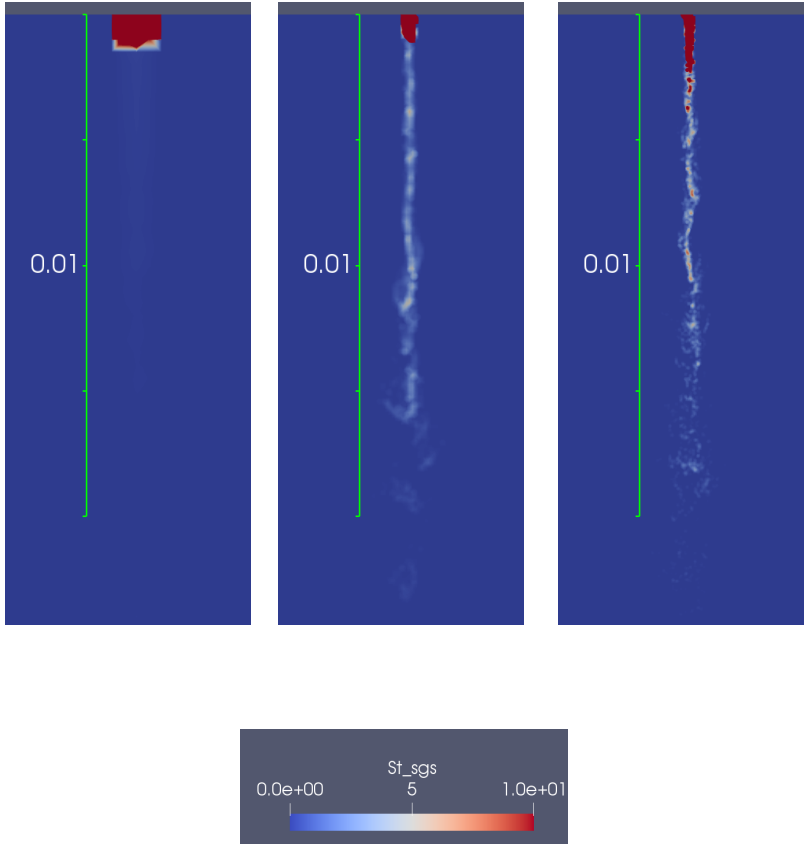


Figure 35 – Droplet Stokes number with AMR2 (left), AMR4 (center) and AMR5 (right) without STD at 0.10ms.

Figure 36 shows the droplet Stokes number plot over a line along the centerline of the spray closer to the injector tip ( $1^{st}$  row) and further away ( $2^{nd}$  row) at 0.10ms after the start of injection, considering different mesh sizes (AMR2, 4 and 5 without STD). In Fig. 37 plots for droplet Stokes number along an horizontal line  $4mm$  below the injector tip are shown. It is clearly observed that as the mesh is refined, the droplet Stokes number increases indicating that the unresolved vortices are reducing their impact in droplet dispersion.

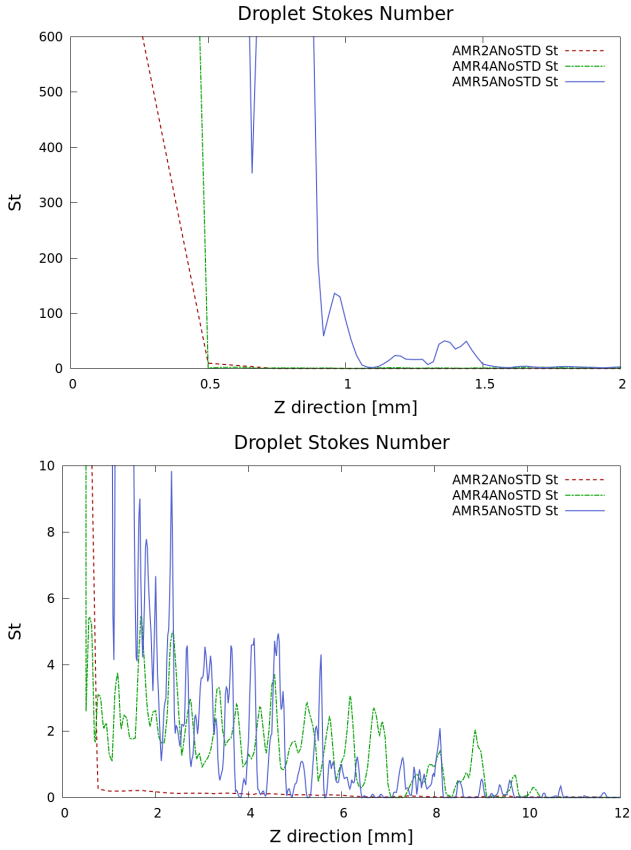


Figure 36 – Droplet Stokes number plot along the injector centerline, closer to the injector tip ( $1^{st}$  row) and further away ( $2^{nd}$  row) without STD at 0.10ms.

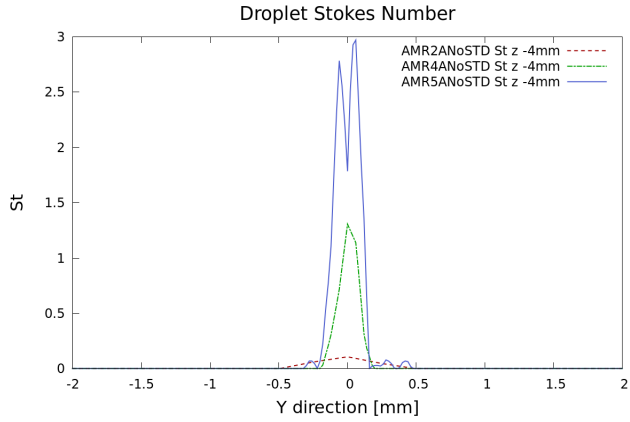


Figure 37 – Droplet Stokes number plot along an horizontal line 4 mm below the injector tip without STD at 0.10ms.

Figure 38 shows the liquid and vapor penetration curves comparing cell refinement levels and using the Stokes criterion. It is possible to see a good agreement with the experiments for both 4 and 5 levels of cell refinement.

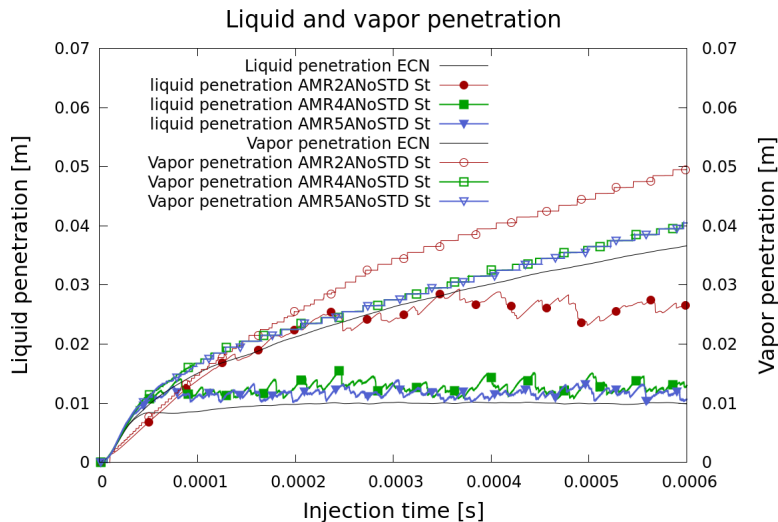


Figure 38 – Liquid and vapor penetration for different refinement levels, using Stokes criterion, without STD modeling.

However as shown in Fig. 30 for the vapor phase distributions of n-Dodecane for the AMR4 and AMR5 cases, at 0.10ms after start of injection, there is a distinct difference between them. So even though the liquid and vapor penetrations lengths are very similar, the actual fuel distribution in the domain is significantly different.

To confirm the proposed mesh refinement criterion, a second experimental setup from ECN was simulated (ECN Test 2), as shown in Tab. 2. Figure 39 shows the comparative result for liquid length penetration against the ECN Test 2 using the criterion for cell refinement proposed in Eq. 3.6, where it can be seen a good agreement with the experimental results shown. For the simulation of this case the same spray sub-models and spray breakup parameters (Tab. 1) as in case 1 have been used.

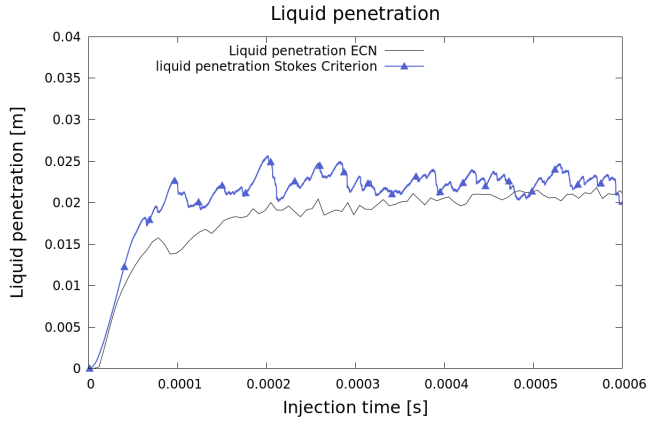


Figure 39 – Comparison to ECN Test 2 with AMR5 using the  $St_{sgs} \geq 1$  criterion.

### 4.3 LES TURBULENT KINETIC ENERGY RESOLUTION

This section presents, based on an analogous approach described in Pope (2001), the ratio between the residual kinetic energy (the subgrid  $k_{sgs}$ ) to the total turbulent kinetic energy,

$$k = \frac{1}{2}(U_i'U_i') + k_{sgs}, \quad (4.1)$$

as a method to evaluate how much of the energy contained in the turbulent flow is resolved, where  $U_i'$  is the resolved fluctuation velocity and not the subgrid model fluctuation velocity ( $u_i'$ ).

With the information about the total kinetic energy contained in the flow, and the subgrid scale turbulent kinetic energy, it is possible to evaluate to what extent the energy contained in the flow structures are being resolved, given by,

$$1 - \frac{k_{sgs}}{k} \quad (4.2)$$

This method was post-processed comparing 3 levels of cell refinement used with LES (AMR2, AMR4 and AMR5) and shown in Fig. 40, where it is possible to identify that with 5 levels of cell refinement a very large part of the turbulent energy is being resolved in the spray jet region. On the other hand, with a coarser mesh (AMR2) this ratio is lower, in the spray jet region, which

indicates that only a small fraction of the energy contained in the turbulent structures is being resolved.

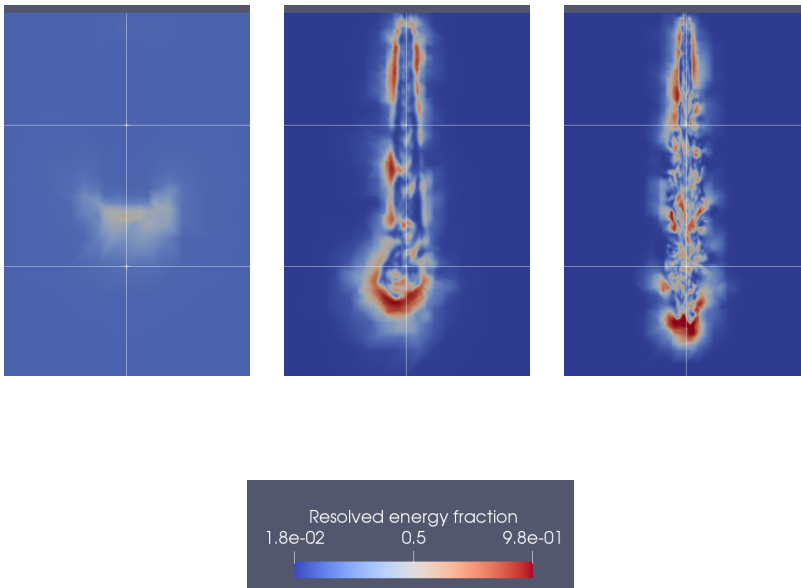


Figure 40 – Fraction of turbulent energy resolved for AMR2 (left), AMR4 (center) and AMR5 (right) meshes, at 0.05ms after start of injection.

Assessment of Fig. 40 is further detailed by comparing among the 3 levels of cell refinement, plotting the value of the resolved turbulent flow energy, in a vertical line passing through the centerline of the fuel spray jet (Fig. 41),



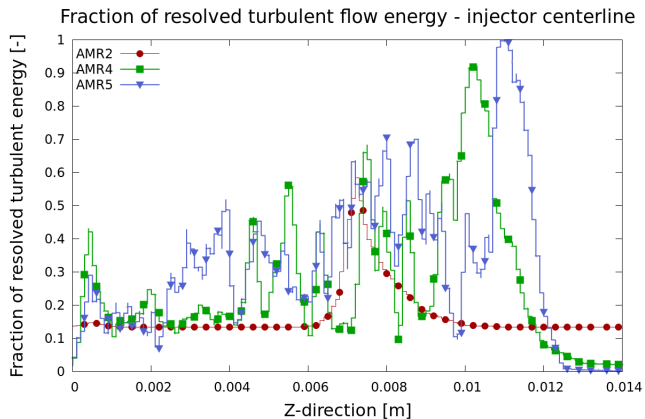


Figure 41 – Fraction of the turbulent flow energy resolved plot along the centerline of the injector, at  $0.05ms$  after start of injection.

and in a horizontal line passing at a position  $4mm$  below the fuel injector tip (Fig. 42),

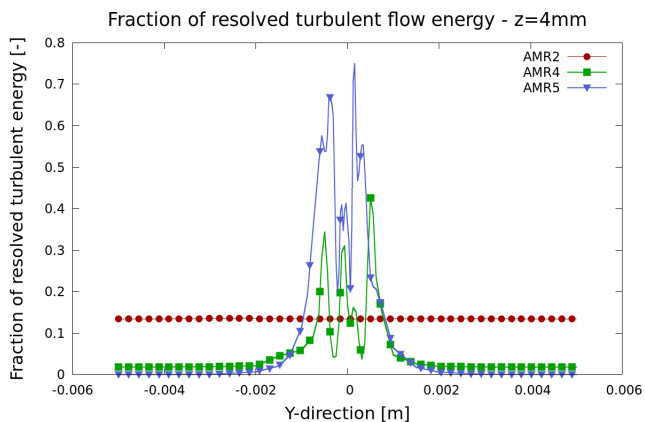


Figure 42 – Fraction of the turbulent flow energy plot along an horizontal line  $4mm$  below the injector tip, at  $0.05ms$  after start of injection.

and  $9mm$  below the fuel injector tip (Fig. 43),

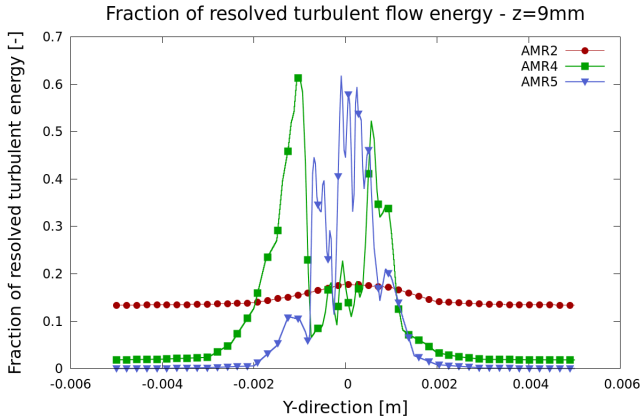


Figure 43 – Fraction of the turbulent flow energy plot along an horizontal line  $9\text{mm}$  below the injector tip, at  $0.05\text{ms}$  after start of injection.

where it is possible to observe that with AMR2 only a small fraction of the energy is resolved, and thus contradicting the statement from Irannejad and Jaberi (2014) and Keller et al. (2015) that is mentioned in section 3.1. It is also clear from the figures that as the mesh is refined, more of the energy contained in the flow is resolved, and even though the fact that the AMR4 is similar to AMR5 regarding flow energy capture, as discussed previously, the AMR5 is better in capturing the spray-turbulence interactions.

#### 4.4 COMPARISON BETWEEN RANS AND LES

As RANS is the usual turbulence modeling choice in industrial applications for internal combustion engine modeling, this section presents a comparison between RANS and LES turbulence modeling impact concerning liquid and vapor length penetrations. The modified RNG  $k - \varepsilon$  turbulence model from Han and Reitz (1995) presented in section 2.2.2 is used.

Concerning the numerical schemes used for RANS cases, first order discretization is used for the time derivatives and second order discretization scheme for convection and diffusion terms. The same limit as in the LES simulations was used for the maximum CFL number, 0.25. The pressure-velocity coupling algorithm used is PIMPLE. Regarding the solution of resulting linear systems, pressure and density are solved with a matrix symmetric solver, Preconditioned Conjugate Gradient (PCG) using a Diagonal Incomplete-Cholesky (DIC) preconditioner, while velocity, enthalpy, turbu-

lent kinetic energy and turbulent dissipation, are solved with a Preconditioned Bi-Conjugate Gradient (PBiCG), with a Diagonal Incomplete-LU (DILU) preconditioner.

In order to analyze only the single effect out of the turbulence modeling, the final refined meshes obtained at the end of the LES case with AMR 4 and 5 (Fig. 44), have been used in the RANS case and the adaptive mesh refinement has not been used. Therefore, the RANS based model cases was run with the same grid meshes as the ones used in the LES cases.

All cases that are part of the analyses do not include the STD modeling, thus relying only on the resolved part of the velocity fields in order to account for the turbulent dispersion of the droplets. Dynamic droplet drag distortion model is also not included.

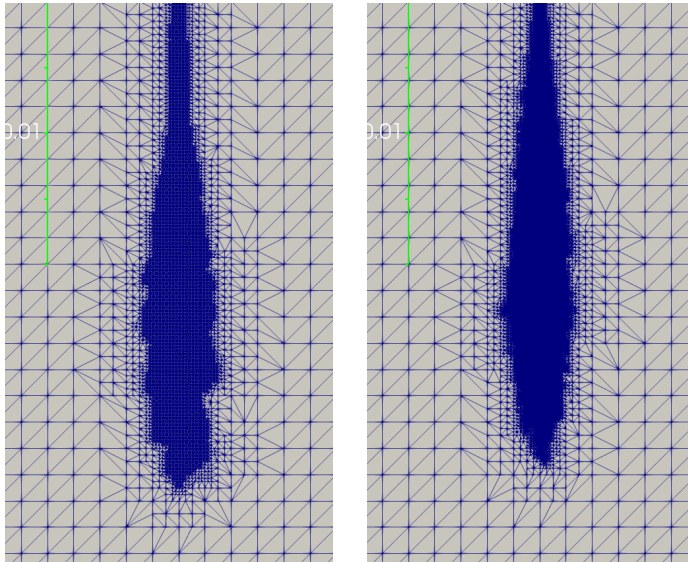


Figure 44 – Refined mesh from LES simulated cases used as fixed meshes for the RANS simulated cases - 4 levels of refinement (left) and 5 levels of refinement (right).

Prior to assessing the results below, it is useful to summarize what has been shown in section 2.3.1 regarding droplet breakup models and the impact of the relative velocity between gas and droplet. In the Kelvin-Helmholtz breakup model, the drop-gas relative velocity impacts the maximum growth rate and wavelength of the perturbation in the surface, thus modifying the model droplet breakup time ( $\tau_{KH}$ ). In the Rayleigh-Taylor breakup model,

the drop-gas relative velocity impacts on the acceleration/deceleration of the droplets, and as a consequence also modifying the model's droplet breakup time ( $\tau_{RT}$ ).

A comparison of the RANS averaging of the velocity field solution with the LES filtering approach results in significant differences in the velocity flow field (Fig. 45), for the same simulated conditions and mesh.

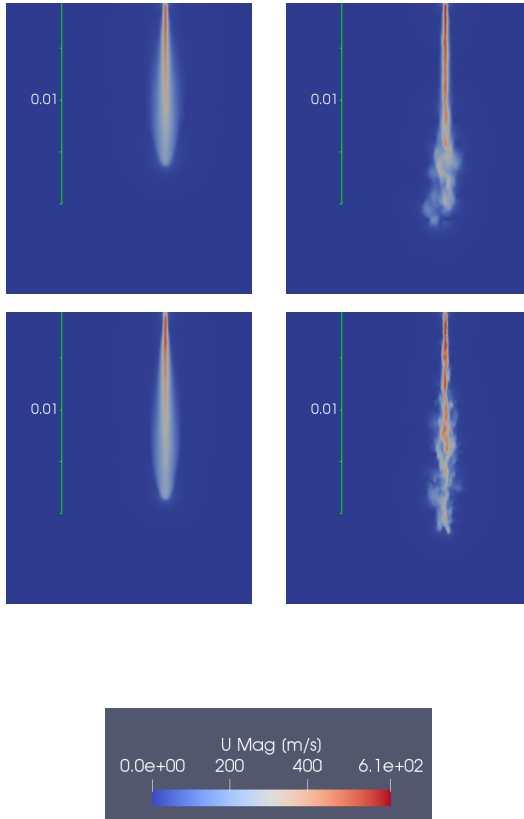


Figure 45 – Gas velocity magnitude RANS (left) and LES (right) with 4 and 5 levels of cell refinement (1<sup>st</sup> and 2<sup>nd</sup> rows respectively), at 0.05ms after start of injection.

This can also be seen, in more detail, in Fig. 46 for the mesh with 4 levels of refinement and in Fig. 47 for the mesh with 5 levels of refinement, where the gas velocity along the centerline of the spray is plotted, compar-

ing RANS vs. LES cases at 0.05ms after start of injection (the injector is placed in the  $Z=0\text{m}$  coordinate). There is clear distinction between RANS and LES cases, where only minor velocity fluctuations are present for both RANS cases and also related to the magnitude of the velocity field.

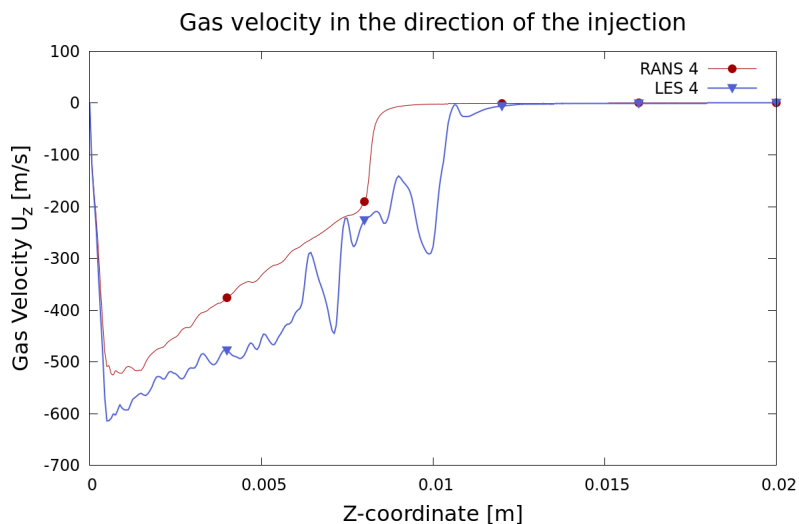


Figure 46 – Comparison between RANS and LES on z-component of gas velocity at 0.05ms after start of injection with the mesh from the AMR4 LES case.

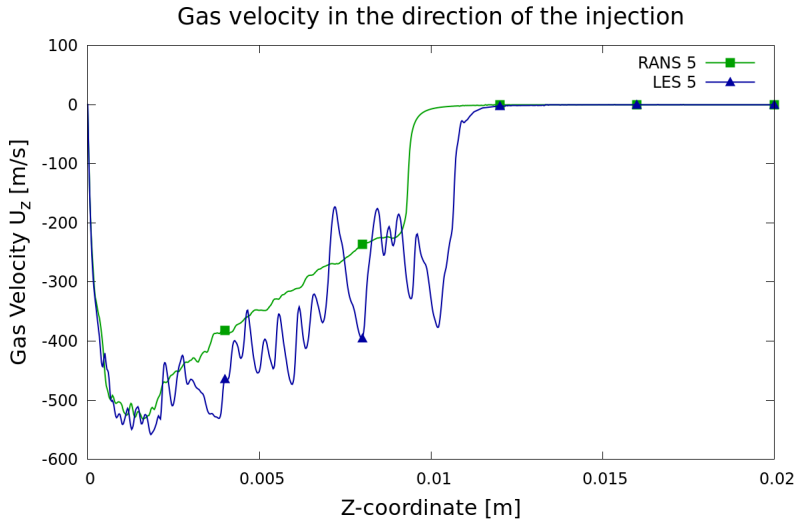


Figure 47 – Comparison between RANS and LES on z-component of gas velocity at 0.05ms after start of injection with the mesh from the AMR5 LES case.

As discussed previously, it is expected that the droplet-turbulence interaction is poorly characterized with RANS.

A volume average of parcel velocities calculated at 0.05ms after the start of injection comparing the RANS and LES with the finer mesh (5 levels of refinement) is shown in Fig. 48, where it is possible to see that the average velocities of the parcels are very similar.

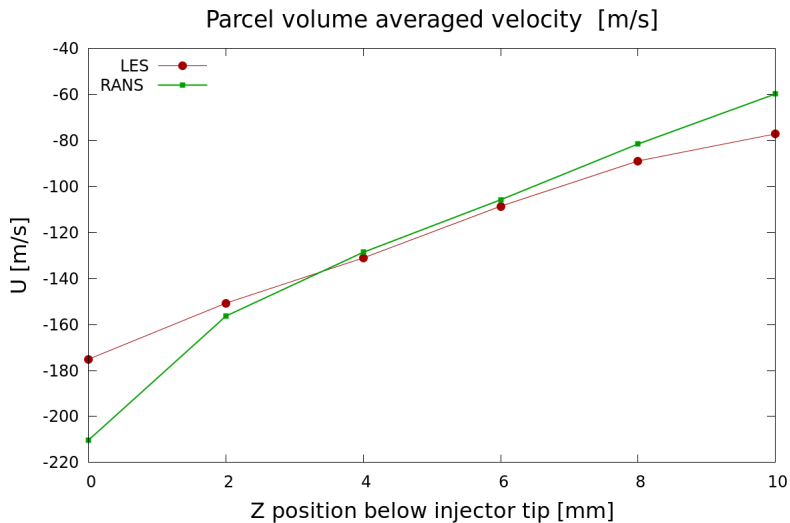


Figure 48 – Volume average of parcel velocity evaluated at different positions below the injector tip.

A 3D view of the spray parcels, with constant size to make visualization easier, and colored by z-component of velocity and droplet drag can be seen in Figures 49 and 50, respectively, where it is also possible to see qualitatively that there is no significant difference between them.

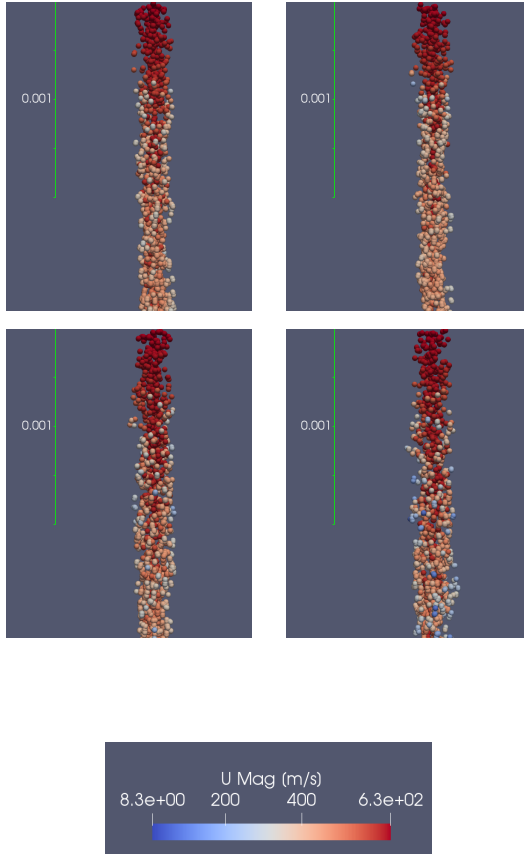


Figure 49 – Droplet velocity magnitude RANS (left) and LES (right) with 4 and 5 levels of cell refinement (1<sup>st</sup> and 2<sup>nd</sup> rows respectively), at 0.05ms after start of injection.

Analyzing the drag in cases with 5 levels of cell refinement for both RANS and LES, the difference between the maximum drag that the parcels are subjected to is of less than 1%. Only less than 1% of the parcels in either LES or RANS cases subjected to a drag of the order  $10^{-3}$  to  $10^{-2}N$ , with more than 99% of the parcels subjected to a drag in the order of  $10^{-4}N$ .



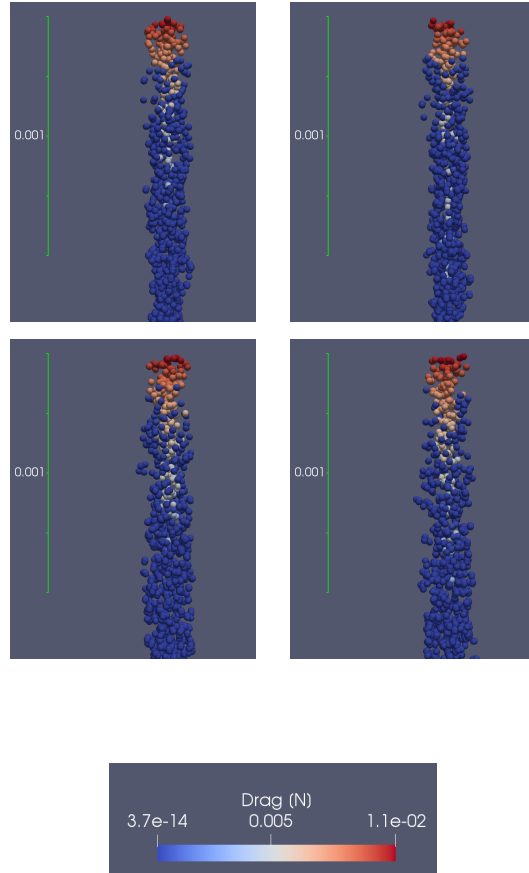


Figure 50 – Droplet drag RANS (left) and LES (right) with 4 and 5 levels of cell refinement (1<sup>st</sup> and 2<sup>nd</sup> rows respectively), at 0.05ms after start of injection.

Looking at the liquid and vapor length penetration results (Figures 51 and 52), it is possible to see that the ramp part of the spray is not properly captured in the RANS cases. The liquid length overshoots and later reduces abruptly, but still with a higher error. The cause of the abrupt variation in liquid length penetration is not clear. Vapor length penetration starts smaller than the experimental data but after approx. 0.3ms matches well with the experimental data in both RANS cases.

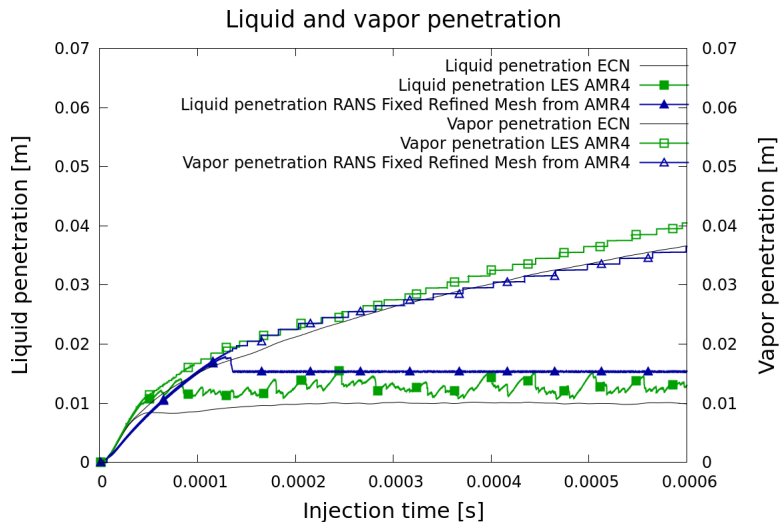


Figure 51 – Comparison among LES and RANS on liquid and vapor length penetrations with the mesh from AMR4 LES case.

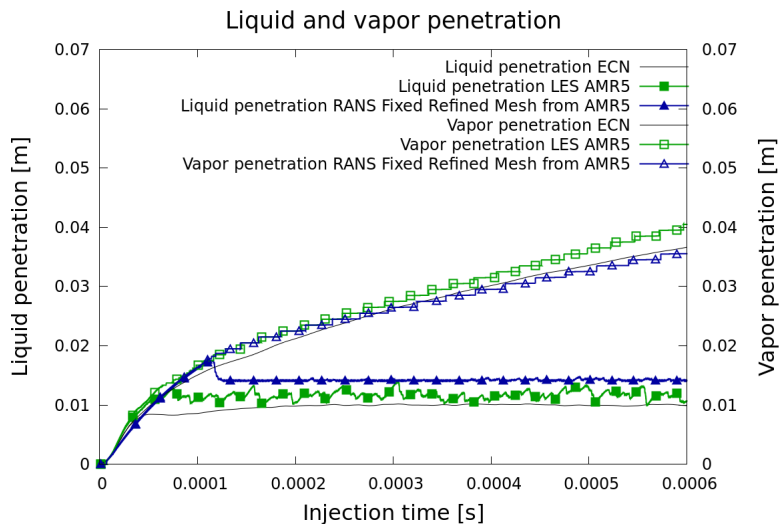


Figure 52 – Comparison among LES and RANS on liquid and vapor length penetrations with the mesh from AMR5 LES case.

Putting together the description of the breakup models, and the observation of the velocities for gas and droplet and the resulting similar drag, this leads to the conclusion that the most important effect that the turbulence model impacts on the spray is due to the gas velocity field and as a consequence on the turbulent dispersion of the droplets. As expected, even with the same mesh, RANS turbulence modeling is very dissipative and cannot capture the necessary flow structures for a proper characterization of the spray-turbulence interaction.

Even though vapor penetration appears better with RANS than with LES in the figures above, the vapor distribution is completely different (Figures 53 and 54), showing a distribution nearly without disturbances which is not correct, as can be seen from the Schlieren image from this experiment showing the vapor region border (Fig. 55).

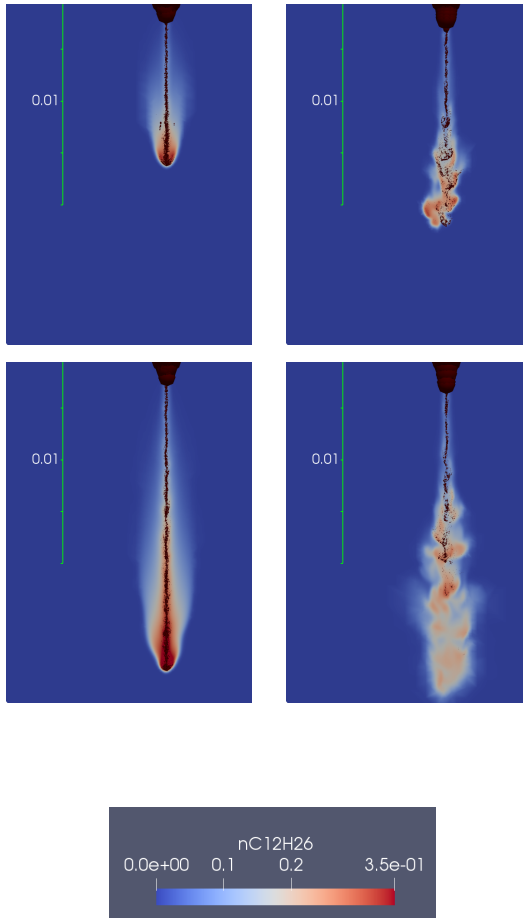


Figure 53 –  $nC_{12}H_{26}$  vapor distribution with 4 levels of cell refinement mesh RANS (left) and LES (right), at 0.05ms and 0.10ms (1<sup>st</sup> and 2<sup>nd</sup> rows respectively).

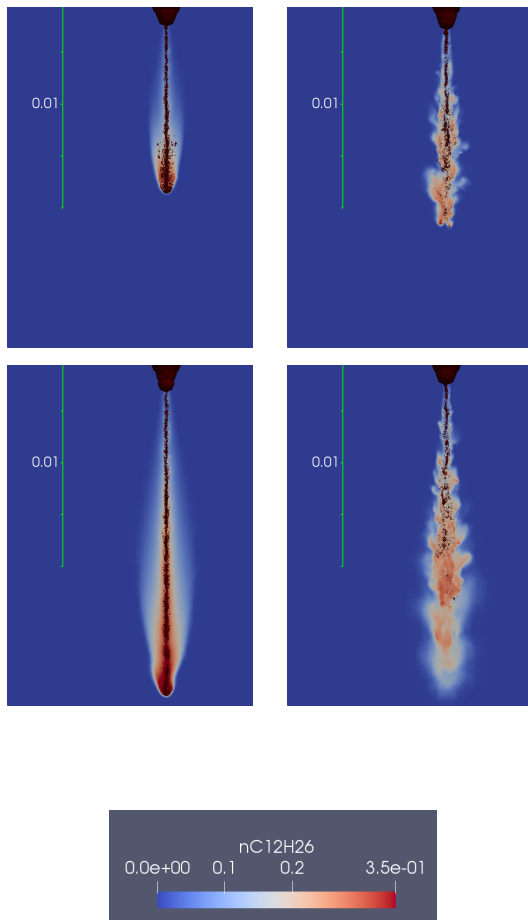


Figure 54 –  $nC_{12}H_{26}$  vapor distribution with 5 levels of cell refinement mesh RANS (left) and LES (right), at 0.05ms and 0.10ms (1<sup>st</sup> and 2<sup>nd</sup> rows respectively).

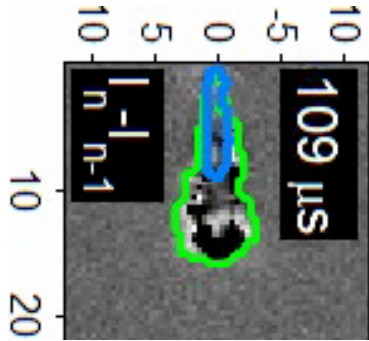


Figure 55 – Schlieren image extracted from the Sandia experiment showing vapor region border at 0.10ms.

Due to the different approaches in solving the turbulent kinetic energy a comparison in the turbulent kinetic energy modeled via RANS with the total kinetic energy from LES, is presented in Fig. 56, for the case with 5 levels of cell refinement.

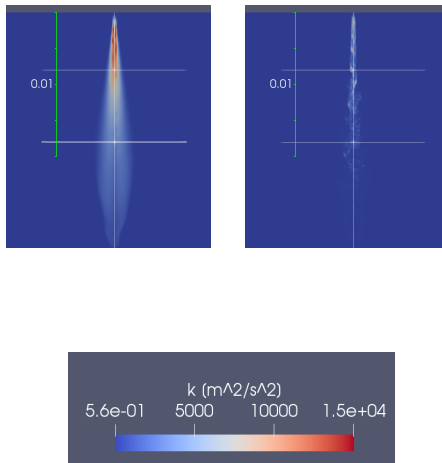


Figure 56 – Comparison between RANS turbulent kinetic energy (left) and LES total kinetic energy (right), at 0.10ms after start of injection.

A further assessment of Fig. 56 plotting the values for the turbulent kinetic energy assessed in a vertical line passing through the centerline of the fuel spray jet (Fig. 57),

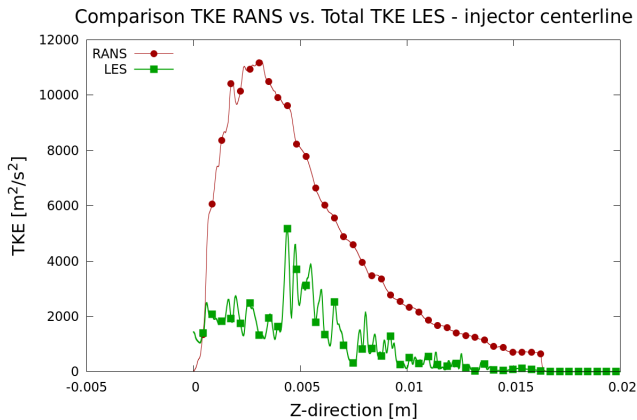


Figure 57 – Turbulent kinetic energy plot along the centerline of the injector, at  $0.10\text{ms}$  after start of injection.

in a horizontal line passing at a position  $4\text{mm}$  below the fuel injector tip (Fig. 58),

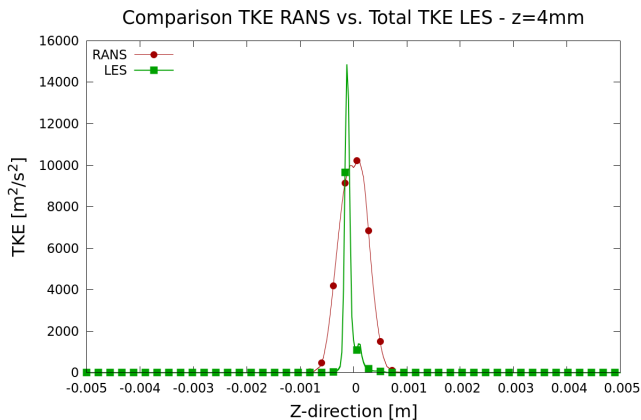


Figure 58 – Turbulent kinetic energy plot along an horizontal line  $4\text{mm}$  below the injector tip, at  $0.10\text{ms}$  after start of injection.

and  $9\text{mm}$  below the fuel injector tip (Fig. 59),

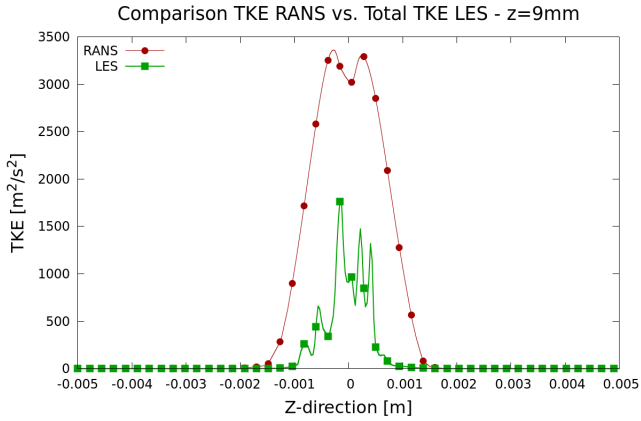


Figure 59 – Turbulent kinetic energy plot along an horizontal line  $9mm$  below the injector tip, at  $0.10ms$  after start of injection.

clearly show for the RANS model a significantly higher turbulent kinetic energy field.

Regarding the statement of more dissipative behavior of RANS modeling, the turbulent viscosities for RANS and LES subgrid are shown in Fig. 60, indicating that clearly for the RANS approach. The scales were left intentionally different for easy visualization of the contour plots, as the turbulent viscosity with RANS approach is 2 orders of magnitude higher than the subgrid turbulent viscosity with LES approach.



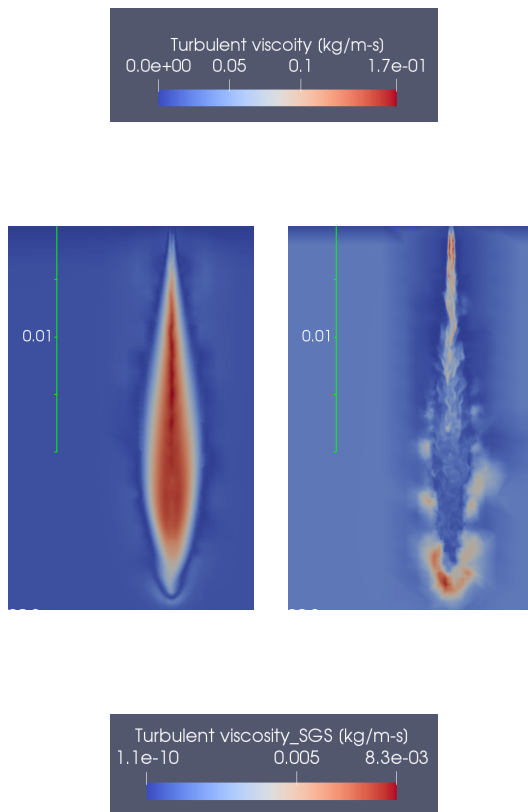


Figure 60 – Turbulent viscosity RANS (left) and LES (right) meshes with 5 levels of cell refinement, at 0.10ms after start of injection.

After this evaluation an attempt to use RANS modeling with AMR enabled has shown numerical instability limitations in the code, if attempting to use more than 3 levels of cell refinement. As a consequence with RANS it is only possible to go to a cell size as small as  $125\mu\text{m}$ , while with LES 5 levels of adaptive mesh refinement ( $31.25\mu\text{m}$ ) can be used, with the current implementation of AMR.

In Fig. 61 a comparison of liquid and vapor length penetrations between RANS and LES cases with AMR3 is shown, where it is possible to see that for RANS with 3 levels of cell refinement the vapor length penetration is correctly captured after approx.  $0.15\text{ms}$ , better than the LES case with

the same level of cell refinement. Even though the vapor penetration length is better correlated to the experiments with RANS than with LES, again the vapor phase distributions (Fig. 63), are completely different, and the same comments as presented before for the cases with 5 levels of cell refinement apply here. Liquid length penetration in both RANS and LES are over-predicted.

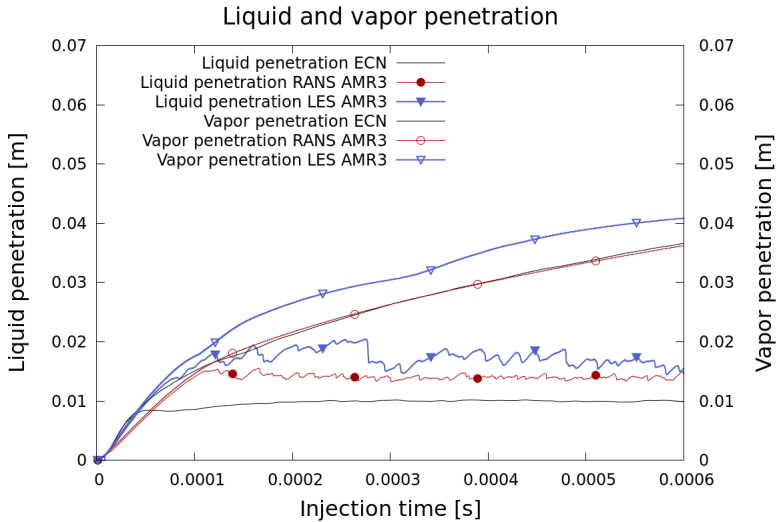


Figure 61 – Comparison among RANS and LES both with AMR enabled with 3 levels of refinement on liquid and vapor length penetrations.

It is worth mentioning that when using AMR3 for both cases, the resulting mesh is also different (Fig. 62).

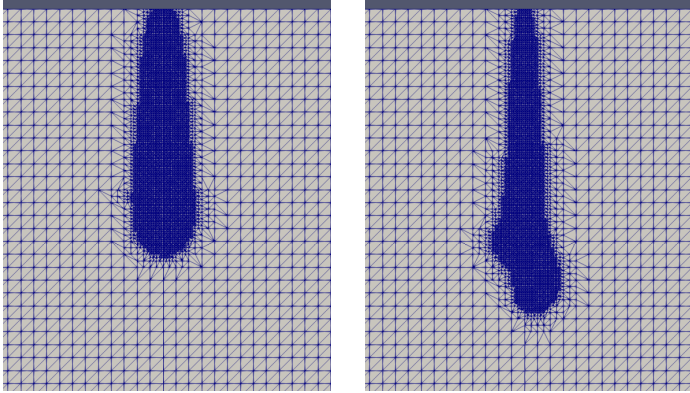


Figure 62 – Mesh at 0.05ms for RANS case (left) and LES (right).

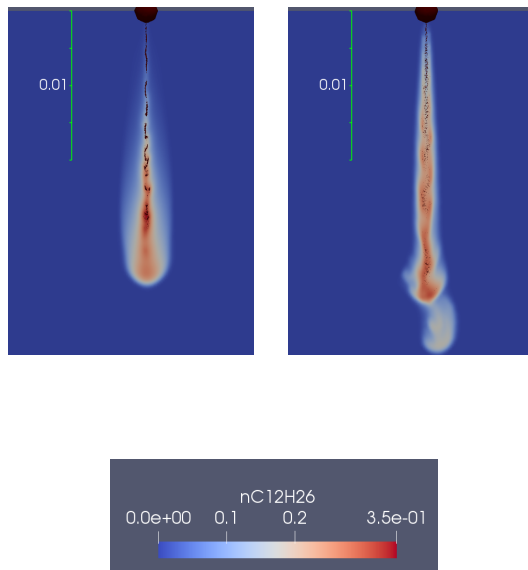


Figure 63 –  $nC_{12}H_{26}$  vapor distribution with AMR and 3 levels of cell refinement RANS (left) and LES (right), at 0.05ms after start of injection.



## 5 ANALYSES OF VESSEL CONDITIONS AND FUEL TYPE ON IMPORTANT SPRAY PARAMETERS AND ON MIXTURE FORMATION

In this chapter first an analysis regarding mesh refinement criteria is presented followed by a sensitivity analyses regarding vessel ambient pressure and temperature, and fuel's physical properties, with the objective to describe their impacts on important non-reacting spray characteristics, such as liquid and vapor length penetrations and vapor phase distribution. A comparison of the results with known empirical correlations for liquid length penetration, spray angle and Sauter Mean Diameter (SMD) is shown.

### 5.1 MESH REFINEMENT CRITERION COMPARISON

In the previous chapter two different mesh refinement criteria have been used, vaporized fuel fraction and droplet Stokes number. Here a direct comparison between them is presented in order to understand complementary and similarity behaviors.

A potential limitation of the vaporized fuel fraction criterion exists in cases with reduced rate of fuel vaporization, such as fuel injection in a vessel with a low ambient temperature or fuel injection with a low liquid temperature where it will take some time for the liquid to heat-up and then start to vaporize. In these scenarios the liquid jet can eventually lead the vapor front. In this scenario, relying only on the vaporized fuel fraction criterion will not suffice to track correctly the liquid fuel front and thus the mesh refinement will fail, directly impacting on the prediction accuracy of the liquid length penetration. In such cases the refinement based on droplet Stokes number seems to be a more adequate criterion.

Figure 64 shows a comparison between adaptive mesh refinement criteria, i.e., vaporized fuel fraction and droplet Stokes number, in liquid length penetration in a case with vessel's ambient temperature of 400K. It can be observed that the liquid length penetration does not stabilize as the evaporation is not enough to evaporate the droplets until a determinate spray length. Resulting meshes at 0.10ms after start of injection are shown in Fig. 65 and, in Fig. 66 the impact of these two refinement criteria is also shown in the vapor phase distribution, spray parcel dispersion, vapor concentration and shape.

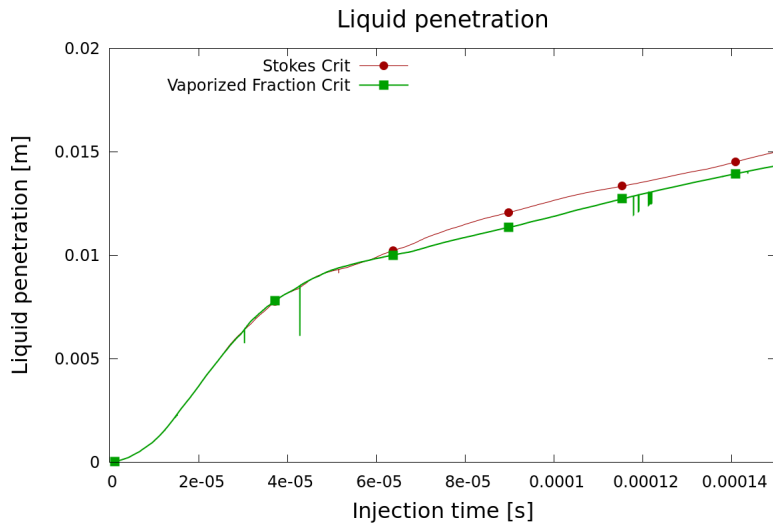


Figure 64 – Refinement criterion impact on liquid length penetration.

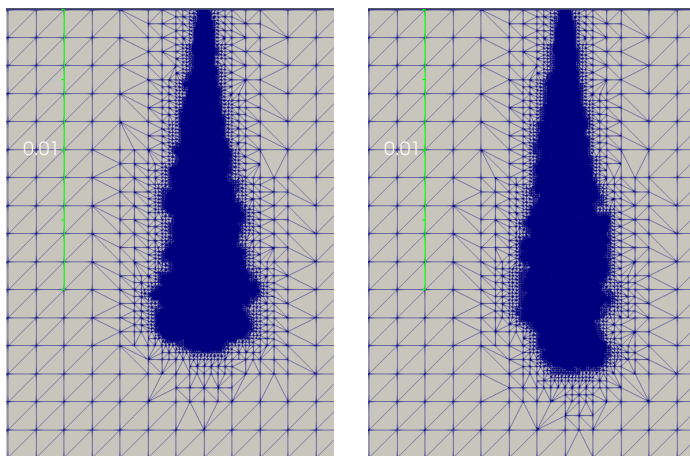


Figure 65 – Resulting mesh with vaporized fuel fraction criterion (left) and  $St_{sgs}$  criterion (right), at 0.10ms.

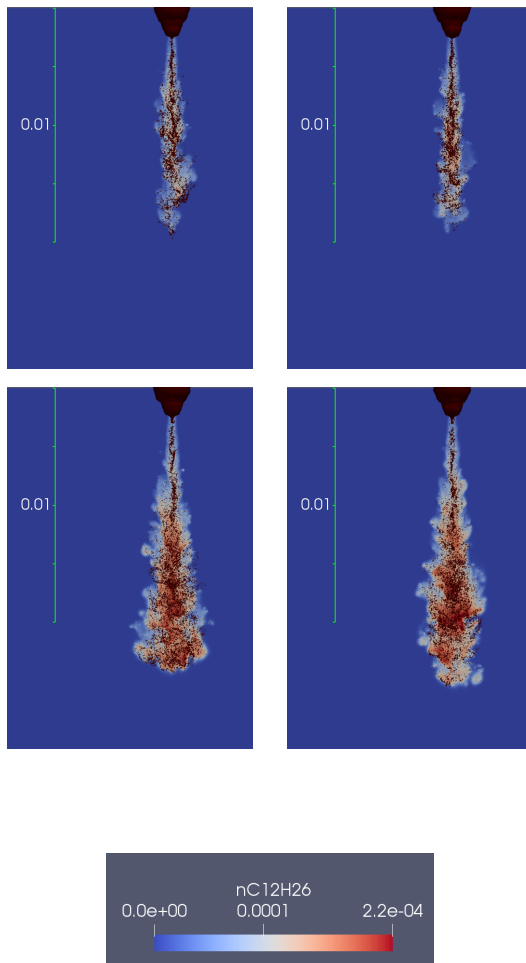


Figure 66 –  $nC_{12}H_{26}$  vapor distribution and parcels - vaporized fuel fraction criterion (left) and  $St_{sgs}$  criterion (right), at 0.05ms and 0.10ms (1<sup>st</sup> and 2<sup>nd</sup> rows respectively).

Performing the same analysis as before for a case with vessel ambient temperature of 900K, Fig. 67 shows a comparison between adaptive mesh refinement criteria. It can be observed that both refinement criteria lead to very similar results for both liquid and vapor length penetrations. Resulting meshes at 0.10ms after start of injection are shown in Fig. 68 and, in Fig. 69 the impact of these two refinement criteria is shown in the vapor phase distri-

bution, spray parcels dispersion, vapor concentration and shape. It is possible to identify that the vaporized fuel fraction criterion is better in capturing the vapor distribution in a perpendicular direction to the fuel spray jet axis, which is evidenced by the wider refined region.

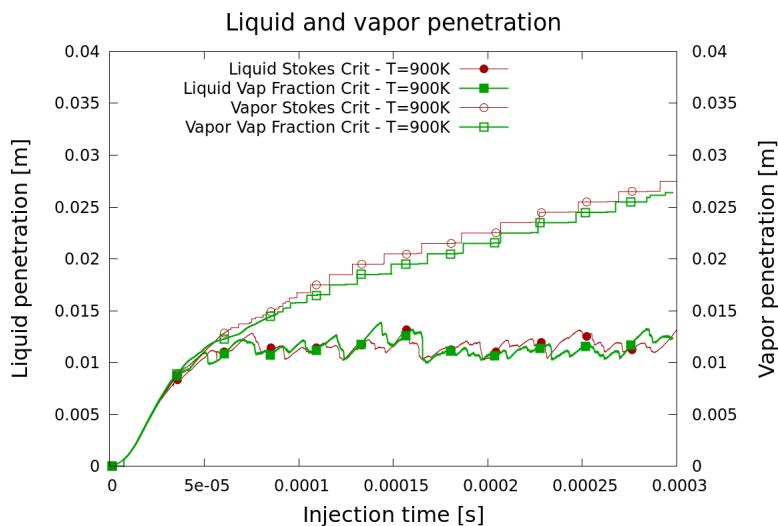


Figure 67 – Refinement criterion impact on liquid length penetration with vessel temperature of 900K.



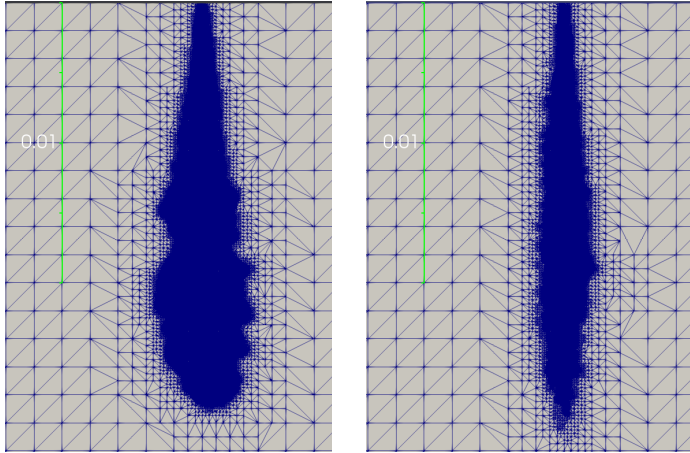


Figure 68 – Resulting mesh with vaporized fuel fraction criterion (left) and  $St_{sgs}$  criterion (right), at 0.10ms with vessel temperature of 900K.

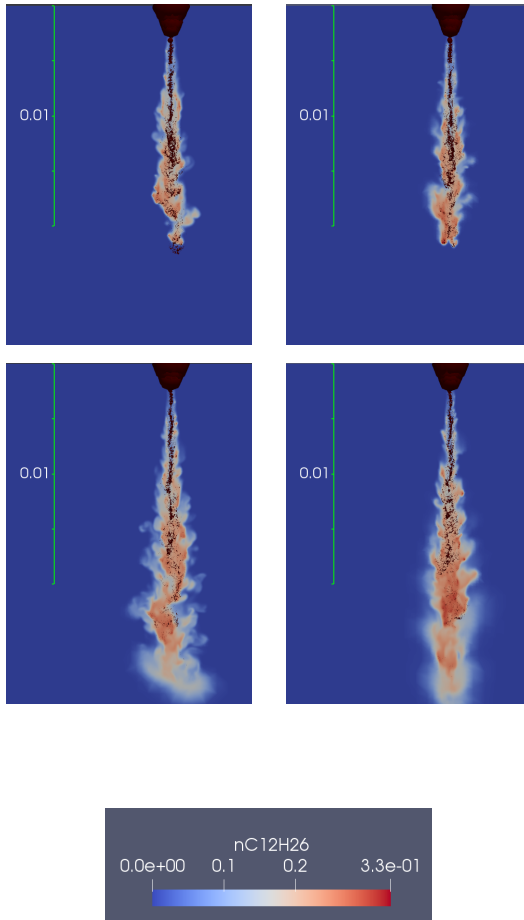


Figure 69 –  $nC_{12}H_{26}$  vapor distribution and parcels - vaporized fuel fraction criterion (left) and  $St_{sgs}$  criterion (right), at 0.05ms and 0.10ms ( $1^{st}$  and  $2^{nd}$  rows respectively) with vessel temperature of 900K.

As a concluding remark from the mesh refinement criterion evaluation, without knowing beforehand the rate of evaporation condition, the best configuration is to have both mesh refinement criteria enabled. With that definition, all the following analyses are run as such.

## 5.2 VESSEL AMBIENT PRESSURE IMPACT

In this section three vessel ambient pressures have been analyzed, 4, 6 and 8MPa, keeping the injection parameters and the vessel ambient temperature constant at  $T = 900K$ . The results will also be used to assess the behavior of empirical correlations for liquid length penetration, spray angle and SMD.

The first correlation, considered to be applicable in a general form to diesel sprays (MARTÍNEZ-MARTÍNEZ et al., 2010), to be evaluated was proposed by Dent (1971), where it related the dominant boundary conditions that affect the spray tip penetration (Fig. 1),

$$S = 3.07 \left( \frac{\Delta p}{\rho_g} \right)^{0.25} (tD)^{0.5} \left( \frac{294}{T_g} \right)^{0.25} \quad (5.1)$$

where  $\Delta p$  is the difference between the injection ( $P_{inj}$ ) to the chamber ( $P_g$ ) pressure,  $\rho_g$  and  $T_g$  are the chamber gas density and temperature, respectively,  $t$  is the injection time and  $D$  is the nozzle hole diameter.

Although Eq. 5.1 can provide an indication about the liquid penetration behavior, it does not capture the proper phenomena, as it fails to capture the ramp and the evolution over time after the main breakup. As shown in Fig. 70, where the empirical correlation was used to calculate spray tip penetration for the case with vessel pressure at 4MPa from table 5, the correlation predicted a lower spray tip penetration and also at a lower rate of penetration length over time.

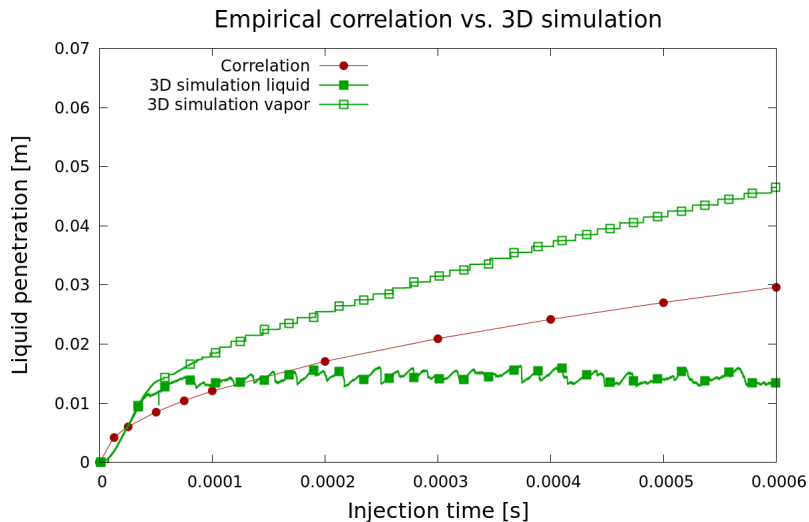


Figure 70 – Spray tip penetration predicted from Eq. 5.1 for the case with vessel ambient pressure of 4MPa, compared to 3D simulation.

An important aspect of the correlation, is that it closely estimates the impact of the pressure when comparing the 3 cases at the same time after SOI. For example, employing the correlation at the time of 0.2ms after SOI, it estimates that an increase in vessel ambient pressure from 4 to 6MPa will lead to a reduction in spray tip penetration of approx. 10% and, a further increase in vessel ambient pressure to 8MPa will lead to a further reduction of approx. 6%. The spray simulation results are different but close where, an increase from 4 to 6MPa in pressure leads to a reduction in spray tip penetration of approx. 12%, and a further increase to 8MPa leads to a further reduction in spray tip penetration of approx. 9%.

Figure 71 presents the simulated results for the cases with varying vessel ambient pressures, and as density increases with increase in vessel ambient pressure, the droplets will suffer a higher drag leading to a faster breakup with smaller size droplets (Tab. 4) and also slower velocities (Fig. 72). These smaller size droplets will have then lower momentum thus will penetrate less inside the chamber.

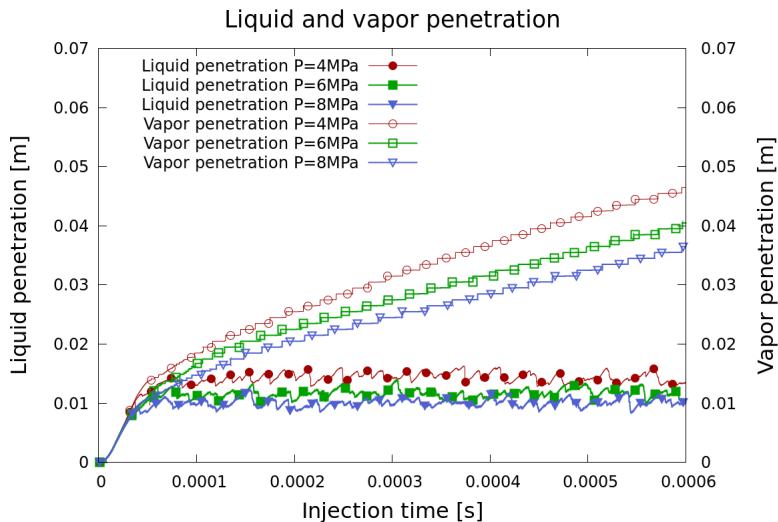


Figure 71 – Vessel pressure impact on liquid and vapor length penetrations.

Table 4 – Sauter Mean Diameter Evaluated at 0.05ms After SOI

| Position below injector tip [mm] | 4MPa | 6MPa | 8MPa |
|----------------------------------|------|------|------|
| 1                                | 67.5 | 68.1 | 69.3 |
| 2                                | 52.5 | 52.2 | 51.7 |
| 3                                | 10.6 | 2.0  | 1.1  |
| 4                                | 1.7  | 1.3  | 1.0  |

The impact on the droplet's velocity can be seen in Fig. 72, where volume average of parcel velocities calculated at 0.05ms after the start of injection comparing the 3 conditions of vessel ambient pressure is presented and, it is possible to see that with increasing vessel ambient pressure, the average velocity of the parcels reduces due to increased drag, as will be described shortly.

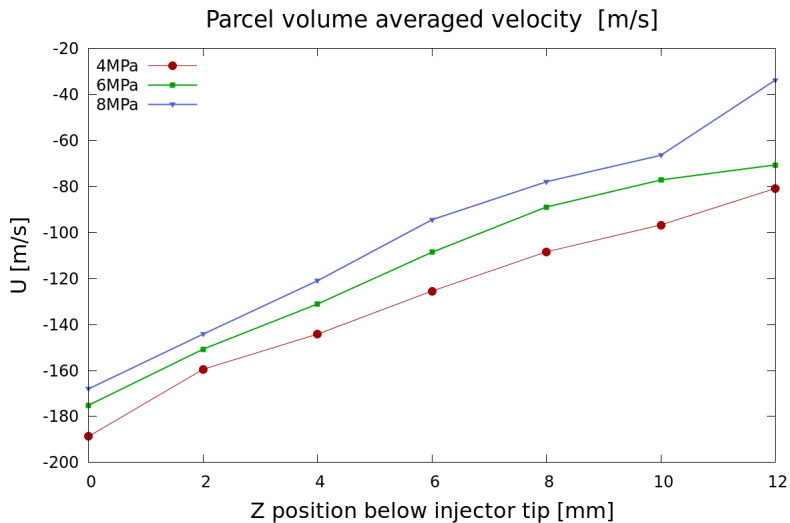


Figure 72 – Volume average of parcel velocity evaluated at different positions below the injector tip.

A 3D view of the spray parcels, with constant size to make visualization easier, and colored by z-component of velocity can be seen in Fig. 73, where it is possible to see qualitatively that as the droplets enter the domain they are affected by drag and have their velocities reduced. The slower droplets are then pushed to the side by the new droplets entering the domain. In the center of the spray, as new droplets enter the domain, they are somewhat shielded by the slower droplets in the periphery of the spray jet.

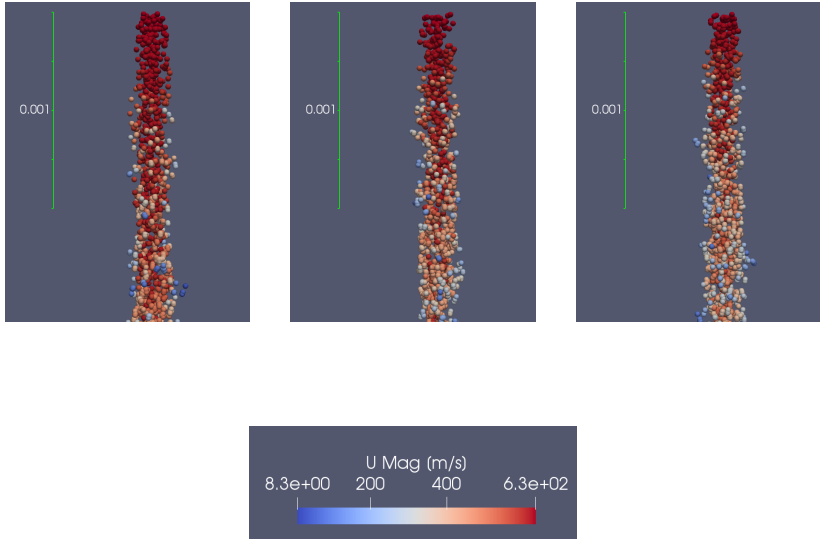


Figure 73 – Droplet velocity magnitude as a consequence of the varying vessel ambient pressure - 4MPa (left), 6MPa (center) and 8MPa (right), at 0.05ms after start of injection.

Analyzing the drag on all the parcels in the domain for the cases with varying vessel ambient pressure, the maximum drag that the parcels are subjected to when going from 4MPa to 6MPa ambient pressure increases by approx. 50% and, a further increase to 8MPa increases the maximum drag that the parcels are subjected to in approx. 32%. Only less than 1% of the parcels in these cases are subjected to a drag of the order  $10^{-3}$  to  $10^{-2}N$ , with more than 99% of the parcels subjected to a drag in the order of  $10^{-4}N$ .

Regarding vapor length penetration, even though it reduces with increased backpressure, the impact does not seem to be as constant along the injection duration as in the liquid length. This can be noticed by the fact that the vapor length in the 4MPa case has a different slope as both 6 and 8MPa curves (Fig. 71).

The vapor mass phase diffusivity for n-Dodecane as a function of temperature at these 3 vessel's ambient pressure is shown in Fig. 74, where it is possible to verify that at  $T = 600K$ , the diffusivity at 4MPa ambient pressure is roughly 50% higher than at 6MPa, which is roughly 30% higher than at 8MPa.

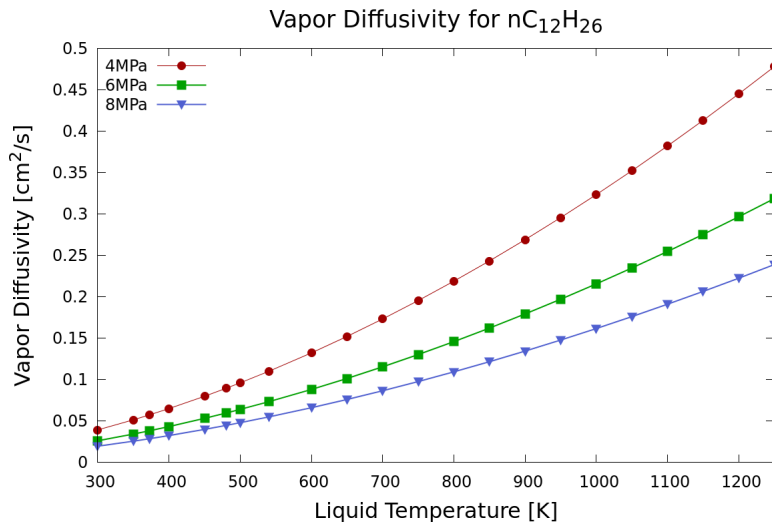


Figure 74 – Vapor mass phase diffusivity for n-Dodecane as a function of temperature.

To verify clearly the impact of the vessel ambient pressure in the vapor phase diffusion, Fig. 75 shows the difference between vapor to liquid length penetration, which is a measure of how much the vapor phase travels from a starting point in the liquid phase position. The difference is roughly equal regardless of vessel ambient pressure, which may lead to the wrong conclusion that the vapor phase diffusion is relatively insensitive to the ambient pressure.



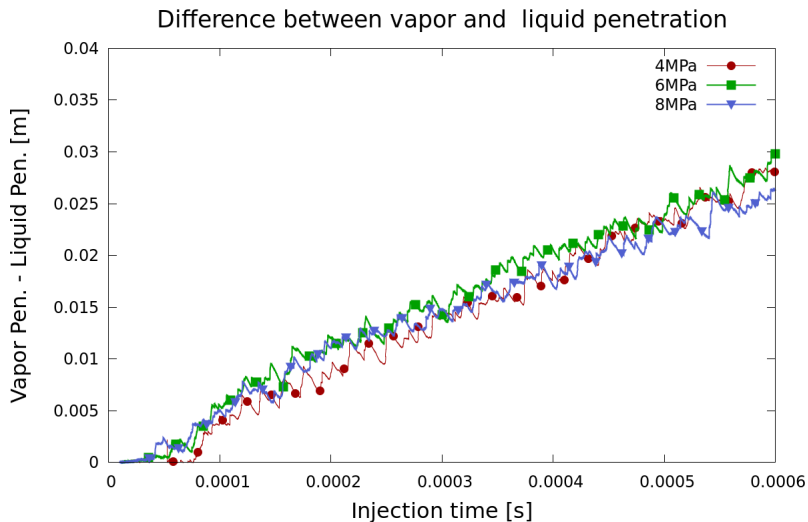


Figure 75 – Vessel pressure impact on liquid and vapor length penetrations.

The reason for the behavior seen in Fig. 75 is related to the droplet breakup process, where as shown in Tab. 4, at lower vessel ambient pressure the breakup is slower, leading to bigger SMD (higher volume to surface area ratio), thus slower evaporation ratio is foreseen.

Figure 76 shows the impact not only on penetration lengths but also on vapor phase distribution, spray parcels dispersion, vapor concentration and shape of the vapor distribution.

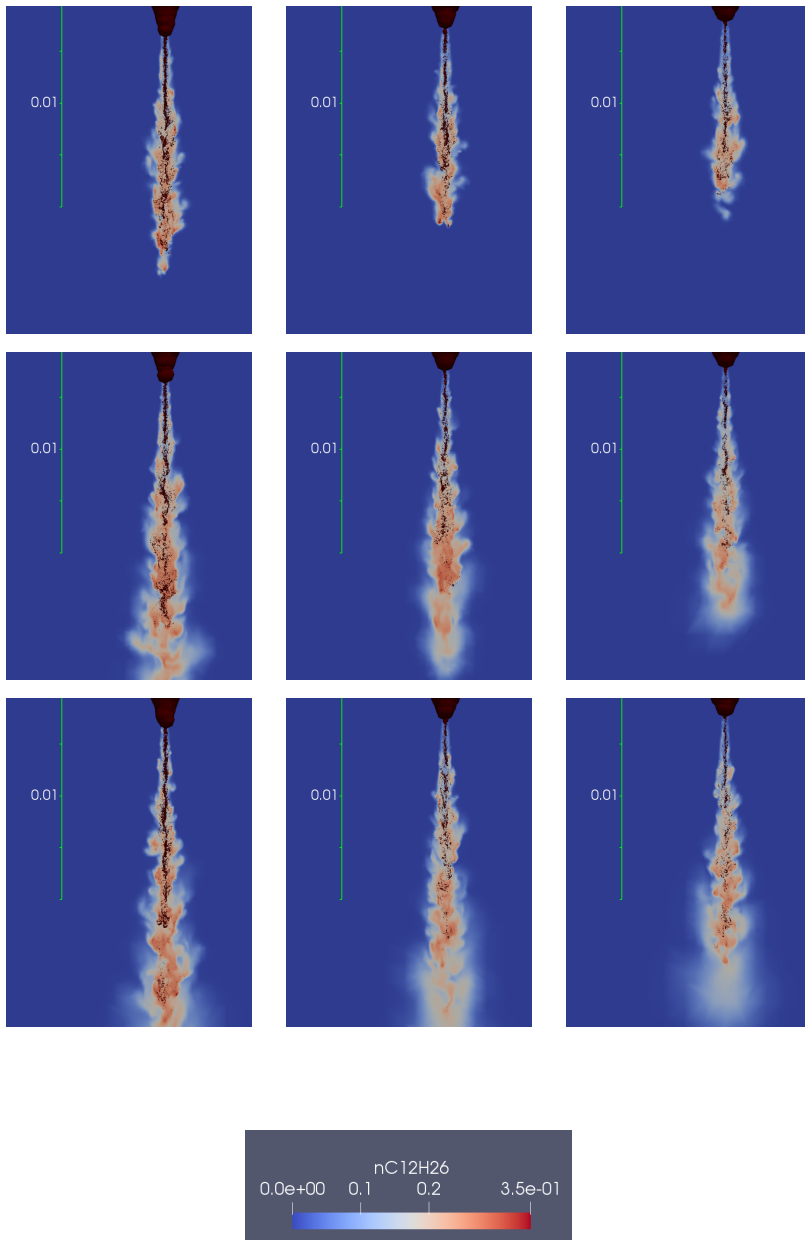


Figure 76 –  $nC_{12}H_{26}$  vapor distribution and parcels - P=4MPa (left), 6MPa (center) and 8MPa (right), at 0.05ms, 0.10ms and 0.15ms (1<sup>st</sup>, 2<sup>nd</sup> and 3<sup>rd</sup> rows respectively).

The second correlation to be evaluated was proposed by Hiroyasu and Arai (1990), where it relates the dominant boundary conditions that affect the spray angle ( $\Phi$ ),

$$\Phi = 83.5 \left( \frac{L}{D} \right)^{-0.22} \left( \frac{D}{D_s} \right)^{0.15} \left( \frac{\rho_g}{\rho_l} \right)^{0.26} \quad (5.2)$$

where  $D_s$  is the sac hole diameter as defined in section 2.1 and  $L$  is the length of the nozzle hole.

With the increase in the vessel ambient pressure, there is an increase in vessel ambient density, and this correlation states that, with the increase in the density ratio ( $\rho_g/\rho_l$ ) between gas and liquid, the spray angle ( $\Phi$ ) increases due to the increased drag on the droplets.

The correlation from Eq. 5.2 also underestimates, roughly by half, the impact of the pressure when comparing the 3 cases. It results that an increase in vessel ambient pressure from 4 to 6MPa will lead to an increase in spray angle of approx. 11% and, a further increase in vessel ambient pressure to 8MPa will lead to a further increase of approx. 7%. The spray simulation results are different, where an increase from 4 to 6MPa in pressure leads to an increase in spray angle of approx. 22%, and a further increase to 8MPa leads to a further increase in spray angle of approx. 14% (Tab. 5). This correlation is also able to indicate the tendency.

As the nozzle hole's length information for the fuel injector was not available at the ECN database, it was not possible to calculate the predicted spray angle by this correlation.

Table 5 – Vessel and Spray Conditions - Pressure Analyses

|                          | 4MPa   | 6MPa   | 8MPa   |
|--------------------------|--------|--------|--------|
| $\rho_{gas} [kg/m^3]$    | 15.0   | 22.7   | 30.0   |
| $U_{inj} [m/s]$          | 664.2  | 664.2  | 664.2  |
| Injection pressure [bar] | 1582.2 | 1602.7 | 1622.2 |
| spray angle [deg]        | 12.2   | 15.0   | 17.2   |

The last correlation to be evaluated in this work, also based on experimental results from Hiroyasu and Arai (1990), is to estimate the resulting *SMD* given by,

$$\frac{SMD}{D} = 0.38 Re^{0.25} We_l^{-0.32} \left( \frac{\mu_l}{\mu_g} \right)^{0.37} \left( \frac{\rho_l}{\rho_g} \right)^{-0.47} \quad (5.3)$$

At first glance, this correlation seems physically incorrect as it states

that with an increase in vessel gas density that the resulting  $SMD$  will increase, as it uses a negative exponent to the density ratio term  $((\rho_l/\rho_g)^{-0.47})$ . It may be valid only in a region of the spray where strong coalescence is happening during the spray injection, where due to an increase in droplet numbers with breakup, and thus increase in the collision probabilities can lead to high coalescence and thus increase in the  $SMD$ .

A concluding remark about the correlations proposed by Dent (1971) and Hiroyasu and Arai (1990) is that they are too specific to the experimental setup that has led them to the proposed expressions, thus some caution from the user is required prior to using them as an initial estimation for the resulting conditions from the spray injection. These correlations have been modified by various researchers along the years, but they are still providing the main relations between parameters that affect the spray tip penetration, angle and  $SMD$ , and their application helps in assessing trend behaviors with ambient pressure variations.

### 5.3 VESSEL AMBIENT TEMPERATURE IMPACT

In this section three vessel ambient temperatures have been analyzed, 600, 900 and 1200K, keeping the ambient vessel pressure at  $P = 6MPa$ , and the injection parameters.

To verify the possibility of applying Eq. 5.1 to these simulated conditions, let's first regroup the terms, and knowing that  $\Delta p = P_{inj} - P_g$ , and that for the same vessel ambient molar species compositions  $P_g/\rho_g = RT_g$ ,

$$\begin{aligned} S &= 3.07(tD)^{0.5} \left( \frac{294\Delta p}{T_g\rho_g} \right)^{0.25} \\ &= 3.07(tD)^{0.5} \left( \frac{294\Delta pR}{P_g} \right)^{0.25}, \end{aligned} \quad (5.4)$$

where  $R$  is the gas constant.

From Eq. 5.4 it is clear that if injection and vessel ambient pressures are kept constant for the various cases, the resulting spray tip penetration will not change, which makes impossible to evaluate the simulated conditions described in this section with this correlation, indicating a limitation.

To assess Eq. 5.1 a set of experimental data from ECN was selected, and the resulting prediction for spray tip penetration is compared against them. The selected experiments from ECN have varying vessel ambient pressure and temperature and, injection pressure, while maintaining the same in-

jector and vessel ambient molar species composition (Figure 77).

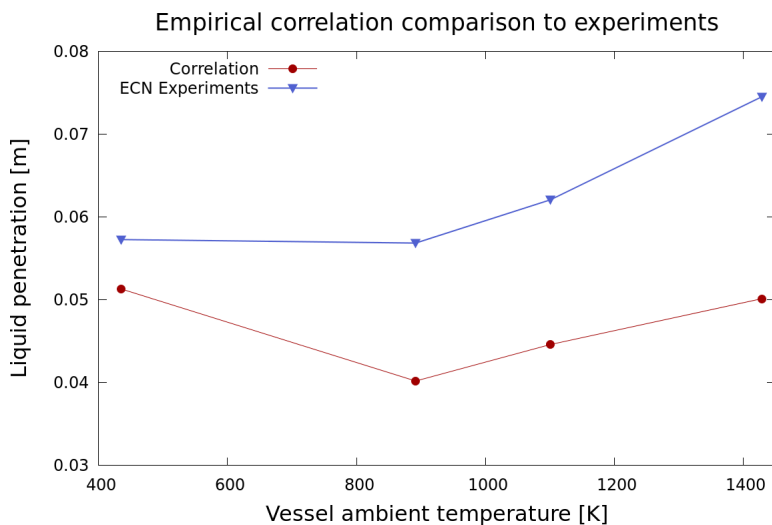


Figure 77 – Spray tip penetration predicted from Eq. 5.1 with varying vessel and injection conditions.

A final comment based on the analyses made on Eq. 5.1 considering their input parameters has shown that it captures the overall spray tip penetration trends, but fails to predict its absolute penetration values with variations in vessel ambient pressure and temperature, under estimating them. It also fails to predict the spray tip penetration in the condition where vessel ambient and injection pressures and, ambient composition are kept constant.

Regarding the empirical correlation for  $SMD$ , expressed by Eq. 5.3, it does not present a direct relation to the vessel ambient temperature. The relation is implicit in the dynamic viscosity and density temperature dependencies for the gas phase.

Simulation results for the three cases are shown in Fig. 78 where, it is possible to see that as the vessel temperature increases the liquid length penetration decreases and the vapor length penetration increases, as initially expected. Going from 600 to 900K, the liquid length penetration reduces almost by half, where an additional temperature increment of 300K, going to 1200K doesn't lead to the same level of impact. The increase in vapor penetration with a higher vessel temperature is not as high as the impact on the liquid length penetration.

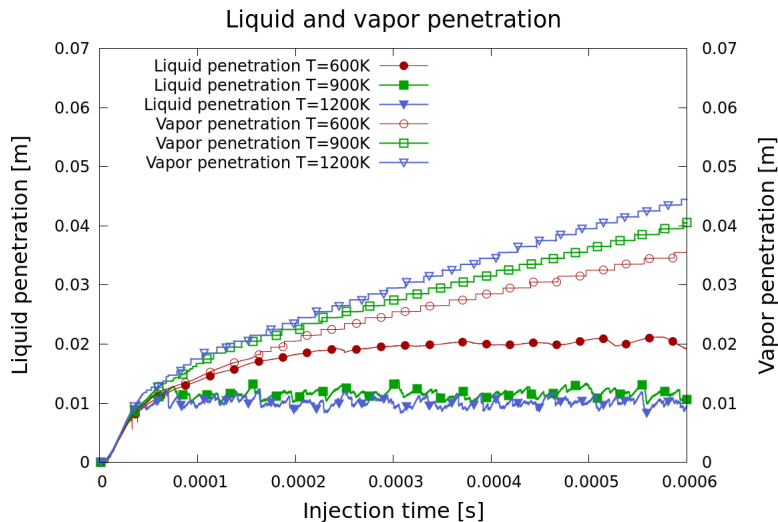


Figure 78 – Vessel temperature impact on liquid and vapor length penetrations.

To verify clearly the impact of the vessel ambient temperature in the vapor phase diffusion, Fig. 79 shows the difference between vapor to liquid length penetrations, which is a measure of how much the vapor phase travels from a starting point in the liquid phase position. The vapor diffusion increases with increasing vessel ambient temperature, but more aggressively with the variation from 600 to 900K, indicating a relatively high sensitivity to the ambient temperature, which can be explained mainly by the vapor mass phase diffusivity (Fig. 74), where it is approx. 65% higher at 1200K than at 900K and it is roughly 100% higher at 900K than at 600K.

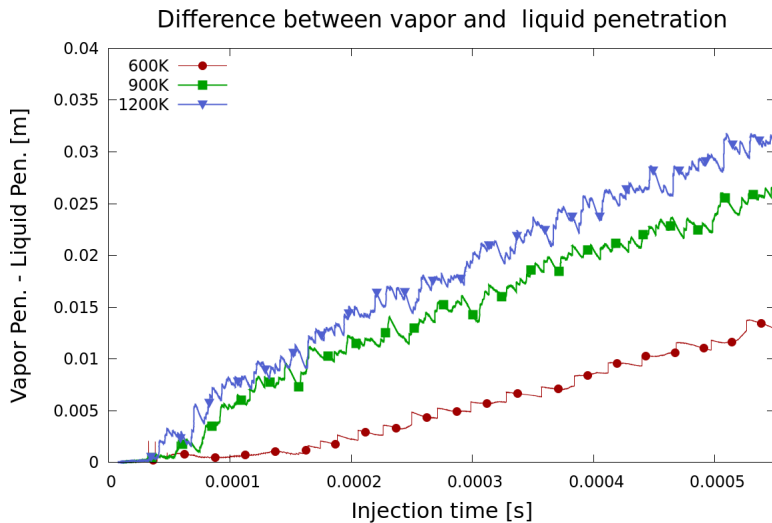


Figure 79 – Vessel pressure impact on liquid and vapor length penetrations.

In Fig. 80 it is possible to see the impact on vapor phase distribution, spray parcels dispersion, vapor concentration and shape for the cases with varying vessel ambient temperature.

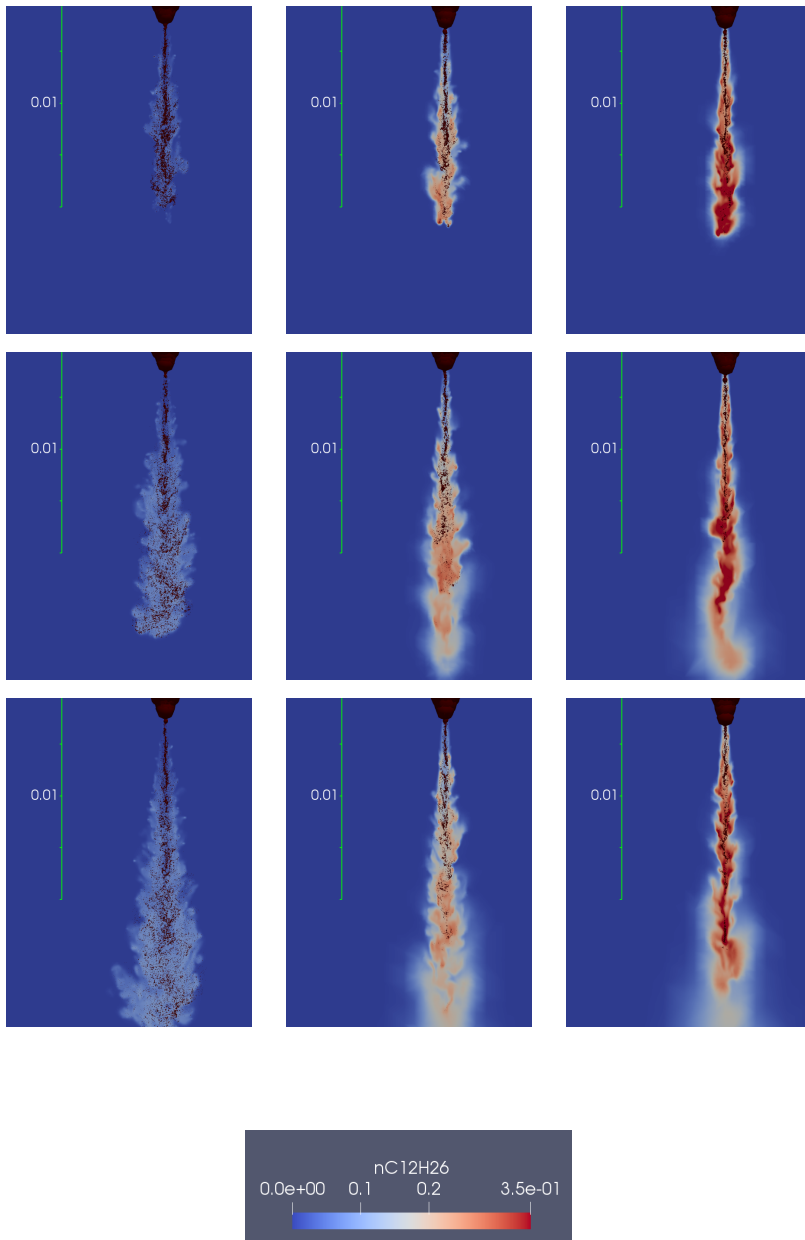


Figure 80 –  $nC_{12}H_{26}$  vapor distribution and parcels -  $T=600K$  (left),  $900K$  (center) and  $1200K$  (right), at  $0.05ms$ ,  $0.10ms$  and  $0.15ms$  ( $1^{st}$ ,  $2^{nd}$  and  $3^{rd}$  rows respectively).



Comparing the 2 cases with similar gas density but, with different conditions for ambient pressure and temperature, helps to understand the dominant factors in liquid length penetration. The first case had ambient  $P = 8\text{MPa}$  and  $T = 900\text{K}$  leading to an ambient gas density of  $30\text{kg}/\text{m}^3$  (Tab. 5) and, the second case had ambient  $P = 6\text{MPa}$  and  $T = 600\text{K}$  leading to an ambient gas density of  $34\text{kg}/\text{m}^3$  (Tab. 6). Comparing these two cases for liquid length penetration, the first case was approx.  $10\text{mm}$  while the second case was approx.  $20\text{mm}$ , while vapor length penetrations were nearly the same (Fig. 81). The SMDs for these cases as shown in Tables 4 and 7, are similar. This indicated that the most relevant factor, in these cases, for liquid length penetration was not the increase in ambient gas density, that would have increased the droplet drag but, the reduction in the evaporation rate due to the lower gas temperature. Regarding vapor phase length the lower evaporation rate together with a lower vapor mass phase diffusivity at  $600\text{K}$  against  $900\text{K}$ , as stated before, explain the results.

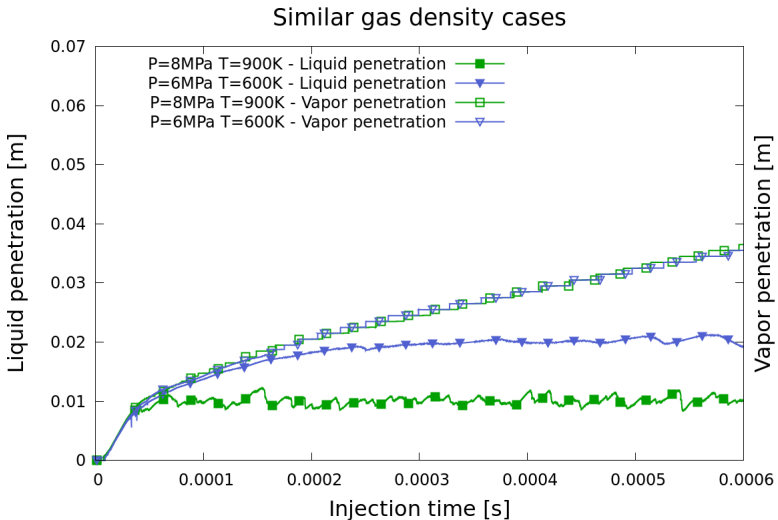


Figure 81 – Liquid and vapor length penetrations comparing cases with similar gas density.

Vessel and spray conditions are,

Table 6 – Vessel and Spray Conditions - Temperature Analyses

|                          | 600K   | 900K   | 1200K  |
|--------------------------|--------|--------|--------|
| $\rho_{gas}[kg/m^3]$     | 34.0   | 22.7   | 17.0   |
| $U_{inj}[m/s]$           | 664.2  | 664.2  | 664.2  |
| Injection pressure [bar] | 1602.7 | 1602.7 | 1602.7 |
| spray angle [deg]        | 18.3   | 15.0   | 13.0   |

With the increase in vessel ambient temperature from 600K up to 1200K, the heating up of the droplets' surface is faster with increased heat transfer rate, thus the n-Dodecane boiling temperature ( $T_{boil}^{nDodecane} = 489.3K$ ) is reached faster and the evaporation starts sooner in time as compared to the 600K gas temperature condition. So the smaller droplets will reduce their size faster and, as a consequence the SMD will be biased by the bigger droplets, which explains the slight increase in SMD (Tab. 7) with increasing vessel ambient temperature.

Table 7 – Sauter Mean Diameter Evaluated at 0.05ms After SOI

| Position below injector tip [mm] | 600K | 900K | 1200K |
|----------------------------------|------|------|-------|
| 1                                | 68.6 | 68.1 | 68.2  |
| 2                                | 49.4 | 52.2 | 54.9  |
| 3                                | 1.3  | 2.0  | 2.1   |
| 4                                | 1.2  | 1.3  | 1.5   |

#### 5.4 COMPARISON BETWEEN nDODECANE ( $nC_{12}H_{26}$ ) VS. nHEPTANE ( $nC_7H_{16}$ )

Diesel fuels are a blend of different hydrocarbon compounds with a wide range of lengths, which turns evaporation and combustion modeling a difficult task. They also present complex reaction kinetics (GALLE; SEBASTIAN, 2013). In order to make Diesel fuel CFD simulations feasible, development of surrogate fuels are required, that can either be a single component or a mixture of them, presenting chemical and physical characteristics that are similar to the real fuel.

Based on that, both  $nC_{12}H_{26}$  (n-Dodecane) and  $nC_7H_{16}$  (n-Heptane) have been used frequently as single component surrogates for Diesel fuel in internal combustion engines' simulations. In a direct comparison between these two single component surrogates,  $nC_7H_{16}$  (n-Heptane) has a compara-

ble cetane number with Diesel, although due to its higher volatility, in mixing-controlled combustion it will present a different ignition delay to Diesel fuel (FARRELL et al., 2007). On the other hand,  $nC_{12}H_{26}$  (n-Dodecane) presents a liquid density closer to average Diesel fuel, thus better representing the liquid to gas density ratio (GALLE; SEBASTIAN, 2013), and presents similar high boiling temperature characteristics to Diesel (PITZ; MUELLER, 2011). These two single component fuels also have known chemistry and available kinetic mechanisms, covering low to high temperature combustion range.

This section will then present a comparison between  $nC_{12}H_{26}$  (n-Dodecane) and  $nC_7H_{16}$  (n-Heptane) concerning liquid and vapor length penetrations describing some important differences related to their specific physical properties. Combustion of these fuels will not be covered.

Vessel conditions, injected mass and injection flow rate for both cases are the same, so differences in liquid and vapor length penetrations are only function of their specific fuel properties.

The first difference appears in the fuel injection velocity as the Blobs' injection velocity  $U_{inj}$  can be approximated by,

$$U_{inj} = \frac{\dot{m}_{inj}}{A_{hole}\rho_l} \quad (5.5)$$

so for the same injected mass flow rate ( $\dot{m}_{inj}$ ), the same nozzle hole cross-section area ( $A_{hole}$ ), with the injection velocity inversely proportional to the liquid fuel density, this leads to an increase in the velocity of the injected Blobs with n-Heptane of approx. 12% when comparing to the n-Dodecane. This increase in the Blob's injected velocity for n-Heptane also leads to an increase in the spray cone angle in approx. 6% (Tab. 8).

The resulting values for the spray characteristics at the fuel injection temperature ( $T = 373K$ ) are,

Table 8 – Vessel and Spray Conditions - Fuel Type Analyses

|                      | $nC_{12}H_{26}$ | $nC_7H_{16}$ |
|----------------------|-----------------|--------------|
| $\rho_l [kg/m^3]$    | 690.7           | 613.2        |
| $\sigma [N/m]$       | 0.018           | 0.012        |
| $\mu_l [mPa.s]$      | 0.60            | 0.30         |
| vapor pressure [kPa] | 2.0             | 105.7        |
| $U_{inj} [m/s]$      | 664             | 748          |
| spray angle [deg]    | 15              | 15.9         |

The vapor pressure for n-Heptane is much higher than for n-Dodecane at the fuel injection temperature, as shown in Tab. 8. As described in Pol-

ing et al. (2001), applying the Antoine (1888) correlation in their validated temperature intervals and comparing both single component fuels, it is evident the higher volatility of n-Heptane at lower temperatures (Fig. 82), which indicates that the n-Heptane liquid jet will evaporate faster.

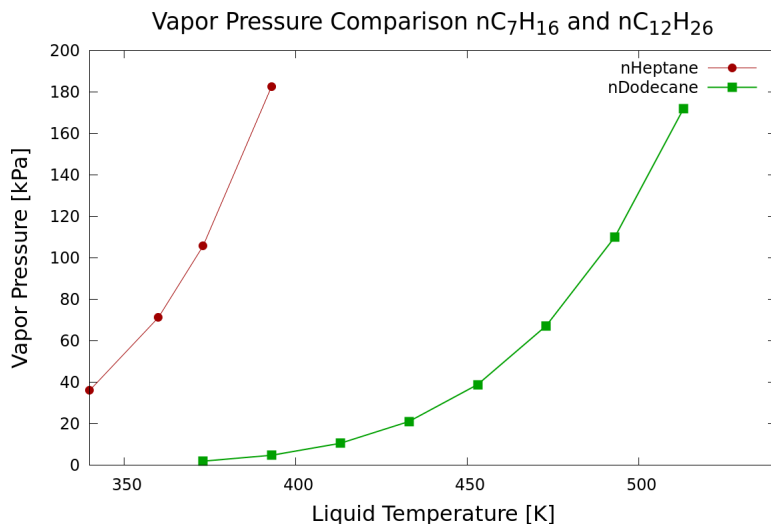


Figure 82 – Vapor pressure comparison between  $nC_7H_{16}$  and  $nC_{12}H_{26}$ .

Calculating for both n-Heptane and n-Dodecane, as a function of liquid temperature, the liquid surface tension (Fig. 83) based on NIST (the NIST Standard Reference Data.) functions, and the dynamic viscosity (Fig. 84), applying the correlation from Lucas (1981), as described in Poling et al. (2001), it is clear that regardless of temperature n-Dodecane presents higher surface tension and dynamic viscosity than n-Heptane.

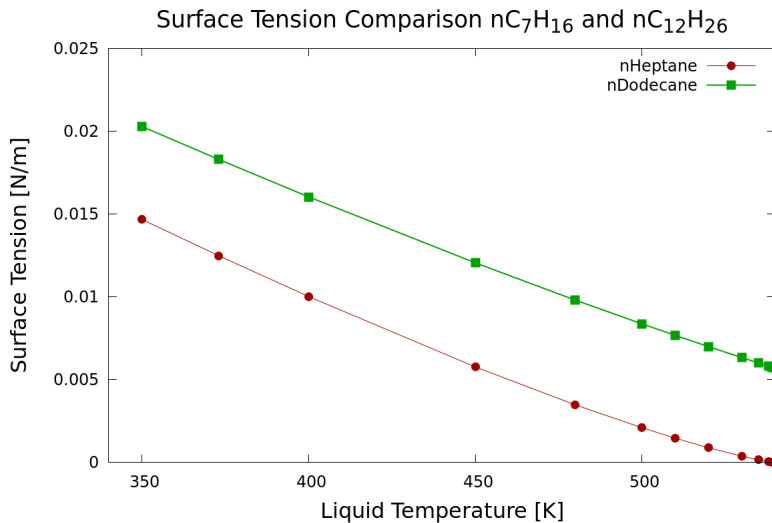


Figure 83 – Surface tension comparison between  $nC_7H_{16}$  and  $nC_{12}H_{26}$ .

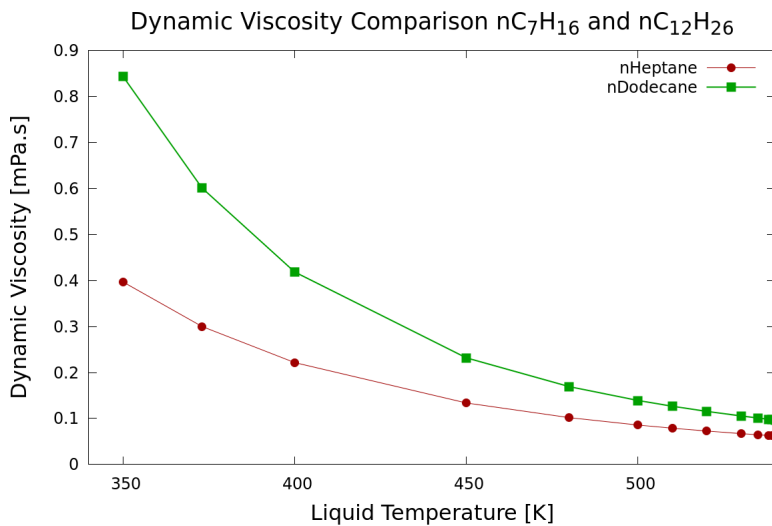


Figure 84 – Dynamic viscosity comparison between  $nC_7H_{16}$  and  $nC_{12}H_{26}$ .

These fuel properties impact directly in the relation between the vis-

cous forces to the inertia and surface tension forces in the droplet, the Ohnesorge number ( $Z_l = \sqrt{We_l}/Re_l$ ). If assumed same droplet radius and relative velocity for both fuels, just to make understanding of the impacts clear, the ratio between liquid fuel density to surface tension impacts on the liquid Weber number ( $We_l = \rho_l r_0 u_{rel}^2 / \sigma$ ) and, the ratio between liquid fuel dynamic viscosity to density impacts on the liquid Reynolds number ( $Re_l = r_0 u_{rel} / \nu_l$ ). So as a consequence, the ratio between the liquid Weber to Reynolds numbers (the Ohnesorge number) is affected. A direct analysis of the ratio between the Ohnesorge numbers for  $nC_{12}H_{26}$  to  $nC_7H_{16}$  with varying liquid fuel temperatures is shown in Fig. 85. As can be seen, at the injection temperature the Ohnesorge number for  $nC_{12}H_{26}$  is approx. 1.5 times higher than the number for  $nC_7H_{16}$ , decreasing steadily with increasing droplet fuel temperature, thus showing a high influence of the viscosity in favor of the  $nC_{12}H_{26}$ .

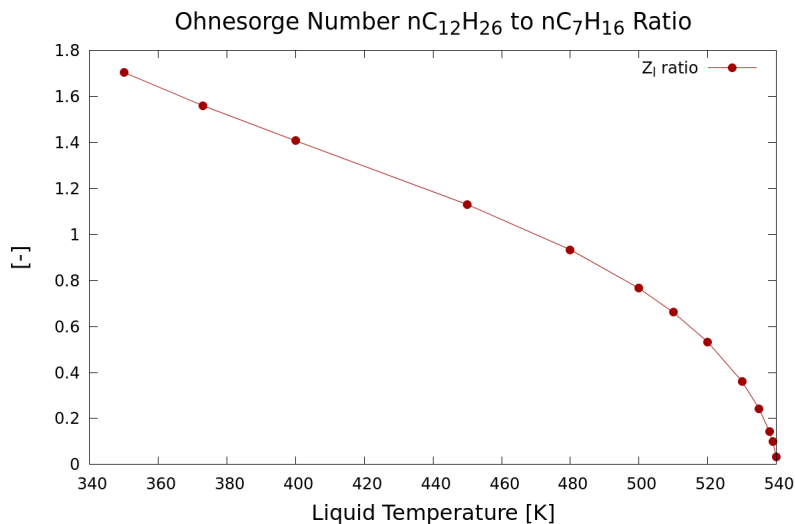


Figure 85 – Ohnesorge number ratio comparison between  $nC_{12}H_{26}$  to  $nC_7H_{16}$ .

An analysis of the effect of liquid viscosity on droplet breakup was presented by Bergeles et al. (2017), where it was concluded that a higher liquid dynamic viscosity will help to reduce the deformation in the droplet due to aerodynamic forces. So for n-Heptane with a lower dynamic viscosity the droplets will present higher and faster deformations and, faster accelerations.

The lower liquid surface tension of n-Heptane will also lead to a higher

gas Weber number ( $We_g = \rho_g r_0 u_{rel}^2 / \sigma$ ), still assuming same droplet radius and relative velocity for both fuels, which indicates that the aerodynamic forces are more significant and, the surface tension is less effective in balancing the surface deformations in the droplet. Figure 86 shows a ratio comparison between the gas Weber numbers of  $nC_7H_{16}$  to  $nC_{12}H_{26}$  with varying liquid fuel temperature. As can be seen, at the injection temperature the gas Weber number for  $nC_7H_{16}$  is approx. 1.4 times higher than the number for  $nC_{12}H_{26}$ , which indicates a more aggressive type of droplet's breakup. With increasing liquid droplet temperature this ratio increases further, continuing to favor a more rapid breakup for the  $nC_7H_{16}$  fuel jet.

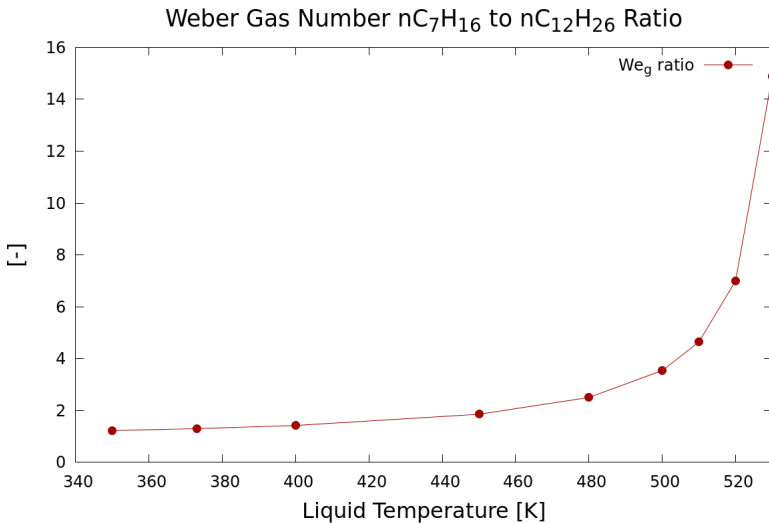


Figure 86 – Gas Weber number ratio comparison between  $nC_7H_{16}$  to  $nC_{12}H_{26}$ .

So from a droplet size perspective it is expected for n-Heptane that, as a consequence of the lower liquid dynamic viscosity and lower surface tension, it will present a faster breakup of the droplets. Due to its lower boiling temperature compared to n-Dodecane ( $T_{boil}^{nHeptane} = 371.5K$ ) so higher vapor pressure at lower temperatures, it is expected that the rate of vaporization will be higher with n-Heptane than with n-Dodecane. Also with a faster evaporation for n-Heptane, the smaller droplets will reduce their size faster and, as a consequence the SMD will be biased by the bigger droplets. These combined effects can be seen in the resulting SMD from the simulation (3D sim) pre-

sented in Tab. 9, showing higher SMD values for the n-Heptane case and, in Fig. 90 showing lower liquid length penetration for n-Heptane. In the same table, for reference only, the SMD obtained applying the empirical correlation Eq. 5.3 (Correl.) is presented, clearly indicating that it underpredicts the SMD.

Table 9 – SMD Evaluated at  $0.05ms$  After SOI for Both Fuels

| Position below<br>injector tip [mm] | $nC_7H_{16}$ |         | $nC_{12}H_{26}$ |         |
|-------------------------------------|--------------|---------|-----------------|---------|
|                                     | 3D sim.      | Correl. | 3D sim.         | Correl. |
| 2                                   | 70.0         | 12.9    | 68.1            | 10.5    |
| 4                                   | 14.9         | 2.4     | 1.8             | 1.6     |
| 6                                   | 0.9          | 0.5     | 1.2             | 0.3     |

The impact on the droplet's velocity is shown in Fig. 87, where volume average of parcel velocities calculated at  $0.05ms$  after the start of injection comparing both fuels is presented and, it is possible to see that the average velocity of the parcels is higher with  $nC_7H_{16}$  along the whole spray length.

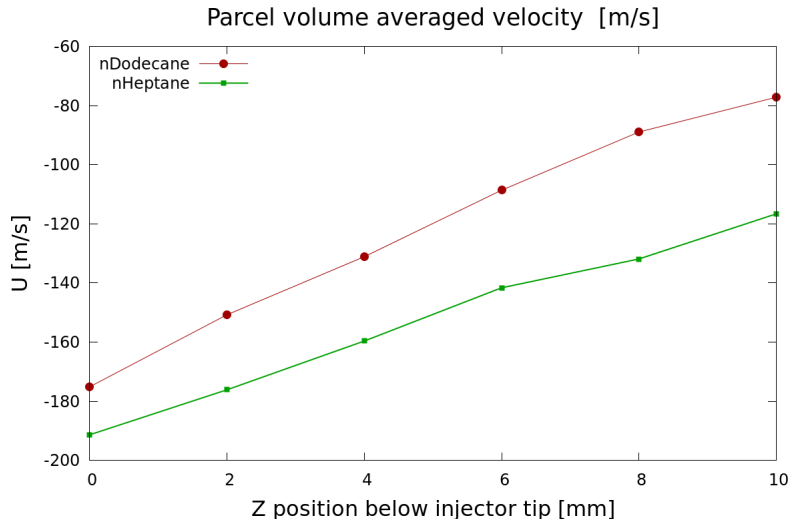


Figure 87 – Volume average of parcel Velocity evaluated at different positions below the injector tip.

A 3D view of the spray parcels, with constant size to make visualiza-



tion easier, and colored with z-component of velocity and droplet drag can be seen in Figures 88 and 89, respectively, where it is also possible to see qualitatively higher velocity and drag for  $nC_7H_{16}$ .

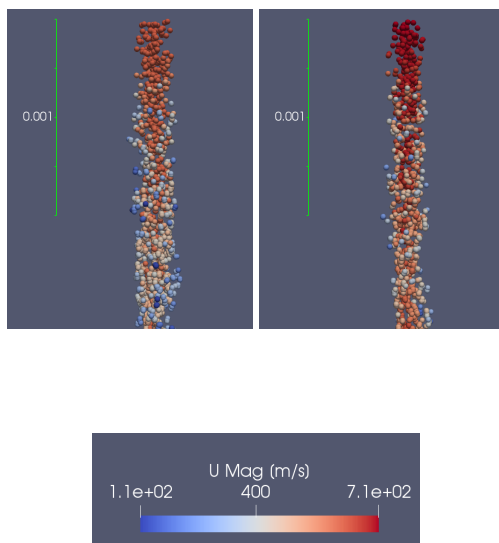


Figure 88 – Droplet velocity magnitude  $nC_{12}H_{26}$  (left) and  $nC_7H_{16}$  (right), at 0.05ms after start of injection.

Analyzing the drag on all the parcels in the domain for the cases with different fuel properties, the maximum drag that the parcels are subjected to with n-Heptane is approx. 27% higher than for n-Dodecane. Only just a little more than 1% of the n-Heptane parcels and, just a little less than 1% of the n-Dodecane parcels are subjected to a drag of the order  $10^{-3}$  to  $10^{-2}N$  and, roughly 99% of the parcels are subjected to a drag in the order of  $10^{-4}N$ .

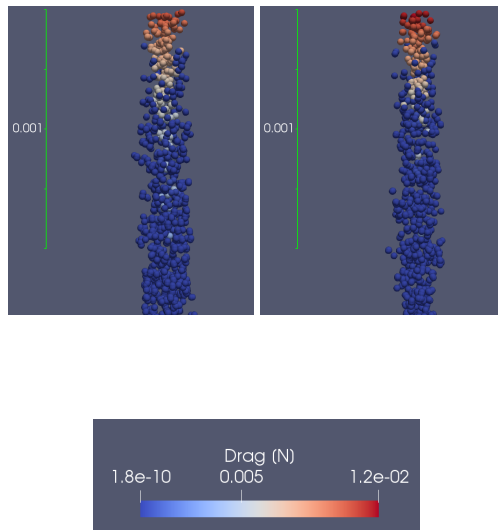


Figure 89 – Droplet drag  $nC_{12}H_{26}$  (left) and  $nC_7H_{16}$  (right) fuel sprays, at 0.05ms after start of injection.

As already discussed previously the increase in the injection velocity leads to a faster breakup of the droplets, which can be seen in Fig. 90 where, in the simulated condition, liquid length penetration with  $nC_7H_{16}$  is roughly 20% lower than with  $nC_{12}H_{26}$ . Taking in consideration this fact alone, if proper attention when in use for internal combustion engine simulations is not taken, it will have a significant impact as wall wetting may not be correctly captured.

In what concerns vapor length penetration from the observation of Fig. 90, they are nearly equal, on the other hand, as can be seen in Fig. 91, the vapor phase distribution is significantly different between both fuels due to the higher volatility of the n-Heptane. This difference can also be extremely relevant to the combustion process, impacting both ignition delay and flame lift-off length.

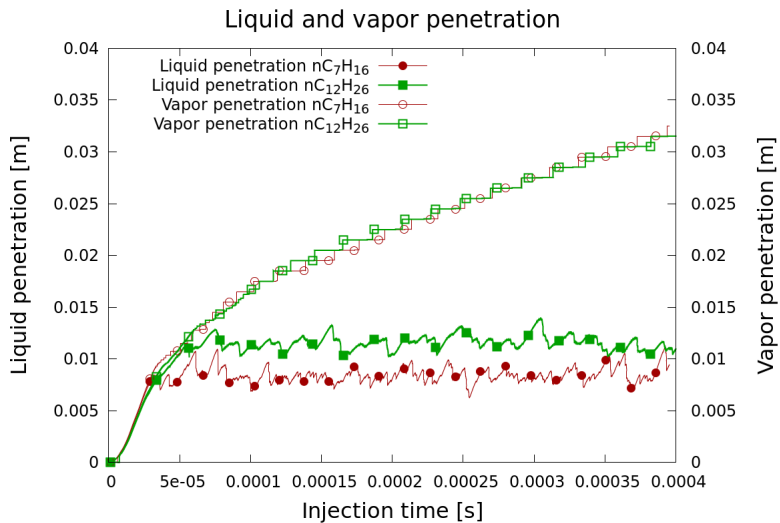


Figure 90 – Comparison between  $nC_{12}H_{26}$  and  $nC_7H_{16}$  on liquid and vapor length penetrations.

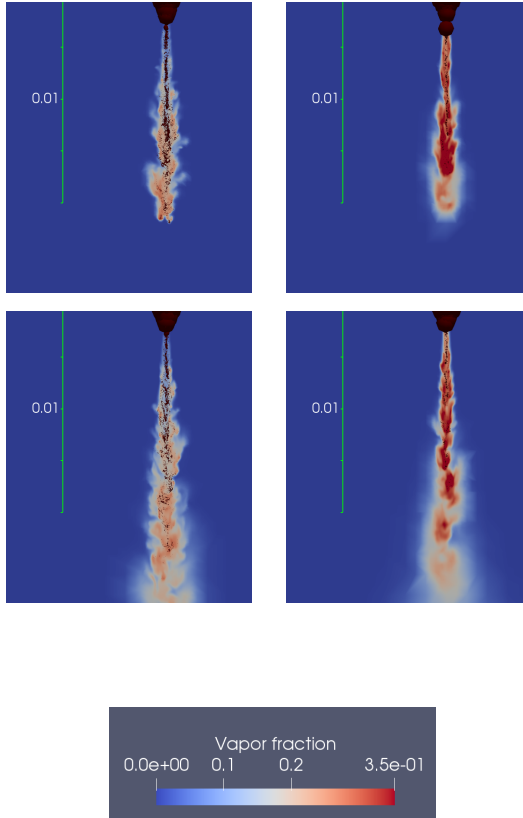


Figure 91 –  $nC_{12}H_{26}$  vapor distribution (left) and  $nC_7H_{16}$  (right), at 0.05ms and 0.15ms (1<sup>st</sup> and 2<sup>nd</sup> rows respectively).

## 6 SUMMARY AND CONCLUSIONS

In this work a Lagrangian spray based solver was implemented in OpenFOAM 2.0.x to analyze turbulent, non-reacting fuel spray injection. The turbulence structure was modeled using LES approach. The model uses adaptive mesh refinement, based on the flow physics, to improve the result's quality without excessive CPU consumption. A new mesh refinement criterion based on the droplet Stokes number was proposed and implemented. The solver was validated against experimental spray data, provided by the Combustion Laboratory at SANDIA (US), simulating the conditions prevailing in the constant volume non-reacting chamber.

In this work it is shown that, with LES modeling of evaporating sprays using adequate sub-models and correct level of mesh refinement, mesh independence can be reached without any additional tuning of breakup parameters or length penetration criteria, as verified in some works presented in the literature. Furthermore, the results are improved as mesh is refined, with no need of setting a specific mesh size to obtain optimal results, as stated in the "mesh convergence" concept in the literature. This fact is of fundamental importance, as it fulfills the very basic consistency concept in numerical models.

It is also shown that STD models are needed to improve the length penetrations' predictions but, in the context of LES models, where STD only takes into account the sub-grid dispersion, an adequate mesh refinement is necessary to achieve correct predictions, even including these models. In addition, an analysis is presented, considering the subgrid Stokes number, showing that there is a mesh size that would include the effect of turbulent dispersion on droplets, considering only resolved scales, and no STD model will be needed. However, in current simulations, these mesh sizes could still be prohibitive to perform parametric analyses, for instance. The proposed criterion presented in this work, based on subgrid Stokes number, was also successfully used as adaptive mesh refinement criterion.

In cases with reduced rate of evaporation where the liquid phase could penetrate further than the vapor phase, the usage of only vaporized fuel fraction as the refinement criterion could fail to properly characterize the liquid length penetration. In that scenario the droplet Stokes number based on the liquid phase could be a more adequate parameter for adaptive mesh refinement. In cases where the evaporation rate is high, the vaporized fuel fraction criterion can characterize the liquid length penetration with good enough accuracy, while better capturing the vapor phase diffusion in a direction perpendicular to the fuel spray jet axis. Therefore in order to improve accuracy and properly characterize both liquid and vapor length penetrations, without

knowing beforehand about the rate of evaporation, it is recommended to use both the droplet Stokes number and the vaporized fuel fraction as refinement criteria.

Regarding the injected number of parcels in order to assure good statistical representation of the Lagrangian phase, in the scenarios simulated in this thesis, assuming a minimum ratio of 130k to 150k *parcels/mg* of injected fuel mass, it is shown that this parameter has not much influence on results.

Reynolds Averaged Navier Stokes approach when compared to Large Eddy Simulation approach for turbulence, even for the same mesh and keeping constant all other vessel conditions and spray parameters, presented significantly different results for liquid length penetration, and even with better results for RANS concerning vapor length penetration, the resulting vapor phase distribution with RANS seemed less realistic, contrary to LES.

The empirical correlation for spray tip penetration proposed by Dent (1971) does not capture correctly the impact of vessel ambient pressure and temperature. Also, if injection and vessel ambient pressures are kept constant, i.e., only varying temperature and as a direct consequence the gas density, the resulting spray tip penetration will not change.

The empirical correlation for spray angle proposed by Hiroyasu and Arai (1990) underestimates the impact of pressure, although captures the tendency with increasing gas density.

The empirical correlation for Sauter Mean Diameter (SMD) proposed by Hiroyasu and Arai (1990) over estimates the impact on the liquid and gas physical properties, resulting in smaller SMDs.

A concluding remark about the correlations proposed by Dent (1971) and Hiroyasu and Arai (1990) is that they are too specific to the experimental setup that has led them to the proposed expressions, thus some caution from the user is required prior to using them as an initial estimation for the resulting conditions from the spray injection. These correlations have been modified by various researchers along the years, but they are still providing the main relations between parameters that affect the spray tip penetration, angle and SMD, and their application helps in assessing trend behaviors with ambient pressure variations.

In the sensitivity analysis with n-Dodecane, the increase in vessel ambient pressure reduces liquid length penetration due to the increase in the drag that the droplet's are subjected to, as a consequence of the increase in vessel ambient density. Vapor length penetration reduces with reduction in pressure, due to slower breakup and bigger SMDs, leading to slower evaporation rates.

In the sensitivity analysis for n-Dodecane, the increase in vessel ambient temperature reduces more liquid length penetration up to a temperature of 900K, then the impact is reduced. This effect is due to its vapor mass phase

diffusivity sensitivity with temperature. Directly related to that, vapor length penetration increases with increasing vessel ambient temperature.

In the comparison between n-Heptane and n-Dodecane, as a consequence of n-Heptane's lower liquid density, as vessel conditions and spray injection profile are kept the same as for n-Dodecane, it results in a higher injected spray velocity. Due to lower dynamic viscosity, the surface instabilities in the n-Heptane droplet due to aerodynamic interaction are less damped and thus increase faster. These factors combined lead to a faster breakup and a shorter liquid length penetration for n-Heptane when compared to n-Dodecane. Due to its higher vapor pressure, n-Heptane is more volatile and thus vaporizes faster than n-Dodecane. This leads to significant differences in vapor phase distribution. This raises same awareness to the usage of these fuels as Diesel surrogates for numerical simulation, without taking these effects into consideration.

A future work following this thesis has to include reacting cases. From a combustion perspective, first and second-stage combustions characterizations are challenging. The first-stage, premixed combustion, will identify the ignition delay, while the second stage, diffusion combustion, will identify the steady lift-of-length, usually by steady OH chemiluminescence data analysis. These stages also differ between High Temperature Combustion (HTC) and Low Temperature Combustion (LTC). The simulation error in ignition delay increases on the LTC case compared to the HTC case. These have been investigated in the ECN looking at various modeling approaches and various chemical kinetics mechanisms (LUO et al., 2014; WANG et al., 2014; NARAYANASWAMY; PEPIOT; PITSCH, 2014; PEI et al., 2015; FRAS-SOLDATI et al., 2015) and, the conclusions have shown that the ignition delay is dependent on the chemical mechanism used, while the flame lift-of-length is less dependent (HAWKES, 2015). The chemical mechanism from Luo et al. (2014) was considered as the baseline for all the analysis from the ECN group up to the 3<sup>rd</sup> ECN workshop. In the 2015 workshop (4<sup>th</sup>), it was recommended to identify a new chemical mechanism to replace the baseline, with the reasons that the baseline was over predicting both ignition delay and flame lift-of-length (HAWKES, 2015).





## BIBLIOGRAPHY

- AMSDEN, A. A.; OROURKE, P. J.; BUTLER, T. D. **KIVA-2: A computer program for chemically reactive flows with sprays.** Washington, DC: NASA STI/Recon, 1989. p. 27975, 1989. (Technical Report n. 89).
- ANTOINE, C. Thermodynamic vapor pressures: New relation between the pressures and the temperatures (thermodynamique, tensions des vapeurs: Nouvelle relation entre les tensions et les temperatures). **CR Hebd. Seances Acad. Sci**, v. 107, n. 681, p. 836, 1888.
- ARCOUMANIS, C.; GAVAISES, M.; FRENCH, B. **Effect of fuel injection process on the structure of diesel sprays.** Warrendale, PA: Society of Automotive Engineers, 1997. (SAE Technical Paper 970799).
- BANERJEE, S.; RUTLAND, C. J. Study on spray induced turbulence using large eddy simulations. **Atomization and Sprays**, Begel House Inc., v. 25, n. 4, p. 285–316, 2015.
- BAUMGARTEN, C. **Mixture formation in internal combustion engines.** Wien: Springer Verlag, 2006.
- BERGELES, K. et al. Effect of liquid viscosity on the aerodynamic breakup of non-spherical droplets. In: **ILASS Europe - 28<sup>th</sup> Conference on Liquid Atomization and Spray Systems.** [S.l.: s.n.], 2017.
- BHARADWAJ, N.; RUTLAND, C. Droplet-ambient sub-grid interaction modeling in large eddy simulation of diesel sprays. In: **ILASS Americas - 22<sup>nd</sup> Annual Conference on Liquid Atomization and Spray Systems.** [S.l.: s.n.], 2010.
- BHARADWAJ, N.; RUTLAND, C.; CHANG, S.-M. Large eddy simulation modelling of spray-induced turbulence effects. **International Journal of Engine Research**, SAGE Publications, v. 10, n. 2, p. 97–119, 2009.
- BOIVIN, M.; SIMONIN, O.; SQUIRES, K. D. On the prediction of gas–solid flows with two-way coupling using large eddy simulation. **Physics of Fluids**, AIP, v. 12, n. 8, p. 2080–2090, 2000.

CASTANHEIRA, É. G.; FREIRE, F. Greenhouse gas assessment of soybean production: implications of land use change and different cultivation systems. **Journal of Cleaner Production**, Elsevier, v. 54, p. 49–60, 2013.

CROWE, C.; CHUNG, J.; TROUTT, T. Particle mixing in free shear flows. **Progress in energy and combustion science**, Elsevier, v. 14, n. 3, p. 171–194, 1988.

DENT, J. **A basis for the comparison of various experimental methods for studying spray penetration**. [S.l.], 1971. SAE Technical Paper 710571.

DUKOWICZ, J. K. A particle-fluid numerical model for liquid sprays. **Journal of computational physics**, Elsevier, v. 35, n. 2, p. 229–253, 1980.

ECHEKKI, T.; MASTORAKOS, E. **Turbulent Combustion Modeling**. London: Springer, 2011.

ECN. **Engine Combustion Network**. Sandia National Laboratories, <http://www.ca.sandia.gov/ecn>.

ELMTOFT, E. et al. **Injected Droplet Size Effects on Diesel Spray Results with RANS and LES Turbulence Models**. Warrendale, PA: Society of Automotive Engineers, 2015. (SAE Technical Paper 2015-01-0925).

EPA, U. S. E. P. A. **A Comprehensive Analysis of Biodiesel Impacts on Exhaust Emissions**. [S.l.], 2002. EPA 420-P-02-001.

FARRELL, J. et al. **Development of an experimental database and kinetic models for surrogate diesel fuels**. [S.l.], 2007. SAE Technical Paper 2007-01-0201.

FRASSOLDATI, A. et al. Reduced kinetic mechanisms of diesel fuel surrogate for engine cfd simulations. **Combustion and Flame**, Elsevier, v. 162, n. 10, p. 3991–4007, 2015.

GALLE, J.; SEBASTIAN, V. Influence of diesel surrogates on the behavior of simplified spray models. In: SPRINGER. **Proceedings of the FISITA 2012 World Automotive Congress**. [S.l.], 2013. p. 361–374.

GERMANO, M. et al. A dynamic subgrid-scale eddy viscosity model. **Physics of Fluids A: Fluid Dynamics**, AIP, v. 3, n. 7, p. 1760–1765, 1991.

GONG, C.; JANGI, M.; BAI, X.-S. Large eddy simulation of n-dodecane spray combustion in a high pressure combustion vessel. **Applied Energy**, Elsevier Inc., v. 136, p. 373–381, 2014.

GONG, C. et al. Large eddy simulation of air entrainment and mixing in reacting and non-reacting diesel sprays. **Flow, Turbulence and Combustion**, Springer Science+Business Media Dordrecht, v. 93, p. 385–404, 2014.

GOROKHOVSKI, M.; SAVELIEV, V. Analyses of kolmogorov's model of breakup and its application into lagrangian computation of liquid sprays under air-blast atomization. **Physics of Fluids**, AIP, v. 15, n. 1, p. 184–192, 2003.

HAN, Z.; REITZ, R. D. Turbulence modeling of internal combustion engines using RNG  $k - \epsilon$  models. **Combustion Science and Technology**, Taylor & Francis, v. 106, n. 4-6, p. 267–295, 1995.

HAWKES, E. **Chemistry effects on ignition**. Kyoto, Japan, 2015. (Fourth Workshop of the Engine Combustion Network).

HIROYASU, H.; ARAI, M. **Structures of fuel sprays in diesel engines**. Warrendale, PA: Society of Automotive Engineers, 1990. (SAE Technical Paper 900475).

HOLZMANN, T. **Mathematics, Numerics, Derivations and OpenFOAM**. Fourth. Leoben: Holzmann CFD, 2016. Disponível em: <[www.holzmann-cfd.de](http://www.holzmann-cfd.de)>.

HUH, K. Y.; GOSMAN, A. D. A phenomenological model of diesel spray atomization. In: **Proc. Int. Conf. on Multiphase Flows**. [S.l.: s.n.], 1991. v. 91.

IRANNEJAD, A.; JABERI, F. Large eddy simulation of turbulent spray breakup and evaporation. **International Journal of Multiphase Flow**, Elsevier, v. 61, p. 108–128, 2014.

JANGI, M. et al. On large eddy simulation of diesel spray for internal combustion engines. **International Journal of Heat and Fluid Flow**, Elsevier Inc., v. 53, p. 68–80, 2015.

- JONES, W.; LAUNDER, B. The prediction of laminarization with a two-equation model of turbulence. **International journal of heat and mass transfer**, Elsevier, v. 15, n. 2, p. 301–314, 1972.
- KARLSSON, J. Implementing anisotropic adaptive mesh refinement in openfoam. Chalmers University of Technology, 2013.
- KE, L.; LIXING, Z.; CHAN, C. Large-eddy simulation of ethanol spray-air combustion and its experimental validation. **Chinese Journal of Chemical Engineering**, Elsevier, v. 22, n. 2, p. 214–220, 2014.
- KELLER, J. et al. Numerical and experimental investigation on droplet dynamics and dispersion of a jet engine injector. **International Journal of Multiphase Flow**, Elsevier, v. 75, p. 144–162, 2015.
- KRALJ, C. **Numerical simulation of Diesel spray processes**. Tese (Doutorado) — University of London, 1996.
- LEE, D.; POMRANING, E.; RUTLAND, C. J. **LES Modeling of Diesel Engines**. Warrendale, PA: Society of Automotive Engineers, 2002. (SAE Technical Paper 2002-01-2779).
- LEE, M. W. et al. Comparison and correction of the drop breakup models for stochastic dilute spray flow. **Applied Mathematical Modelling**, Elsevier, v. 36, n. 9, p. 4512–4520, 2012.
- LIU, A. B.; MATHER, D. K.; REITZ, R. D. **Modeling the effects of drop drag and breakup on fuel sprays**. Warrendale, PA: Society of Automotive Engineers, 1993. (SAE Technical Paper 930072).
- LUCAS, K. Die druckabhängigkeit der viskosität von flüssigkeiten—eine einfache abschätzung. **Chemie Ingenieur Technik**, Wiley Online Library, v. 53, n. 12, p. 959–960, 1981.
- LUO, Z. et al. Development and validation of an n-dodecane skeletal mechanism for spray combustion applications. **Combustion theory and modelling**, Taylor & Francis, v. 18, n. 2, p. 187–203, 2014.
- MAREK, M. The double-mass model of drop deformation and secondary breakup. **Applied Mathematical Modelling**, Elsevier, v. 37, n. 16, p. 7919–7939, 2013.
- MARTÍNEZ-MARTÍNEZ, S. et al. Liquid sprays characteristics in diesel engines. In: **Fuel Injection**. [S.l.]: InTech, 2010.

MENON, S.; YEUNG, P.-K.; KIM, W.-W. Effect of subgrid models on the computed interscale energy transfer in isotropic turbulence. **Computers & fluids**, Elsevier, v. 25, n. 2, p. 165–180, 1996.

NABER, J. D.; SIEBERS, D. L. **Effects of gas density and vaporization on penetration and dispersion of diesel sprays**. [S.l.], 1996.

NARAYANASWAMY, K.; PEPIOT, P.; PITSCH, H. A chemical mechanism for low to high temperature oxidation of n-dodecane as a component of transportation fuel surrogates. **Combustion and Flame**, Elsevier, v. 161, n. 4, p. 866–884, 2014.

NORDIN, P. **Complex chemistry modeling of diesel spray combustion**. [S.l.]: Chalmers University of Technology, 2001.

O'ROURKE, P. J.; AMSDEN, A. A. **The TAB method for numerical calculation of spray droplet breakup**. Warrendale, PA: Society of Automotive Engineers, 1987. (SAE Technical Paper 872089).

PARK, S. W.; KIM, H. J.; LEE, C. S. An experimental and numerical study on atomization characteristics of gasoline injector for direct injection engine. In: **ILASS Americas - 15<sup>th</sup> Annual Conference on Liquid Atomization and Spray Systems**. [S.l.: s.n.], 2002. p. 47–51.

PATTERSON, M. A.; REITZ, R. D. **Modeling the Effect of Fuel Spray Characteristics on Diesel Engine Combustion and Emission**. Warrendale, PA: Society of Automotive Engineers, 1998. (SAE Technical Paper 980131).

PEI, Y. et al. Modelling n-dodecane spray and combustion with the transported probability density function method. **Combustion and Flame**, Elsevier, v. 162, n. 5, p. 2006–2019, 2015.

PITZ, W. J.; MUELLER, C. J. Recent progress in the development of diesel surrogate fuels. **Progress in Energy and Combustion Science**, Elsevier, v. 37, n. 3, p. 330–350, 2011.

POINSOT, T.; VEYNANTE, D. **Theoretical and numerical combustion**. Philadelphia: RT Edwards, Inc., 2005.

POLING, B. E. et al. **The properties of gases and liquids**. [S.l.]: McGraw-hill New York, 2001.

POPE, S. B. **Turbulent flows**. [S.l.]: IOP Publishing, 2001.

REITZ, R. D. Modeling atomization processes in high-pressure vaporizing sprays. **Atomization and Spray Technology**, v. 3, n. 4, p. 309–337, 1987.

RUTLAND, C. Large-eddy simulations for internal combustion engines—a review. **International Journal of Engine Research**, SAGE Publications, p. 421–451, 2011.

RUTLAND, C. J. **Development and use of LES for Diesel Engine CFD**. Madison, PA: University of Wisconsin, 2009. (Engine Research Center).

SEARCHINGER, T. D.; HEIMLICH, R. et al. Estimating greenhouse gas emissions from soy-based us biodiesel when factoring in emissions from land use change. **The lifecycle carbon footprint of biofuels**, p. 35–45, 2008.

SENECAL, P. et al. **An investigation of grid convergence for spray simulations using an LES turbulence model**. Warrendale, PA: Society of Automotive Engineers, 2013. (SAE Technical Paper 2013-01-1083).

SIEBERS, D. L. **Liquid-phase fuel penetration in diesel sprays**. [S.l.], 1998.

SMAGORINSKY, J. General circulation experiments with the primitive equations: I. the basic experiment. **Monthly weather review**, v. 91, n. 3, p. 99–164, 1963.

SMITH, J. et al. **A Comparison of Spray-Guided Stratified-Charge Combustion Performance with Outwardly-Opening Piezo and Multi-Hole Solenoid Injectors**. Warrendale, PA: Society of Automotive Engineers, 2011. (SAE Technical Paper 2011-01-1217).

SONE, K.; MENON, S. Effect of subgrid modeling on the in-cylinder unsteady mixing process in a direct injection engine. **Journal of engineering for gas turbines and power**, American Society of Mechanical Engineers, v. 125, n. 2, p. 435–443, 2003.

TANNER, F. X. **Liquid jet atomization and droplet breakup modeling of non-evaporating diesel fuel sprays**. Warrendale, PA: Society of Automotive Engineers, 1997. (SAE Technical Paper 970050).

TAYLOR, G. I. The instability of liquid surfaces when accelerated in a direction perpendicular to their planes. **The scientific papers of sir Geoffrey Ingram Taylor**, Cambridge University Press, v. 3, p. 532–536, 1963.

TSANG, C.-W.; TRUJILLO, M. F.; RUTLAND, C. J. Large-eddy simulation of shear flows and high-speed vaporizing liquid fuel sprays. **Computer & Fluids**, Elsevier Inc., v. 105, p. 262–279, 2014.

WANG, H. et al. Development of a reduced n-dodecane-pah mechanism and its application for n-dodecane soot predictions. **Fuel**, Elsevier, v. 136, p. 25–36, 2014.

WEHRFRITZ, A. et al. Large eddy simulation of high-velocity fuel sprays: Studying mesh resolution and breakup model effects for spray a. **Atomization and Sprays**, Begel House Inc., v. 23, n. 5, p. 419–442, 2013.

XUE, Q. et al. A study of grid resolution and sgs models for les under non-reacting spray conditions. In: **ILASS Americas, 25th Annual Conference on Liquid Atomization and Spray Systems**. [S.l.: s.n.], 2013.

YOSHIZAWA, A.; HORIUTI, K. A statistically-derived subgrid-scale kinetic energy model for the large-eddy simulation of turbulent flows. **Journal of the Physical Society of Japan**, The Physical Society of Japan, v. 54, n. 8, p. 2834–2839, 1985.

ZHOU, L. et al. Large eddy simulation of spray and combustion characteristics with realistic chemistry and high-order numerical scheme under diesel engine-like conditions. **Energy Conversion and Management**, Elsevier Inc., v. 93, p. 377–387, 2015.